Cosmological Parameters and the Large Numbers of Eddington and Dirac

A. Yu. Andreev and B. V. Komberg

Space Research Institute, Russian Academy of Sciences,
Profsoyuznaya ul. 84/32, Moscow, 117810 Russia

Received March 4, 1999

Abstract—Cosmological large numbers are studied using dimensional analysis. Expressions linking cosmological parameters with fundamental constants of the microworld are proposed. The Zel'dovich formula for the cosmological constant is generalized, and a series of characteristic masses of the Universe is derived. © *2000 MAIK "Nauka/Interperiodica".*

1. ON THE FUNDAMENTAL CONSTANTS

The basic cosmological parameters can be expressed in terms of fundamental physical constants, although there is not yet a theory that can explain this fact and derive the exact formulas. One possible starting point in obtaining such expressions is the so-called dimensional analysis (this approach is similar to using the renormalization group in the theory of phase transitions, finding critical numbers in hydrodynamics, and so on).

The number of dimensional fundamental constants (c, $\hbar$, and G) coincides with the number of basic dimensions (centimeter, gram, and second). Consequently, any physical quantity X can be associated with a combination of the above three fundamental constants that has the same dimension: $X_{\text{fund}} = c^m \hbar^n G^k$. As a result, all other physical constants can be considered dimensionless if they are written as the ratio X/X_{fund}. In this form, their values do not depend on the choice of a particular system of units.

For example, the electron charge in dimensionless form is equal to $\sqrt{\alpha}$, where $\alpha = e^2/\hbar c = 1/137$ is the fine-structure constant, and the combination $\sqrt{\hbar c}$ has the dimension of a charge. Here, α is the only constant determining the electromagnetic interaction. Other interactions also possess dimensionless constants (in particular, the "charge" of the strong interaction is ~10, the constant of the electroweak interaction for small momentum transfers $\alpha_W \sim 0.1$). We emphasize that these dimensionless constants do not considerably differ from unity to order of magnitude; therefore, large numbers ~10^n, where $n \gg 1$, cannot be constructed from these constants. Nevertheless, precisely such "large numbers" should specify the scale of cosmological parameters, as was pointed out for the first time by Eddington [1] and Dirac [2].

Large numbers (or the small numbers that are their inverses) can be obtained from the fundamental constants by specifying the ratios of particle masses (see, for example, [3–6]). Therefore, we can suppose that cosmological parameters are also determined by ratios of the corresponding masses or, in other words, of the energetic scales at which these parameters appear in cosmology. (This idea is similar to the suggestion of Muradyan [7] that the ratios of the masses of astrophysical objects are determined by their angular momenta.)

One fundamental quantity with the dimension of mass is the so-called Planck mass $m_{\text{Pl}} = \sqrt{\hbar c/G} = 10^{-5}$ g (this is the mass whose gravitational radius $r_g = 2Gm/c^2$ is equal to its Compton wavelength $\lambda = \hbar/mc$). All other masses can be expressed in dimensionless form via the ratio

$$g = \frac{Gm^2}{\hbar c} = \left(\frac{m}{m_{\text{Pl}}}\right)^2. \qquad (1)$$

The appearance of this constant resembles the fine-structure constant α. Its physical meaning is the same: It is the ratio of the energy of gravitational interaction between two particles when they are separated by a distance equal to their Compton wavelength to the particle' rest mass. For most particles, g^{-1} is a large number from the point of view of Eddington and Dirac. (For example, $g^{-1} \approx 2 \times 10^{38}$ for a proton, although it is not necessary to take $m = m_p$.)[1]

Thus, we conclude that expressions for cosmological parameters should contain precisely the constant g (possibly to a power n, not a large number; we take $|n| \leq 4$ in our subsequent consideration) multiplied by a dimensional quantity for the corresponding parameter,

---

[1] Note that Eddington [1] and Dirac [2] considered a slightly different combination of constants producing large numbers: $e^2/Gm_e m_p = 2 \times 10^{39}$, where m_e and m_p are the masses of the electron and proton. This number corresponded to the ratio of the gravitational interaction between the electron and proton in an atom to the electrical interaction between them.

derived from the fundamental constants. This leads us to a formula of the form

$$X = g^n X_{\text{fund}}. \qquad (2)$$

2. ZEL'DOVICH FORMULA FOR THE COSMOLOGICAL CONSTANT ANT ITS GENERALIZATION

We can use the above considerations to calculate the current value of the cosmological constant Λ or, what amounts to the same thing, the energy density of the cosmological vacuum $\rho_\Lambda = c^2\Lambda/8\pi G$. About 30 years ago, Zel'dovich [8] suggested that this density should be expressed in terms of the fundamental constants and proposed the formula

$$\rho_\Lambda = \frac{Gm^2}{\lambda c^2}\frac{1}{\lambda^3} = \frac{Gm^6 c^2}{\hbar^4}. \qquad (3)$$

In this form, ρ_Λ is defined as the energy density of the gravitational interaction between a virtual vacuum particle at the Compton wavelength. Taking the masses of the proton and electron as the particle masses, Zel'dovich [8] was not able to obtain an estimate for ρ_Λ that coincided with the available observational data. However, Kardashev [9] has recently pointed out that substituting $m = m_\pi$ into the formula of Zel'dovich (3) leads to a satisfactory agreement with observations.[2]

The only combination of dimensional fundamental constants with the dimension of density is the so-called Planck density (defined as the ratio $m_{\text{Pl}}/l_{\text{Pl}}^3$, where l_{Pl} is the Planck length, equal to the gravitational radius for m_{Pl}):

$$\rho_{\text{Pl}} = \frac{c^5}{G^2\hbar} = 10^{92}\ \text{g/cm}^3.$$

The current value of the vacuum density can be roughly estimated from observational data, $\rho_\Lambda \sim \rho_{cr} \sim 10^{-29}\ \text{g/cm}^3$. Thus, the ratio of the Planck density to the current critical density is

$$\frac{\rho_{\text{Pl}}}{\rho_{cr}} = 10^{121}, \qquad (4)$$

which is precisely an example of an Eddington–Dirac large number. Therefore, based on our approach to expressions for cosmological parameters (2), we can write

$$\rho_\Lambda = g^n \frac{c^5}{G^2\hbar} = \left(\frac{m}{m_{\text{Pl}}}\right)^{2n}\frac{c^5}{G^2\hbar}. \qquad (5)$$

---

[2] We imply here not a vacuum of pions, which are unstable particles, but a vacuum scalar field (i.e., virtual particles) with the mass $\sim m_\pi$.

This is a generalization of Zel'dovich's formula, which follows from (5) as a special case for $n = 3$.[3] Comparing formulas (4) and (5) leads to the relation

$$\left(\frac{m}{m_{\text{Pl}}}\right)^{2n} \sim 10^{-121},$$

where the virtual-particle mass m corresponds to the energetic scale for the formation of the current vacuum energy density. Depending on the n chosen, we can obtain various estimates for this mass:

$$m \sim m_{\text{Pl}}10^{-\frac{60}{n}}, \qquad (6)$$

namely,

$$n = 1 \longrightarrow m = 10^{-65}\ \text{g} = 10^{-32}\ \text{eV},$$

$$n = 2 \longrightarrow m = 10^{-35}\ \text{g} = 10^{-2}\ \text{eV (axion?! neutrino?)},$$

$$n = 3 \longrightarrow m = 10^{-25}\ \text{g} = 100\ \text{MeV (pion?!)},$$

$$n = 4 \longrightarrow m = 10^{-20}\ \text{g} = 10\ \text{TeV (Higgs boson?!)}.$$

As noted above, estimates of the particle masses were already presented for the case $n = 3$ in [9].

The mass value for $n = 4$ gives us the scale for electroweak interactions. The corresponding formula for the vacuum density can be written

$$\rho_\Lambda = \frac{G^2 m^8 c}{\hbar^5}. \qquad (7)$$

This may have the meaning of a quantum-gravity correction to the initial zero density of the vacuum energy. Of course, formula (7) cannot explain why, among all possible interactions, only gravity contributes to the quantum corrections and how this initial zero density is produced. A theoretical mechanism satisfying these two requirements using a model of "antipodal" particles was put forward in [10, 11].

3. CHARACTERISTIC MASSES IN THE UNIVERSE

In conclusion, let us turn our attention again to the results of [7]. Muradyan [7] draws three lines in the plane $\ln J - \ln m$:

$$(1)\ n = 1,\ J^{(1)} = \hbar\left(\frac{m}{m_{\text{Pl}}}\right)^2 = \frac{Gm^2}{c};$$

---

[3] In [7], the Regge law for the angular momenta of hadrons $J^{(1)} = \hbar(m/m_p)^2$ was generalized in a similar way for "n-dimensional hadrons." This yielded the expression $J^{(n)} = \hbar(m/m_p)^{(1 + 1/n)}$. If m_p in this formula is replaced by m_{Pl}, we obtain expressions for the momentum $J^{(1)}_{Kerr} = \hbar(m/m_{\text{Pl}})^2 = gJ^{(1)}$ or $J^{(n)}_{Kerr} = \hbar(m/m_{\text{Pl}})^{(1 + 1/n)}$. The quantity n in the last formula denotes the geometric dimension of an astronomical object (string, disk, or ball) whose momentum is determined by this formula (see below).

(2) $n = 2$, $J^{(2)} = \hbar \left(\dfrac{m}{m_{\mathrm{Pl}}} \right)^{3/2}$;

(3) $n = 3$, $J^{(3)} = \hbar \left(\dfrac{m}{m_{\mathrm{Pl}}} \right)^{4/3}$.

By plotting the observational data for the momenta J and masses m of various astronomical objects in this plane, he found that the planets and stars are located on the line for $n = 3$ (a ball). Disk galaxies and galaxy clusters correspond to the line with $n = 2$ (a disk). The intersection of the line $n = 3$ with the line $n = 1$ gives the so-called Chandrasekhar point ($m_* \approx 10^{33}$ g) and the intersection of $n = 3$ with the line $n = 2$, the Eddington point ($m_{**} = 10^{52}$ g). Using the parameter g introduced above (see formula (1)), we can write

$$m_* = m_{\mathrm{Pl}} \left(\frac{m_{\mathrm{Pl}}}{m} \right)^2 = g^{-1} m_{\mathrm{Pl}}, \qquad (8)$$

$$m_{**} = m_{\mathrm{Pl}} \left(\frac{m_{\mathrm{Pl}}}{m} \right)^3 = g^{-\frac{3}{2}} m_{\mathrm{Pl}}, \qquad (9)$$

where, in accordance with [7], we have chosen the proton mass $m = m_p$ as the energetic scale. The Chandrasekhar mass m_* represents the characteristic mass of a star, whereas the Eddington mass m_{**} can be interpreted as the total mass of matter in the Universe (the "mass of the World").

Formulas (8) and (9) can also be rewritten in a slightly different form: $m_* = m_p (m_{\mathrm{Pl}}/m_p)^3$ and $m_{**} = m_p (m_{\mathrm{Pl}}/m_p)^4$. Then, the series of masses in terms of powers of g can be generalized as

$$m = m_p (g^{-1})^{n/2}. \qquad (10)$$

For $n = 0, 1, 2, 3$, and 4, we obtain $m_p = 10^{-24}$ g, $m_{\mathrm{Pl}} = 10^{-5}$ g, $m = 10^{14}$ g, $m_* = 10^{33}$ g, and $m_{**} = 10^{52}$ g, respectively. The interpretation is difficult only for the third of these characteristic masses. Nevertheless, it is striking that, to an order of magnitude, it coincides with the mass of a black hole that just completes its evaporation at the current time in the Universe's evolution. According to [12], the mass of such a black hole is given by the formula

$$M \sim \sqrt[3]{10^{-4} \frac{T_0}{t_{\mathrm{Pl}}}} \, m_{\mathrm{Pl}} \approx 10^{14} \ \text{г}. \qquad (11)$$

It is not an accidental fact that precisely the substitution of the age of the Universe T_0 gives the required mass: From the viewpoint of Kardashev [9], the current time is quite specific, since the vacuum is beginning to again dominate over matter, and a new stage of inflation is taking place.

ACKNOWLEDGMENTS

REFERENCES

1. A. S. E. Eddington, Proc. Cambridge Philos. Soc. **27**, 15 (1931); Proc. R. Soc. London **133**, 605 (1931).

2. P. A. M. Dirac, Nature **139**, 323 (1937); Proc. R. Soc. London **165**, 199 (1938).

3. Yu. V. Baryshev and A. A. Raǐkov, Astrofizika **28**, 689 (1988).

4. A. Julg, Astrophys. J. **271**, 9 (1983).

5. M. A. Markov, Fiz. Élem. Chastits Atom. Yadra **29** (1998).

6. I. L. Rozental', *The Universe and Particles* (Znanie, Moscow, 1990).

7. R. M. Muradyan, Fiz. Élem. Chastits Atom. Yadra **28**, 1190 (1997).

8. Ya. B. Zel'dovich, Pis'ma Zh. Éksp. Teor. Fiz. **6**, 883 (1967).

9. N. S. Kardashev, Astron. Zh. **74**, 803 (1997).

10. A. D. Linde, Rep. Prog. Phys. **47**, 979 (1984).

11. A. Yu. Andreev, Krat. Soob. Fiz. FIAN **8**, 10 (1998).

12. I. D. Novikov and V. P. Frolov, *Physics of Black Holes* (Nauka, Moscow, 1986), p. 226.

Translated by Yu. Dumin

A Self-Consistent Model for an Isotropic Universe Evolving under the Influence of Quantum Gravitational Effects

E. G. Vertogradova and Yu. S. Grishkan

Rostov State University,
pr. Stachki 194, Rostov-on-Don, 344104 Russia
Received July 29, 1998

Abstract—The polarization-correction energy–momentum tensor for a semi-classical gravitational theory is derived. This tensor accounts for the creation of particles from a vacuum at a finite temperature. The theory contains an asymptotic cosmological Friedmann solution. The solution obtained turns out to be dynamically stable, so that it can form the observed properties of the Universe. New cosmological solutions describing the early stages of cosmological evolution of a homogeneous isotropic Universe are obtained. One of these corresponds to the simultaneous creation of matter and geometry from the vacuum of a flat, empty space–time without structure. Another solution corresponds to a high-temperature inflation regime. A cosmological scenario for the creation of the observed Universe from "nothing" that includes the properties of all the solutions obtained is put forward. © 2000 MAIK "Nauka/Interperiodica".

1. FORMULATION OF THE MODEL

Currently, various possibilities for realistic scenarios for the evolution of the hot Universe, including its early quantum stages, are being put forward and actively developed. Let us discuss the main aspects of constructing such scenarios for a flat, isotropic model of the Universe, taking into account the fact that the global macroscopic properties of the space are formed by quantum gravitational effects. We can use a quasi-classical, semi-quantum theory of gravitation [1–7] to study these effects. In such theories, applicable for space–time scales $l \geq l_g, t \geq t_g,$[1] the gravitational field is assumed to be classical, whereas all other fields of the physical matter are subject to quantization. In this sense, the semi-quantum theory represents an intermediate stage between quantum geometrodynamics and Einsteinian general relativity. As emphasized in some studies (e.g., [6, 7]), in semi-quantum theories, many new solutions can be obtained that are free of singularities of the space–time curvature and energy density at small physical times $t \longrightarrow t_g$. However, no attempts to obtain solutions for the complete equations of such theories (including general asymptotic solutions that depend on the maximum number of constants) have been undertaken in previous studies. The aim of the present paper is to close this gap.

Certain criteria for the construction of the basic equations have been developed in semi-quantum theory [1–9]. The Lagrangian of the quantum polarization corrections is local and restricted to linear and quadratic terms in the space–time curvature R. The effect of particle creation [5] is taken into account using the viscos-

ity coefficients of the vacuum of the gravitational field in the law of entropy increase for an ultrarelativistic medium. In turn, this law follows from the expression for the rate of spontaneous creation of particles in the ultrarelativistic medium [5]. Analyses of general properties and a number of solutions of the corresponding equations have been presented in many studies (see, for example, [1–11]). In particular, under certain simplifying assumptions, a characteristic feature of the semi-quantum theory of gravitation are so-called "scalaron" oscillations of the space–time metric, which are not damped even in the Einstein limit $R \ll l_g^{-2}$. In these papers, the state of the origin of the Universe is often assigned to a low-temperature inflationary de Sitter solution (see [12]). However, it was later shown that such solutions, which correspond to a vacuum oversaturated in energy, are unstable from the dynamic [10] and gravitational [13] points of view.

These difficulties led to skepticism about the theory as a whole. We show here that one drawback of the theory, associated with the damping-free character of the non-Einsteinian branch of the cosmological solutions, can be removed via a more accurate construction of the asymptotic expansions for the series of quantum corrections at finite temperature. In addition, it seems more logical to relate the state of the Universe's origin to solutions corresponding to the creation of the Universe from "nothing." The inflationary (de Sitter) branch of cosmological evolution is only an intermediate stage in this type of cosmological scenario.

A phenomenological construction of the energy–momentum tensor T_i^k for quantum corrections in a semi-quantum approach was started in [14]. The Pascal

---

[1] $l_g \sim 10^{-33}$ cm and $t_g \sim 10^{-44}$ s are the Planck space and time scales.

tensor was derived taking into account the distortion of the distribution function of the created particles by a self-consistent gravitational field. In quantum field theory at finite temperatures, subsequent quantum corrections to the energy-momentum tensor should be associated with the induced creation of particles in the ultrarelativistic medium and will be composed of products of quantities describing the deformation of space–time by the temperature of the medium. The effects produced by such corrections are discussed below for the case of an isotropic Universe

$$ds^2 = a^2(d\tau^2 - dl^2), \tag{1}$$

filled with an ultrarelativistic medium with a conformal temperature $\theta = Ta$.

The part of the energy-momentum tensor constructed in previous studies is[2]

$$a^4 T^0_{0(1)} = \tilde{T}^0_{0(1)} = k_1\theta^4 + k_2\dot{a}^2/a^2\theta^2,$$

where $\dot{a} = da/d\tau$. Based on considerations of the tensor dimension, the following terms, with lower powers of θ, are constructed from the $\binom{0}{0}$ components of the Einstein tensor $G^i_k = R^i_k - (1/2)\delta^i_k R$, the quadratic quantum-correction tensor $P^i_k = R^{;i}_{;k} - \delta^i_k R^{;l}_{l} - RR^i_k + (1/4)\delta^i_k R^2$, and the Hubble parameter $H = (G^0_0/3)^{1/2}$. Since the geometric invariant for ultrarelativistic matter is $R = 0$ to a first approximation with respect to curvature,[3] the required correction to the energy–momentum tensor is

$$T^0_{0(2)} = k_3 H R^0_0 T + k_4 P^0_0 \ln\frac{\mu^2}{T^2}, \tag{2}$$

where μ^2 is the renormalization scale. We can see from (2) that the tensor $T^i_{k(2)}$, which contains odd powers of R^i_k and T^i_k, is irreversible with respect to time. Such expressions can appear only in a nonlocal field theory, during the subsequent localization of its equations. Such localization of gravitational theory is possible in the early stages of evolution of the hot Universe, for example, due to the effect of the gravitational exchange interaction in an ultrarelativistic cosmological gas of elementary particles [15], followed by the formation of equilibrium statistical distributions for these particles.

Let us now explain the appearance of the factor $\ln(\mu^2/T^2)$ in the quantum-correction tensor (2). In calculations of the vacuum polarization in nonperturbation quantum field theory, the part of the polarization-correction tensor corresponding to (2) takes the form $-\ln(\hat{J}/\mu^2 a^2)S^i_{k(2)}$, where $\hat{J}$ is a quite complicated nonlo-

cal operator composed of components of the space–time metric, and $S^i_{k(2)}$ is a tensor given by a polynomial in the metric and its time derivatives. The part of the temperature quantum corrections in the energy–momentum tensor corresponding to (2) is $\ln(\hat{J}/\theta^2)S^i_{k(2)}$. If these expressions are added, we obtain the term $\ln(\mu^2 a^2/\theta^2)S^i_{k(2)}$. Therefore, the renormalization scale μ^2 enables us to accumulate quantum corrections of various kinds in the form of one simple tensor expression (2).[4] The component of the energy-momentum tensor $a^4 T^0_0 = a^4 T^0_{0(1)} + a^4 T^0_{0(2)}$ in the metric (1) for the model under consideration takes the form:

$$a^4 T^0_0 = \tilde{T}^0_0 = k_1\Theta^4 + k_2\frac{\dot{a}^2}{a^2}\Theta^2$$
$$+ k_3\Theta\left(\frac{\dot{a}^3}{a^3} - \frac{\dot{a}\ddot{a}}{a^2}\right) - k_4\left(2\frac{\dot{a}a^{(3)}}{a^2} - \frac{\ddot{a}^2}{a^2} - 4\frac{\dot{a}^2\ddot{a}}{a^3}\right)\ln\frac{\mu^2 a^2}{\Theta^2}. \tag{3}$$

A complete system of dynamical equations describing the Universe's evolution taking into account quantum gravitational effects contains equations of motion for the scale factor and an equation for the temperature, which follows from the law of entropy increase in the ultrarelativistic medium due to the creation of particles from vacuum by the strong classical gravitational field $R/m^2 \gg 1$:

$$l_g^{-2}(\dot{a}^2 - \Lambda a^4) = \beta\frac{\dot{a}^4}{a^4} + k_1\Theta^4 + k_2\frac{\dot{a}^2}{a^2}\Theta^2$$
$$+ k_3\Theta\left(\frac{\dot{a}^3}{a^3} - \frac{\dot{a}\ddot{a}}{a^2}\right) - k_4\left(2\frac{\dot{a}a^{(3)}}{a^2} - \frac{\ddot{a}^2}{a^2} - 4\frac{\dot{a}^2\ddot{a}}{a^3}\right)\ln\frac{\mu^2 a^2}{\Theta^2}, \tag{4}$$

$$\dot{\Theta}\Theta^2 = \alpha\frac{\ddot{a}^2}{a^2}. \tag{5}$$

Here, $\beta\dot{a}^4/a^4$ is the component of the energy-momentum tensor for the conformal anomaly and Λ is the cosmological Λ term.

An exact microscopic calculation fixes only the coefficients of the system (4) and (5). If only a scalar field is present, these coefficients are

$$k_1 = \frac{\pi^4}{30}, \quad k_2 = \frac{1}{24}, \quad k_3 = \frac{\pi}{8}, \quad k_4 = \frac{9}{8\pi^4},$$
$$\beta = \frac{1}{1440\pi^2}, \quad \alpha = \frac{15}{16\pi^3}. \tag{6}$$

---

[2] Here and below, we use the system of units $\hbar = c = 1$.
[3] Due to relation $R = \kappa T$.

[4] Exact calculation shows that precisely such a structure, evident from the dimensional considerations presented above, can be obtained via accurate derivation of the Green functions for the quantum fields in a self-consistent gravitational field.

Since the set of quantum fields has not been fixed up to the present time by the current theory of elementary particles, the corresponding coefficients should be considered phenomenological.

2. THE HIGH-TEMPERATURE INFLATIONARY SOLUTION AND ITS STABILITY

Inflationary solutions are of particular interest in constructing scenarios for cosmological evolution. Here, we derive such a solution and study its stability. Application of Lie-group symmetry methods (see, for example, [16, 17]) to the system of equations (4) and (5), described in the Appendix, enabled us to reduce the order of this system twofold. The invariants of the similarity-transformation group P and T have the physical meaning of the curvature $G_0^0/3$ and temperature of the medium, respectively. Using the change of variables (A.2), equation (4) can be rewritten in terms of the unknown functions P and T. From here, it is easy to obtain a particular solution with stationary physical parameters P_0 and T_0—the curvature and temperature of the medium:

$$P = P_0 = \text{const}(t), \quad T = T_0 = \text{const}(t),$$
$$\frac{a}{a_0} = \exp[P_0^{1/2}(t - t_0)], \tag{7}$$

where $t = \int a d\tau$ is the physical time.

Solution (7) is inflationary and, as will be explained below in detail, will be referred to as a de Sitter–Hoyle solution. The parameters P_0 and T_0 determined by the system of algebraic equations (A.4) obviously exist when the Λ term is sufficiently small,

$$\Lambda \leq \frac{l_g^{-2}}{4A}, \tag{8}$$

where $A = \beta + k_1(4\alpha)^{4/3} + k_2(4\alpha)^{2/3} - k_3(4\alpha)^{1/2}$, and take the form

$$T_0 = (4\alpha)^{1/3} P_0^{1/2} \text{sign}(P_0^{1/2}),$$
$$P_0 = \frac{l_g^{-2}}{2A}(1 \pm \sqrt{1 - 4A\Lambda l_g^2}). \tag{9}$$

A negative value of $P_0^{1/2}$ in expression (9) for the temperature is prohibited from the physical point of view. Therefore, a solution with stationary physical parameters—the curvature P_0 and temperature of the medium T_0—occurs only during the stage of expansion with positive Hubble parameter for the stationary solution

$$H_0 = P_0^{1/2},$$

where the subscript "0" corresponds to the physical solution (9).

When $\alpha = 0$ ($T_0 = 0$), the solution under consideration coincides with the de Sitter solution, which describe a space–time with constant curvature expanding exponentially with time (the low-temperature inflation of Starobinskiĭ). If we impose the condition $\alpha = \beta = 0$, the inflationary solution follows immediately from (A.4), and its parameters are determined directly by the Λ term:

$$P_0 = \Lambda.$$

This is precisely the form of an asymptotic (as $t \longrightarrow \infty$) Robertson–Lemaitre solution in general relativity [18].

When $\beta = 0$ and $\Lambda = 0$, the stationary solution (7) coincides with the Hoyle solution [8, 10], which describes the creation of matter via the birth of particles. In this case, the quantum gravitational process of particle birth plays the role of the hypothetical C field of Hoyle.

In the general case, the cosmological expansion (7) is governed by a combined de Sitter–Hoyle law. The existence of such a solution is expected based on simple physical considerations. Indeed, this solution arises in the case of complete compensation of two oppositely-directed processes: A decrease in the density of the medium due to expansion is compensated by its increase due to the creation of particles by the gravitational field. The analysis of the dynamic stability of the stationary solution presented in the Appendix [see (A.7)–(A.10)] shows that it is unstable for a wide range of model parameters. Moreover, this instability is exponential with respect to the physical time t. All the instability increments are determined by the numerical values of the model parameters k_1, k_2, k_3, k_4, α, and $n_0 = \ln(\mu^2/T^2)$. For example, the increment for $\Lambda = 0$ takes the form

$$\gamma = \frac{l_g^{-1}}{(4\alpha)^{1/3}k_3}. \tag{10}$$

The presence of another asymptotic (at $P \longrightarrow \infty$) symmetry of the similarity transformations (A.11) in equations (4) and (5) does not, in general, enable us to reduce the order of this system of equations but significantly simplifies our subsequent analysis [see (A.12)]. After all the transformations resulting from the symmetries, the exact equations of the semi-quantum theory (4) can be reduced to the form (A.13), which is the most convenient form for finding asymptotic solutions for various extreme values of the space–time curvature. This problem is discussed below.

3. A PARTICULAR NONSTATIONARY SOLUTION OF THE GRAVITATIONAL EQUATIONS, INTERPRETED AS THE UNIVERSE'S BIRTH FROM "NOTHING"

Apart from solutions of the form (7), the model under consideration has another particular solution of equations (A.13) under certain initial conditions, which are not included in the general case. For example, when the curvature of space–time is small $Rl_g \ll 1$, the geo-

metric vacuum terms dominate over matter terms, and $\Lambda = 0$ in (A.13), we have the following vacuum solution:

$$P = \left(\frac{I_0}{4}\right)^4 l_g^{-6}(t - t_0)^4, \quad T = (\alpha_1|I_0|)^{1/3} P^{1/4} l_g^{(-1/2)},$$

$$\frac{a}{a_0} = \exp\left[\frac{l_g^{-3}I_0^2}{48}(t - t_0)^3\right], \tag{11}$$

which is valid at times satisfying the condition

$$\left[\frac{I_0}{4}(t - t_0)l_g^{-1}\right]^4 < \frac{1}{\alpha}\left(\frac{3n_0k_4}{k_1}\right)^{1/2}.$$

Here, a_0, t_0, and I_0 are arbitrary constants, and $n_0 = \ln(\mu^2/T^2) = \ln(\mu^2/LP)$. In this case, we have the following asymptotic estimates for the parameters of the temperature and curvature of solution (11):

$$G_0^0 = R_0^0 - \frac{1}{2}R \sim (t - t_0)^4, \quad T \sim t - t_0. \tag{12}$$

The increase in the medium temperature with time in (11) corresponds to the creation of particles. We can see from the inequality in this formula that such particle creation plays the role of a trigger mechanism, making possible the existence of an expansion regime. The curvature G_0^0 and temperature T are obviously equal to zero at the initial time t_0:

$$\left(R_0^0 - \frac{1}{2}R_0\right)\bigg|_{t_0} = 0, \quad T\big|_{t_0} = 0.$$

In other words, at $t = t_0$, the solution corresponds to an empty, flat space–time without any structure. This type of space is topologically equivalent to a closed space [19]. Thus, solution (11) in the quasi-classical (semi-quantum) theory of gravitation can be interpreted as the birth of the Universe from "nothing" in quantum geometrodynamics ([7, 20]). In the evolution of the model, this initial state separates into geometry and particles under the action of an initial impulse, which is described as a nonzero fourth derivative of the curvature at the initial time:

$$\left(R_0^0 - \frac{1}{2}R\right)^4\bigg|_{t_0} = 4!(I_0/4)^4 l^{-6} \neq 0.$$

Note that the assumption of thermodynamic equilibrium at the early stages of the cosmological evolution of the Universe corresponds to the rapid thermalization of the created particles. Therefore, the characteristic times for particle creation and thermalization near the Planck scales $l \sim l_g$ should be comparable. This evidently corresponds to the rough character of the approximation. Nevertheless, the proposed approach reflects quite important features of the physical phenomena under consideration. One justification for the approach is the introduction of real gravitons to form

the initial part of the evolution of the Universe filled with the quanta of physical matter fields [7]. Indeed, gravitons are the only particles that are both massless and conformally noninvariant. Therefore, there is no threshold for their creation at small curvatures, whereas, as before, the law of entropy increase has the form (5). As a result, adding gravitons in the semi-quantum theory can lead to the formation of a vacuum stage in the Universe's evolution.

To draw a complete phase portrait and calculate the total number of particles created from the vacuum $N|_{t=\infty}$, our analytic treatment described here must be supplemented by numerical integration of the system (4) and (5). Strictly speaking, quantum geometrodynamics with a finite temperature for the physical vacuum should be used in the ranges of curvature, temperature, and time evolution under consideration. There is no such theory at present. Consequently, all conclusions about the character of a complete scenario for the cosmological evolution of the Universe can be drawn only using the semi-quantum theory considered here.

4. THE FRIEDMANN SOLUTION

The Friedmann solution is asymptotic both for the general solution of the equations of the semi-quantum theory (4), (5), (A.13) and for the particular solution (11). As noted in Section 1, the semi-quantum theory with quadratic invariants in the Lagrangian has been discussed for a long time. In the Friedmann limit as $R \longrightarrow 0$, this theory leads to solutions containing a non-Einsteinian mode that is not damped in time:

$$\bar{l} \sim C\left(\frac{k_4\Phi}{h}\right)^{1/4}\cos(\Phi - \Phi_0),$$

where $C = $ const, h is the dimensionless Hubble constant, and Φ is a decreasing function of h and constant parameters of the model.

Let us show that this problem can be solved if we take into account terms of the energy–momentum tensor with $k_3 \neq 0$ irreversible with respect to time (corresponding to the creation of matter). We shall consider solutions of system (A.13) for $\Lambda = 0$. It is known that these equations have no solutions for $k_3 = 0$ and $\Lambda = 0$ that approach the Friedmann solution as the curvature of space–time decreases $P \longrightarrow 0$. The situation changes radically when $k_3 \neq 0$. Let us seek a solution of equations (A.13) in the form

$$L = L_F(1 + l), \quad I = -4 + y, \tag{13}$$

where y and l are the non-Einsteinian modes of the cosmological solution,

$$I = \frac{dP}{Pd\ln(a/a_0)}, \quad L = \frac{T^2}{P}.$$

The Friedmann solution for a radiation-dominated plasma corresponds to the following physical parameters of the curvature and temperature of the medium:

$$L_F = k_1^{-1/2} l_g^{-1} F^{-1/2}, \quad F^{1/2} = \frac{\dot{a}}{a^2} = \frac{1}{2(t-t_0)}, \quad (14)$$

$$F l_g^2 = e^x, \quad T = k_1^{-1/4} l_g^{-1/2} F^{1/4},$$

and the scale factor is given by the relation

$$\frac{a}{a_0} = [2l_g^{-1}(t-t_0)]^{1/2}. \quad (15)$$

Substituting (13) and (14) into (A.9), we find a relation between the variables describing the non-Einsteinian modes of the cosmological solution $y = 16/3l'$, where $l' = dl/dx$. As a result, this system is reduced to a second-order equation for l:

$$l'' - \frac{k_3 k_1^{-1/2} l_g^{-1/2}}{x k_4} e^{-x/4} l' + \frac{6 l_g^{-1}}{x k_4} e^{-x} l = 0. \quad (16)$$

The solution of (16) can be presented in the form of WKB asymptotics in the large parameter $l_g^{-2} \sim 10^{66}$ cm^{-2}:

$$\ln \frac{a}{a_0} = -\frac{1}{2}\ln h - \frac{l}{4},$$

$$l_g^{-1}(t-t_0) = \frac{1}{2h} - \frac{l}{4h}, \quad (17)$$

$$l = 2\sqrt{2} C \left(\frac{k_4 \Phi}{h}\right)^{1/4} \exp\left(-\frac{k_3}{k_1^{1/4} k_4}\Phi\right) \cos(\Phi - \Phi_0), \quad (18)$$

where $h = l_g^1 H$ and $\Phi = -1/4h \ln h$.

Expression (17) represents a general asymptotic solution of the system (4) and (5) that depends on the four arbitrary constants a_0, t_0, C, and Φ_0. The Friedmann solution for a radiation-dominated plasma (15) follows from (17) when $l = 0$. In other words, the first terms on the right-hand side of this formula correspond to the Friedmann solution. This solution exists if the non-Einsteinian branches l, given by the arbitrary constants A and Φ_0, are suppressed when $t \longrightarrow \infty$. It follows from the general solution (17) and (18) that the constants k_3 and k_4 play the leading role in such suppression. As noted above, these constants, introduced into the matter energy–momentum tensor [i.e., the right-hand side of semi-quantum equations (4) and (5)], correspond to induced particle creation in the medium and polarization of the vacuum. Taking these into account is key in the problem of suppressing oscillations of non-Einsteinian branches of the solution.

The solution of this problem in [11] was sought without allowing for the effect of induced particle creation ($k_3 = 0$). In this case, the exponential function in the expression for l from (18) tends to zero as $t \longrightarrow \infty$ and $h \longrightarrow 0$, and the large pre-exponential terms of the

solution, which grow as $\sim h^{-1/2}$, prevail and dominate over the Friedmann part of the solution. Nevertheless, as demonstrated above, the non-Einsteinian terms of the solution are suppressed as $\sim h^{-1/2}\exp(-k_3/h)$ and decrease exponentially in the classical limit under consideration. Our study shows a particular way of finding a solution for the problem of non-Einsteinian branches in the framework of quasi-classical (semi-quantum) gravitational theory via a composite account of all quantum gravitational effects. Now, we can turn to the construction of a composite cosmological scenario using the solutions derived above and our analysis of their stability.

5. A SCENARIO FOR COSMOLOGICAL EVOLUTION INCLUDING THE BIRTH OF THE UNIVERSE FROM "NOTHING" AND ESTIMATES OF THE CHARACTERISTIC ENERGETIC SCALES

When the cosmological model born from the vacuum acquires a curvature of the order of the Planck curvature in the course of its expansion, the intersection of the vacuum branch (11) with some particular de Sitter–Hoyle solution with stationary physical parameters $P_0 = $ const and $T_0 = $ const becomes possible. As shown above, this de Sitter–Hoyle branch (7) is dynamically unstable, and the corresponding instability increment is of the order of the Planck increment. As a result, a rapid transition of the Universe initially born from the vacuum to a Friedmann branch distorted by quantum effects (17) and (18) is possible. The initial temperature of the medium on the quantum branch is $T_0 = 0$. The temperature for the stationary solution can be estimated from the Planck formula:

$$T_1 \sim l_g^{-1} \sim 10^{19} \text{ GeV}. \quad (19)$$

To estimate variations in the temperature of the medium during the transition from the stationary to the Friedmann solution, let us join the parameters of solutions (7) and (17) at times $t \sim t_g$, specified by the instability increment of the stationary solution (10). As a result, we obtain for the values of the constants (6) the dimensionless Hubble parameter $h = h_c = 2.5$, the constant $|C| \leq 2$, and the corresponding non-Einsteinian solution mode $l \sim 10^{-6}$. In realistic quantum field theory models, the value of A increases and the damping decrement for the quasi-Friedmann solution (17) decreases, due to the increasing values of the parameters k_1 and k_2 relative to k_3. Therefore, the region for joining the solutions must be shifted to curvatures corresponding to several Planck times. Similar estimates can be obtained for the non-Einsteinian mode l. This last fact implies that the Friedmann solution (15) is valid even after several Planck times. Consequently, the medium temperature in the proposed scenario rapidly increases (over the Planck time) from 0 to the Planck values (19) and then decreases with the expansion of the Universe. The final state of the overall quantum evo-

lution is the Friedmann solution for a classical radiation-dominated plasma. Therefore, the temperature scale for the hot cosmological model has the standard form for relativistic astrophysics (see, for example, [21, 22]).

From the viewpoint of quantum geometrodynamics, this case for joining the quasi-classical solutions to obtain a unified sequence that is realistic cosmologically implies a nonzero probability for the Universe to tunnel from one branch of the cosmological solutions of the quasi-classical gravitational theory to another. Our joining of the solutions yields a composite scenario for the cosmological evolution of the Universe:

(1) Decay of the vacuum of an empty, flat space without structure, followed by exponential expansion;

(2) High-temperature quantum-gravitational inflation;

(3) Evolution in accordance with a Friedmann branch distorted by quantum effects.

This scenario substitutes a flat space–time without structure for the cosmological singularity of general relativity. This object is associated with the initial state of evolution of the observed Universe. Of course, we can draw final conclusions about the perspectiveness of the proposed scenario only on the basis of quantum geometrodynamics, once there is such a theory that is capable of describing the problems considered here.

ACKNOWLEDGMENTS

APPENDIX

GROUP-THEORY METHOD FOR REDUCING THE ORDER OF THE SYSTEM OF QUANTUM GRAVITATIONAL EQUATIONS AND CONSTRUCTING THEIR SOLUTIONS

As noted in [16], where a system of equations with similar properties was considered, equations (4) and (5) possess the following continuous symmetries:

(1) translational symmetry of the time origin: $\tau \longrightarrow \tau + \tau_0$;

(2) conformal symmetry with the generator σ:

$$\dot{a}^2 \longrightarrow \dot{a}^2 \exp \sigma, \quad \Theta \longrightarrow \Theta \exp\left(\frac{\sigma}{4}\right),$$

$$a \longrightarrow a \exp\left(\frac{\sigma}{4}\right). \tag{A.1}$$

These symmetries enable us to reduce the differential order of the system (4) and (5) twofold via the change of variables:[5]

$$\dot{a}^2 = Pa^4, \quad \Theta = Ta, \quad Q^{1/2} = \frac{dP}{d\ln(a/a_0)}. \tag{A.2}$$

After substituting (A.2) into (4) and (5), the equations of the semi-quantum theory take the form:

$$l_g^{-2}(P - \Lambda) + k_4 n_0\left(\frac{1}{2}P\frac{dQ}{dP} + 3PQ^{1/2} - \frac{1}{4}Q\right)$$

$$= \beta P^2 + k_1 T^4 + k_2 T^2 P - k_3 T P^{1/2}\left(P + \frac{1}{2}Q^{1/2}\right). \tag{A.3}$$

The fact that the logarithm $\ln(\mu^2/T^2)$ is a slowly varying function of the temperature was taken into account in (A.3), and, for the sake of convenience, we have introduced the notation $n_0 = \ln(\mu^2/T^2) = \ln(\mu^2/LP)$.[6] As a result, we obtain

$$P^{1/2}T^2\left(\frac{dT}{dP}Q^{1/2} + T\right) = \alpha\left(2P + \frac{1}{2}Q^{1/2}\right)^2.$$

When $P_0, T_0 = \text{const}$, this expression leads to a particular solution with stationary physical parameters (7) and the relation between the constants of the stationary solution:

$$l_g^{-2}(P_0 - \Lambda)$$

$$= [\beta + k_1(4\alpha)^{4/3} + k_2(4\alpha)^{2/3} - k_3(4\alpha)^{1/3}]P_0^2, \tag{A.4}$$

$$T_0^3 = 4\alpha P_0^{3/2}.$$

The solution of the system of algebraic equations (A.4) is

$$P_{01,2} = \frac{B}{2A}\left(1 \pm \sqrt{1 - \frac{4AC}{B^2}}\right), \tag{A.5}$$

where $B = l_g^{-2}$, $C = l_g^{-2}\Lambda$, and $A = \beta + k_1(4\alpha)^{4/3} + k_2(4\alpha)^{2/3} - k_3(4\alpha)^{1/3}$. The solution (A.5) exists if the determinant

$$D = B^2 - 4AC > 0.$$

This corresponds to the restriction on Λ

$$\Lambda \leq \frac{l_g^{-2}}{4[\beta + k_1(4\alpha)^{4/3} + k_2(4\alpha)^{2/3} - k_3(4\alpha)^{1/3}]}. \tag{A.6}$$

Expressions for the physical parameters of the stationary solution follow immediately from (A.4) and (A.5) and take the form (9).

---

[5] For details, see [16].

[6] The convenience of such notation is due to the fact that, under certain circumstances, the dependence of the function n_0 on its argument can be neglected, and this function can be considered constant.

Let us investigate the stability of system (A.3) by imposing small perturbations on the parameters of the stationary solution $P = P_0(1 + p)$ and $T = T_0(1 + s)$. As a result, we obtain

$$\frac{d^2 p}{d\chi^2} + A1 \frac{dp}{d\chi} + A2 = B1, \qquad (A.7)$$

where

$$A1 = 3 - \frac{(4\alpha)^{1/3} k_3}{k_0}, \quad A2 = \frac{3k_3 (4\alpha)^{1/3}}{2} \frac{p}{k_0},$$

$$B1 = \frac{(4\alpha)^{1/3} [4k_1(4\alpha) + 2k_2 - 3k_3] s}{k_0},$$

$$\frac{ds}{d\chi} + 3s = \frac{1}{2} \left[\frac{dp}{d\chi} + p \right], \quad k_0 = k_4 n_0. \qquad (A.8)$$

We will seek solutions of the system (A.7) and (A.8) in the form

$$p = p_0 a^\lambda, \quad s = s_0 a^\lambda.$$

The resulting characteristic equation for λ is cubic. However, due to its degeneracy, we can find one of the roots immediately: $\lambda_3 = -3$. The two other roots are determined by the relation

$$Q(\lambda) = \lambda^2 + A3\lambda + A4 = 0, \qquad (A.9)$$

where

$$A3 = 3 - b,$$

$$A4 = \frac{[P_c^{-1} - 2k_1(4\alpha)^{4/3} - 2k_2(4\alpha)^{2/3} - 2\beta]}{k_0} + 3b,$$

$$P_c^{-1} = P_0^{-1} l_g^{-2}, \quad b = \frac{(4\alpha)^{1/3} k_3}{k_0}.$$

It is also convenient to introduce the notation

$$c = \frac{k_1(4\alpha)^{4/3} + k_2(4\alpha)^{2/3} + \beta}{k_0}.$$

The solution of equation (A.9) is

$$\lambda_{1,2} = -\frac{(3 - b)}{2}$$

$$\pm \sqrt{\frac{(3 - b)^2}{4} - 3b + \frac{[2ck_0 - P_c^{-1}]}{k_0}}. \qquad (A.10)$$

The instability increment γ can be calculated using formula (7). We can see from (A.10) that there are three cases:

(1) When $b \ll 1$ and $k_0 \gg 1$, we obtain

$$\lambda_1 = 0, \quad \lambda_2 = -\frac{3}{2}, \quad \gamma_1 = 0, \quad \gamma_2 = -\frac{3 l_g^{-1} b}{2(c - b) k_0};$$

i.e., the stationary inflationary solution is unstable for $b > c$ and weakly stable otherwise.

(2) When $b \gg 1$, $k_0 \ll 1$, $\Lambda \neq 0$, and $P_c = 2A$, we obtain

$$\lambda_1 = 1, \quad \lambda_2 = b, \quad \gamma_1 = \frac{l_g^{-1}}{(c - b) k_0}, \quad \gamma_2 = \frac{b l_g^{-1}}{(c - b) k_0};$$

i.e., the stationary inflationary solution is unstable for $c > b$.

(3) When $b \gg 1$, $k_0 \ll 1$, $\Lambda = 0$, and $P_c = A$, we obtain

$$\lambda_1 = b, \quad \lambda_2 = \frac{c - b}{2b},$$

$$\gamma_1 = \frac{l_g^{-1}}{2(c - b) k_0}, \quad \gamma_2 = \frac{l_g^{-1}}{2b k_0};$$

i.e., the stationary inflationary solution is unstable.

The analysis conducted above shows that a stable mode is transformed to the unstable one ($\lambda > 0$) at intermediate values of the parameter k_0, when $k_0 \sim 1$. Therefore, the analyzed high-temperature inflationary solution is unstable over a wide range of the model parameters, and, in the general case, does not have a region of dynamic stability.

Equations (A.3) possess another hidden asymptotic symmetry (as $P \longrightarrow \infty$) for the similarity transformations

$$Q^{1/2} \longrightarrow \exp(r) Q^{1/2}, \quad T^2 \longrightarrow \exp(r) T^2, \qquad (A.11)$$

which enables us to conduct the following change of variables:

$$Q^{1/2} = IP, \quad T^2 = LP. \qquad (A.12)$$

After the transformation (A.11), it is convenient to introduce the dimensionless logarithmic curvature variable $x = \ln(P l_g^2)$. As a result, the system of gravitational equations takes the form

$$e^{-x} - \Lambda l_g^2 e^{-2x} + k_4 n_0 \left(II' + 3I + \frac{3}{4} I^2 \right)$$

$$= \beta + k_1 L^2 + k_2 L - k_3 L^{1/2} \left(1 - \frac{I}{2} \right), \qquad (A.13)$$

$$\frac{1}{2} I L^{1/2} L' + \left(1 + \frac{I}{2} \right) L^{3/2} = \alpha \left(2 + \frac{I}{2} \right)^2.$$

Here, a prime denotes derivation with respect to x. Equation (A.13) contains the particular solution corresponding to the birth of the Universe from "nothing," when the quadratic vacuum terms dominate over the matter terms. Using the relations

$$I = I_0 e^{-3x/4}, \quad L = (\alpha I_0)^{2/3} e^{-x/2},$$

we obtain

$$P = \left(\frac{I_0}{4}\right)^4 l_g^{-6}(t - t_0)^4,$$

$$T = (\alpha_1|I_0|)^{1/3} P^{1/4} l_g^{-1/2}, \qquad (A.14)$$

$$\frac{a}{a_0} = ex\left[\frac{l_g^{-3}I_0^2}{48}(t - t_0)^3\right]$$

with the following restrictions on the curvature and constants of the solution:

$$Pl_g^2 < \frac{1}{\alpha}\left(\frac{3n_0k_4}{k_1}\right)^{1/2}$$

or

$$\left[\frac{I_0}{4}(t - t_0)l_g^{-1}\right]^4 < \frac{1}{\alpha}\left(\frac{3n_0k_4}{k_1}\right)^{1/2}.$$

REFERENCES

1. B. S. De Witt, Phys. Rep. D **9**, 341 (1975).

2. A. A. Grib, S. G. Mamaev, and V. M. Mostepanenko, *Vacuum Quantum Effects in Strong Fields* [in Russian] (Énergoatomizdat, Moscow, 1988).

3. N. D. Birrell and P. C. W. Davies, *Quantum Fields in Curved Space* (Cambridge University Press, Cambridge, 1982; Mir, Moscow, 1984).

4. Ya. B. Zel'dovich and A. A. Starobinskiĭ, Pis'ma Zh. Éksp. Teor. Fiz. **26**, 373 (1977).

5. V. A. Beĭlin, G. M. Vereshkov, Yu. S. Grishkan, N. M. Ivanov, and A. N. Poltavtsev, Zh. Éksp. Teor. Fiz. **78**, 2081 (1980).

6. G. M. Vereshkov, Yu. S. Grishkan, N. M. Ivanov, and A. N. Poltavtsev, Zh. Éksp. Teor. Fiz. **80**, 1665 (1981).

7. G. M. Vereshkov, Yu. S. Grishkan, A.V. Korotun, and A. N. Poltavtsev, Probl. Teor. Grav. Élemen. Chast. (Énergoatomizdat, Moscow, 1986), issue 17, p. 47.

8. L. Parker, Ann. N.Y. Acad. Sci. **262** (1975).

9. S. M. Christensen, Phys. Rev. D **17**, 946 (1978).

10. Yu. S. Grishkan, Candidate of Science (Phys.-Math.) Dissertation, Mosow State University (Moscow, 1983).

11. V. Ts. Gurovich and A. A. Starobinskiĭ, Zh. Éksp. Teor. Fiz. **77**, 1683 (1979).

12. A. A. Starobinsky, Phys. Lett. B **91**, 99 (1980).

13. J. Z. Simon, Phys. Rev. D **45**, 1953 (1992).

14. Yu. S. Grishkan, Astron. Zh. **59**, 833 (1982).

15. G. M. Vereshkov and A. N. Poltavtsev, Zh. Éksp. Teor. Fiz. **71**, 3 (1976).

16. E. G. Vertogradova and Yu. S. Grishkan, Izv. Vuz., No. 3, 64 (1998).

17. L. V. Ovsyannikov, *Group Analysis of Differential Equations* [in Russian] (Nauka, Moscow, 1979).

18. D. Kramer, H. Stefani, M. Mac Callum, *et al.*, *Exact Solutions of the Einstein Equations* [in Russian] (Énergoizdat, Moscow, 1982).

19. P. K. Rashevskiĭ, *Riemann Geometry and Tensor Analysis* [in Russian] (Nauka, Moscow, 1964).

20. L. P. Grishchuk and Ya. B. Zel'dovich, *Proceedings of the Second Seminar: A Quantum Theory of Gravity* [in Russian] (IYaI, Moscow, 1982), p. 39.

21. Ya. B. Zel'dovich and I. D. Novikov, *Relativistic Astrophysics*, Vol. 2: *The Structure and Evolution of the Universe* (Chicago Univ., Chicago, 1983).

22. D. N. Schramm, *After the First Three Minutes* (American Institute of Physics, New York, 1991), p. 12.

Translated by Yu. Dumin

The Bulk Motion of FGC Galaxies on Scales of 100 Mpc

I. D. Karachentsev[1], V. E. Karachentseva[2], Yu. N. Kudrya[2], and S. L. Parnovskiĭ[2]

[1] *Special Astrophysical Observatory, Nizhniĭ Arkhyz,*
Republic of Karachaevo-Cherkessia, Russia
[2] *Astronomical Observatory, Kiev University,*
ul. Observatoriya 3, Kiev, 252053 Ukraine
Received March 1, 1999

Abstract—Large-scale streaming is analyzed using a sample of 983 thin, edge-on galaxies from the FGC catalog with radial velocities $cz < 18000$ km s^{-1}. The catalog covers the entire sky and contains galaxies with apparent axial ratios $a/b > 7$ and angular diameters $a > 0.6$ arcmin. The distances to the galaxies were determined using a multi-parameter "rotation amplitude–linear diameter" relation, which is similar to the Tully–Fisher relation and takes into account surface brightness, morphological type, and other global parameters. The bulk motion of the galaxy sample with respect to the frame of the microwave background radiation can be described by a dipole solution with amplitude $V^B = 300 \pm 75$ km s^{-1} in the direction ($l = 328°$, $b = +7°$) $\pm 15°$. The apex parameters for the FGC galaxies agree well with the amplitude and direction of the bulk motion for the Mark III compiled catalog, although the two samples have no objects in common. The dipole solution provides only a rough approximation to the smoothed peculiar-velocity field of the FGC galaxies. Areas of maxima and minima on the V_{pec} map are not correlated with the locations of known nearby clusters and voids. A comparison of nearby and distant subsamples shows that the amplitude of the bulk motion with respect to the 3K reference frame does not decrease with distance. The observed large-scale galaxy streaming could be due to the Shapley concentration of rich clusters (311°, +30°), which is located within 2σ of the apex. © *2000 MAIK "Nauka/Interperiodica".*

1. INTRODUCTION

The analysis of peculiar galaxy motions is a key tool in understanding the origin and evolution of the large-scale structure of the Universe. Measurements of coherent large-scale galaxy motions can be used to test cosmological models, since the amplitude of such motions is directly related to the power spectrum of density fluctuations [1]. See the review [2] for a detailed discussion of theoretical aspects of this problem and analyses of redshift catalogs and lists of peculiar galaxy velocities. Recall that peculiar radial velocities are defined as $V_{pec} = cz - Hr$, where Hr is the distance of an individual galaxy in km s^{-1} measured independently of its redshift z. In this case, the specific value of the Hubble constant H is not important.

Individual galaxy distances are usually estimated using the Tully–Fisher or Faber–Jackson relations for spiral and elliptical galaxies, respectively, or various combinations thereof. Application of these methods to large galaxy samples requires accurate allowance for various selection effects. Thus far, there is no consensus of opinion about either the amplitude and direction of bulk motions or the spatial scales of this phenomenon. The variety of published results and inconsistencies between them have several origins: different depths and morphological compositions for the samples considered, the use of different calibrations in independent determinations of galaxy distances (field and cluster galaxies), observational selection effects, etc.

The need for a large galaxy sample with homogeneous peculiar-velocity data led to the compilation of the Mark III catalog [3], which contains about 3000 field and cluster galaxies observed by various authors (see references in [4]), with each sample recalibrated and corrected for selection effects. The main problem with merging the galaxy samples was the different photometric limits of the catalogs [5–7] used as sources for the initial samples. It was also necessary to take into account internal extinction in spiral galaxies with arbitrary inclinations to the plane of the sky [3].

The FGC catalog of flat edge-on spirals [8] is a fundamentally new sample compiled especially to study large-scale coherent motions. See [9] for a discussion of the advantages of using this class of strongly inclined spirals. The catalog is the result of a systematic search for flat, edge-on galaxies on the O, E prints and J, R films of the POSS-I and ESO/SERC surveys, respectively. The catalog covers the entire sky and contains a total of 4455 spiral galaxies with minimum "blue" diameters $a_{lim} = 0.6$ arcmin and apparent axial ratios $a/b \geq 7$. Note that, due to the specific properties of the FGC catalog, it has virtually no objects in common with the galaxy lists included in the Mark III compilation.

Earlier [10], we obtained a dipole solution for the amplitude and direction of the bulk motion of 893 FGC galaxies with observed HI radio line widths or optical rotation curves. We estimated the galaxy distances
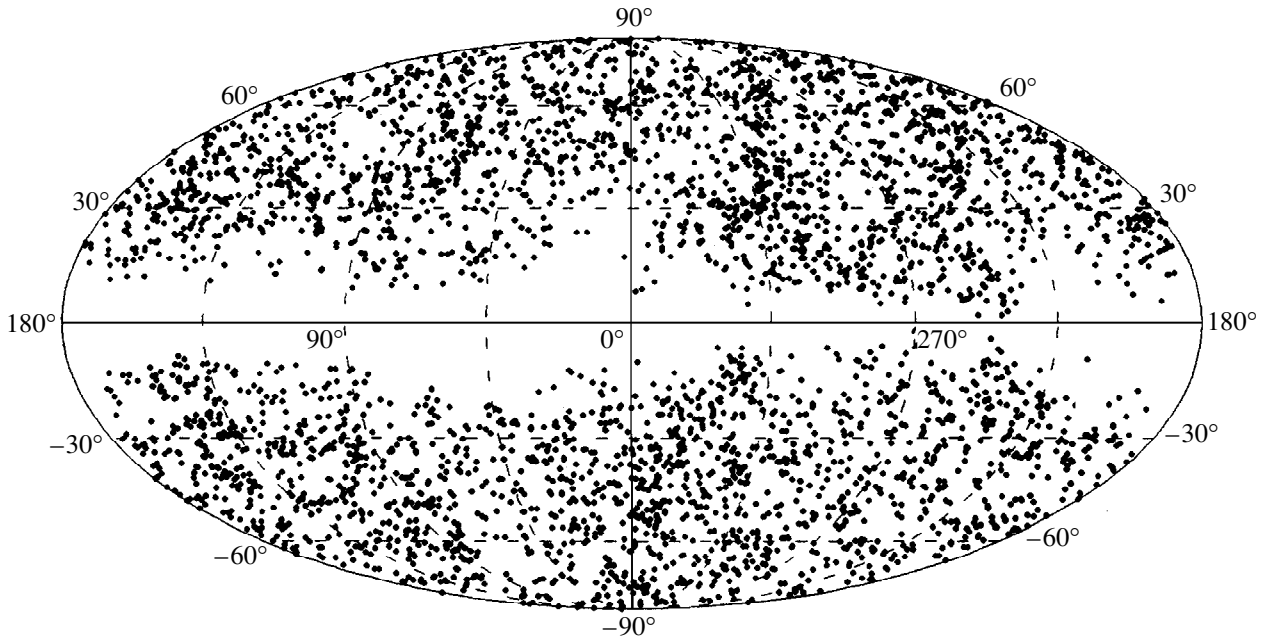
Fig. 1. Distribution of FGC galaxies in Galactic coordinates.

using the Tully–Fisher relation and inferred the following bulk-motion parameters for the sample considered: $|V^B| = (260 \pm 40)$ km s^{-1}; $l = 319° \pm 10°$, and $b = +28° \pm 11°$.

The aims of the current paper are (1) to determine the bulk-motion parameters for the new, expanded sample of flat galaxies using both the Tully–Fisher relation and a generalized multiparameter regression; (2) to compare our results with those of other studies; and (3) to map the peculiar-velocity field of FGC galaxies.

2. THE SAMPLE

Analyses of the FGC catalog showed that these thin, edge-on galaxies are distributed rather uniformly throughout the sky, except for a zone of avoidance in the Milky Way. The catalog is 90% complete down to an angular diameter of $a = 0.9$ arcmin and exhibits no biases in morphological type as a function of limiting magnitude [11–13].

Figure 1 shows the overall sky distribution of the flat galaxies in Galactic coordinates. We reduced the angular diameters of southern galaxies to the FGG system in accordance with the procedure used in [13] in order to allow for the different effective depths of the ESO and POSS-I surveys. We then supplemented the sample [10] with galaxies with recently measured rotation curves [14]. To this end, we used the relation from [15] between the amplitude of the optical rotation curve $V_{\max}$ and the width W_{50} of the 21-cm hydrogen radio line. We also added the results of optical and radio observations of southern galaxies from [16] after converting their $V_{\max}$ into W_{50} in accordance with [17].

These supplements somewhat reduced the nonuniformity of the sky distribution of our sample: More than half of all the galaxies are located within $0 \le \delta \le 38°$ and can therefore be observed by the 305-m Arecibo telescope [18].

Figure 2 shows the sky distribution (in Galactic coordinates) of flat galaxies with measured radial velocities and HI line widths. The sample contains a total of 983 galaxies: 929 and 54 objects in the main catalog and the supplement, respectively. We used the following parameters to describe the galaxies of our sample:

l, b—Galactic coordinates corresponding to the Cartesian coordinates e_x, e_y, and e_z of the unit vector pointing in the direction of the galaxy $e_x = \cos b \cos l$, $e_y = \cos b \sin l$, and $e_z = \sin b$;

a_c, a_k, b_c, b_k—the "blue" and "red" angular sizes (major and minor axes) in arcmin reduced to the POSS-I photographic system [13] and corrected for inclination and Galactic extinction as described in [19];

$cz \equiv V_{3K}$—the radial velocity (in km s^{-1}) in the frame of the microwave background radiation, derived from the measured radial velocity V_h using the formula given in [20];

W—the HI full width at half maximum (in km s^{-1}), with the standard correction for cosmological and turbulent broadening;

T—the number code of the morphological type of the galaxy (Sc corresponds to $T = 5$);

Σ—a discrete index (1 to 4) characterizing the surface brightness;

As—an index quantifying the galaxy's asymmetry (0 to 2).
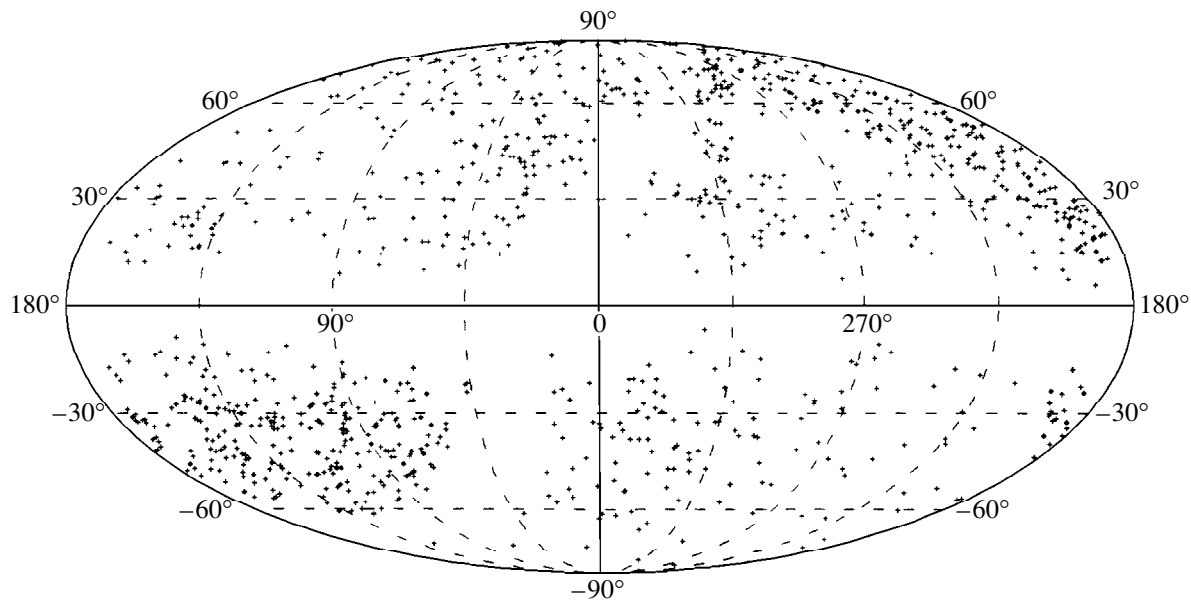
Fig. 2. Sky distribution of 983 FGC galaxies with measured radial velocities. Diamonds indicate objects from the supplement to the main catalog.

We determined the last three parameters only for galaxies from the main catalog. The average values for our subsample are $\langle T \rangle = 5.7$, $\langle \Sigma \rangle = 2.1$, and $\langle As \rangle = 0.35$, i.e., close to the corresponding mean parameters for the entire catalog [8]: $\langle T \rangle = 5.5$, $\langle \Sigma \rangle = 2.3$, and $\langle As \rangle = 0.34$ [11]. Table 1 lists the mean, variance, skewness, and kurtosis of the distributions for the corrected "blue" and "red" angular diameters, radial velocities, and hydrogen-line widths for the sample of 983 flat galaxies we used to derive the parameters of the bulk motion.

3. DETERMINATION OF THE BULK MOTION USING THE TULLY–FISHER TECHNIQUE

We derived direct one- and two-parameter Tully–Fisher relations by applying a least squares method separately to the blue and red corrected diameters:

$$\log(acz) = \alpha + \beta \log W \qquad (1)$$

(one-parameter regression) and

$$\log(acz) = \alpha + \beta \log W + \gamma \Sigma \qquad (2)$$

(two-parameter regression). After excluding 15 galaxies that deviated by more than 3σ from the direct and inverse regression lines, we derived the one- and two-parameter blue and red Tully–Fisher relations presented in Table 2. The columns give, in addition to α, β, and γ, the standard error of the logarithm of the distance and the rms peculiar velocity. The lower part of the table gives the corresponding parameters for the same sample after excluding members of the Local Supercluster with $cz < 2500$ km s^{-1}.

It is clear from these data that the slope β of the relation between the linear diameter and the amplitude of

internal motions in flat galaxies is close to unity. The derived distances had the lowest standard errors when they were computed using the two-parameter red regression, which we used to determine the final distances Hr and radial peculiar velocities $V_{pec} = cz - Hr$. Figure 3 plots the galaxy distances $Hr \equiv V_{TF}$ derived from the two-parameter red regression as a function of the measured velocities $cz \equiv V_{3K}$ in the frame of the 3K background. We then applied the procedure of [10] to the V_{pec} values and sky positions of all the galaxies to obtain a least-squares solution for the components of the bulk-motion vector $\mathbf{V}^B$ in the microwave-background frame and the corresponding amplitude and direction (apex) of the large-scale galaxy motion.

The results are summarized in Table 3. These clearly demonstrate that the sample of FGC galaxies with measured velocities is moving with respect to the microwave background at a velocity of (386 ± 80) km s^{-1} toward Centaurus ($l = 320° \pm 13°$, $b = 10° \pm 11°$). If we exclude the nearest galaxies in order of increasing heliocentric distance, the dipole amplitude remains approximately constant, whereas the direction of the streaming drifts slightly in both Galactic longitude and latitude. We estimated the errors of the amplitude and direction of the dipole solution $\mathbf{V}^B$ listed in the table from the marginal errors of its components V_x^B, V_y^B, and V_z^B obtained by orthogonally projecting the error ellipsoid onto the plane of the sky. The second part of Table 3 gives the corresponding parameters for the apex of the large-scale streaming motion of the FGC galaxies in the frame of the Local Group.

It is obvious that the method could be somewhat improved by including, in addition to surface bright-

ness, additional terms in regression (1) to allow for the morphological type, apparent axial ratio, and other galaxy parameters. However, the disadvantage of this approach is that the components of the $\mathbf{V}^B$ dipole are not derived simultaneously with the parameters of the Tully–Fisher relation. In this case, the nonuniform distribution of the galaxy sample on the sky could result in systematic errors in the parameters of the dipole solution.

4. GENERALIZED REGRESSION METHOD AND DIPOLE PARAMETERS

In the method described below, we simultaneously estimate the parameters of the regression relations for the galaxy distances and large-scale galaxy streaming velocities. We used a multiparameter regression with terms included only if they were statistically significant.

We will write the measured radial velocity of each galaxy in the frame of the 3K background radiation as a sum of three terms: (1) isotropic Hubble expansion, Hr; (2) projection of the bulk motion, $V^B \cos \varphi$; and (3) a random small-scale (virial) component ε_V, which includes the error in the measured value for Hr,

$$cz = Hr$$
$$+ (V_x^B \cos l \cos b + V_y^B \sin l \cos b + V_z^B \sin b) + \varepsilon_V. \quad (3)$$

We used the following slightly modified Tully–Fisher relation to estimate the redshift-independent distances, Hr:

$$Hr = c_1 W^\beta / a. \quad (4)$$

According to Table 2, β is very close to unity, and we accordingly adopt $\beta = 1$ and add a quadratic term to allow for possible nonlinearity in W^2:

$$Hr = c_1 W/a + c_2 (W/a)^2. \quad (5)$$

This allows the coefficients c_i and their errors to be estimated using a linear regression procedure. We added additional terms to (5) in order to allow for the possible dependence of the estimated Hr on other observables:

$$Hr = \sum_{i=1}^{n} c_i Z_i(a_c, a_k, W, \Sigma, T, a/b, As, \ldots). \quad (6)$$

The most difficult problem is correct choice of the functions Z_i. Here, we took W/a_k and $(W/a_k)^2$ for Z_1 and Z_2 and added various combinations of other observables that satisfy the obvious minimum requirements; e.g., that the galaxy velocities should increase with decreasing angular size. We then applied a least squares method to obtain the coefficients c_i that minimized the sum of the squared residuals ε_V^2 in (3). We used a Fisher criterion to determine the statistical significance of each regressor in (6) and left only significant terms. We repeated this procedure several times until we obtained

Table 1. Distribution of observed parameters of 983 galaxies

Parameter	Mean	σ	γ_1	γ_2
a_c, arcmin	1.31	0.99	4.7	36.1
a_k, arcmin	1.23	0.92	4.5	32.7
cz, km s^{-1}	5760	3070	0.51	0.054
W, km s^{-1}	290	112	0.59	0.004

Table 2. Parameters of the Tully–Fisher regression

Regression	N	α	β	γ	$\sigma(\log Hr)$	$\sigma(V_{pec})$
$cz > 0$						
a_c, W	965	1.14 ±0.05	1.07 ±0.02	–	0.112	1440
a_k, W	965	1.01 ±0.05	1.11 ±0.02	–	0.112	1380
a_c, W, Σ	913	1.04 ±0.05	1.09 ±0.02	0.022 ±0.005	0.110	1400
a_k, W, Σ	913	0.94 ±0.05	1.12 ±0.02	0.015 ±0.005	0.110	1350
$cz > 2500$ km s^{-1}						
a_c, W	808	1.40 ±0.05	0.97 ±0.02	–	0.098	1530
a_k, W	808	1.27 ±0.06	1.01 ±0.02	–	0.096	1470
a_c, W, Σ	767	1.30 ±0.06	0.99 ±0.02	0.019 ±0.005	0.096	1490
a_k, W, Σ	767	1.19 ±0.06	1.03 ±0.02	0.012 ±0.005	0.095	1440

Table 3. Amplitude and direction of the bulk motion of the galaxies

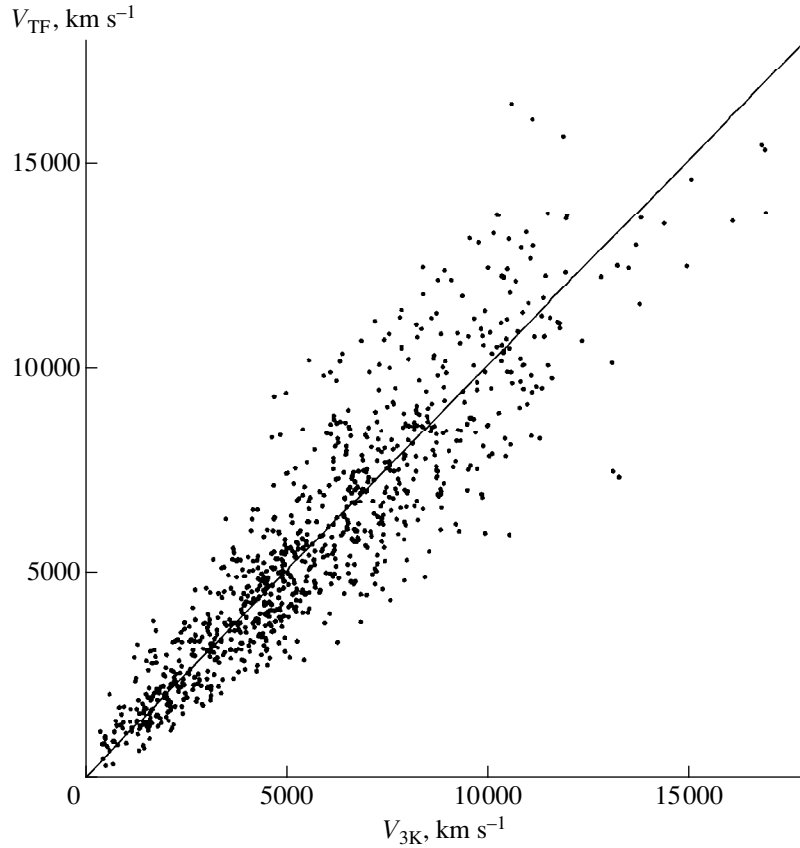| Hr, km s^{-1}	N	V^B, km s^{-1}	l, deg	b, deg
In the microwave-background frame				
>0	913	386 ± 80	320 ± 13	10 ± 11
>2500	773	398 ± 92	321 ± 14	12 ± 13
>5000	494	406 ± 120	341 ± 19	33 ± 18
>7500	253	440 ± 205	39 ± 27	32 ± 20
In the rest frame of the Local Group				
>0	915	466 ± 84	23 ± 11	−37 ± 11
>2500	766	495 ± 100	12 ± 14	−40 ± 12
>5000	483	605 ± 168	342 ± 18	−27 ± 14
>7500	245	903 ± 325	325 ± 20	−40 ± 14

Fig. 3. Tully–Fisher distances [relation (2)] as a function of the measured radial velocities.

a set of six regressors whose Fisher significance coefficients satisfy the rigid condition $F_1 > 10$ (the confidence probability exceeds 99%).

The results are summarized in Table 4. To estimate the c_i and their standard errors $\sigma(c_i)$, we excluded from the initial sample of 929 galaxies only 10 objects that deviated by more than 3σ from the statistical relation. The remaining objects yielded the relation

$$cz = (W/a_k)$$
$$\times (c_1 + c_2 W/a_k + c_3 \Sigma + c_4/W + c_5 T\Sigma + c_6 a_k/b_k) \quad (7)$$
$$+ V_x^B \cos l \cos b + V_y^B \sin l \cos b + V_z^B \sin b + \varepsilon_V.$$

Figure 4 plots the velocity $V_{reg} \equiv Hr$ derived from regression formula (7) as a function of the measured

Table 4. Terms of the generalized regression

i	Z_i	c_i	$\sigma(c_i)$	F_i
1	W/a_k	24.5	1.0	564
2	$(W/a_k)^2$	−0.0106	0.00094	126
3	$\Sigma W/a_k$	1.76	0.20	79
4	$1/a_k$	−832	120	48
5	$\Sigma TW/a_k$	−0.72	0.14	27
6	$(a_k/b_k)W/a_k$	0.23	0.06	12

radial velocity $V_{3K} \equiv cz$ in the 3K background frame. The scatter in this relation for the FGC galaxies is much smaller than the corresponding scatter in Fig. 3.

The six statistically significant regressors are listed in Table 4 in order of decreasing significance. It is evident from this table that the nonlinearity of the Tully–Fisher relation is more important than its surface-brightness dependence. The negative value for c_2 indicates that the linear regression systematically underestimates the linear sizes and, consequently, the distances, of giant galaxies compared to their dwarf counterparts. This effect is expected if internal extinction is stronger in giant edge-on spirals that in dwarf galaxies with the same tilt. A number of authors have already provided observational evidence for this effect [21, 22]. The last two regressors in Table 4 suggest that the relation depends weakly but significantly on the morphological type and apparent axial ratio (tilt) of the flat galaxies.

We determined the parameters listed in Table 4 simultaneously with the components of the bulk motion of the galaxy sample. The entire sample of flat galaxies yielded the results

$$V_x^B = 252 \pm 74 \text{ km s}^{-1}, \quad V_y^B = -157 \pm 81 \text{ km s}^{-1},$$

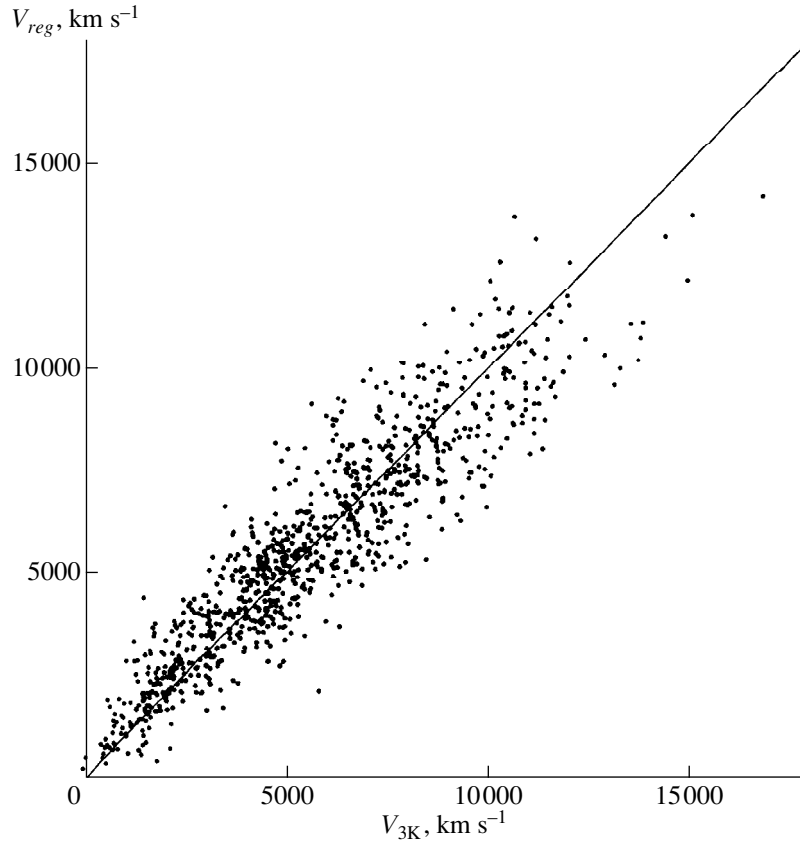$$V_z^B = 37 \pm 63 \text{ km s}^{-1}.$$

Fig. 4. Velocities of FGC galaxies derived using regression (7) as a function of the measured radial velocities.

The galaxy streaming has a velocity of 300 km s^{-1} toward $l = 328°$, $b = +7°$, and the rms peculiar velocity is $\sigma_V = 1160$ km s^{-1}.

Omitting the Z_2 term, which is nonlinear with distance, makes the Z_4 term statistically insignificant. In this case, only three regressors remain in relation (6), apart from W/a_K (the apparent axial ratio, surface brightness, and morphological type); the corresponding parameters are listed in Table 5. The resulting "truncated" linear regression

$$cz = (W/a_K)(c_1 + c_2 a_K/b_K + c_3 \Sigma + c_4 T\Sigma) \\ + V^B \cos\varphi + \varepsilon_V \qquad (8)$$

depends on fewer, reliably chosen parameters and looks more like a classical Tully–Fisher relation. The rms peculiar velocity increases to $\sigma_V = 1240$ km s^{-1} and the new components of the bulk motion are

$$V_x^B = 275 \pm 78 \ \text{km s}^{-1}, \quad V_y^B = -224 \pm 86 \ \text{km s}^{-1},$$

$$V_z^B = 85 \pm 67 \ \text{km s}^{-1},$$

implying a velocity of 365 km s^{-1} toward $l = 321°$, $b = +14°$. We can see that all three methods—(2), (7), and (8)—yield similar amplitudes and directions for the bulk galaxy motion.

We now estimate the errors in the amplitude and direction of the bulk motion using relation (7) as an example. Standard statistical methods can be used to derive the parameters of the 1σ nine-dimensional (three velocity components and six functions) error ellipsoid. We then project this ellipsoid onto the three-dimensional velocity space to obtain the three-dimensional marginal-error ellipsoid, which we can then use to determine the unknown errors. The innermost and outermost ellipsoid points determine the marginal boundaries of the bulk velocity, which are 225 km s^{-1} < V^B < 374 km s^{-1}. The marginal boundaries of the 2σ and 3σ ellipsoids are 151 km s^{-1} < V^B < 450 km s^{-1} and 79 km s^{-1} < V^B < 527 km s^{-1}, respectively. It follows that the bulk velocity differs from zero at the 4σ significance level.

Some idea of the error in the bulk velocity is given by Fig. 5, which shows the section of the three-dimensional ellipsoid made by the $l = 328°$ meridian passing through the apex (solid line). We estimated the error of the bulk-velocity apex by determining the boundaries of the projection of the marginal-error ellipsoid onto the plane of the sky. Figure 6 shows the boundaries of the 1σ, 2σ, and 3σ full-regression ellipsoids. The errors in the amplitude and direction of the bulk motion

Table 5. Terms of the truncated regression

i	Z_i	c_i	$\sigma(c_i)$	F_i
1	W/a_k	14.9	0.55	738
2	$(a_k/b_k)W/a_k$	0.43	0.07	43
3	$\Sigma W/a_k$	1.36	0.21	43
4	$\Sigma TW/a_k$	−0.82	0.14	33

Table 6. Amplitude and direction of the dipole solution for the bulk motion

Velocity interval, km s^{-1}	N	$\sigma(V_{pec})$, km s^{-1}	V^B, km s^{-1}	l, deg	b, deg
Full regression					
Whole sample	919	1160	300	328	7
$Hr < 3500$	206	750	324	309	−8
$3500 < Hr < 5500$	258	1000	294	338	−16
$5500 < Hr < 7500$	214	1150	477	303	30
$7500 < Hr$	241	1530	463	348	−3
Truncated regression					
Whole sample	919	1240	365	321	14
$Hr < 3500$	234	810	403	288	−16
$3500 < Hr < 5500$	263	1020	309	344	8
$5500 < Hr < 7500$	193	1220	755	307	29
$7500 < Hr$	229	1620	415	5	10

derived using the truncated regression differ only slightly from the above values.

Table 6 summarizes our determinations of the amplitude and direction of the bulk motion of FGC galaxies. To estimate the possible dependence of the apex parameters on the survey depth, we subdivided our sample into four approximately equal Hr distance-lim-
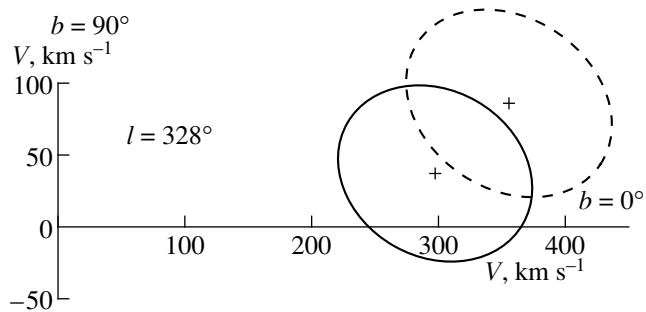

Fig. 5. Section of the bulk-velocity error ellipsoid made by the $l = 328°$ meridian passing through the apex. The solid and dashed lines correspond to the full (7) and truncated (8) regressions, respectively.

ited subsamples. The amplitude of the bulk motion does not exhibit the characteristic decrease with spatial volume expected in many cosmological models. This result is independent of the regressors used to determine the apex parameters.

Previously published parameters for dipole solutions for large-scale galaxy streaming are listed in Table 7. The first three columns give the estimated amplitude and direction of the dipole with respect to the 3K background frame. The following columns give the number, type, and radial-velocity interval of the galaxies (clusters) in the sample considered. We included in this table only the most representative samples, covering at least half the sky. The corresponding apices in Fig. 6 [23–29] are shown by the diamonds, with numbers indicating the references from Table 7. The filled circles indicate the most representative nearby clusters: Centaurus, Hydra, Pavo-Indus, Pisces, Perseus, Coma, and Hercules, and also the Shapley supercluster. The gray circle shows the region occupied by the well-known Bootis void. The amplitude and direction of our apex solution agrees satisfactorily with the previously published estimates. Only one apex estimate [28] lies outside the 3σ confidence interval for our dipole solution. The closest to our apex in terms of both the amplitude and direction of the galaxy streaming is the result of Dekel *et al.* [29], based on the Mark III data. This very good agreement (to within about 1σ) is rather surprising, especially in view of the fact that our sample and the Mark III compilation have no galaxies in common.

5. THE PECULIAR RADIAL-VELOCITY FIELD

Given the peculiar galaxy velocities, we can map the V_{pec} distribution in Galactic coordinates and reconstruct the positions of high-density and low-density regions (attractors and voids). This is the subject of a separate detailed analysis, and we discuss only some preliminary results here.

We cannot depict the three-dimensional peculiar-velocity field, and therefore restrict our analysis to its projection onto the plane of the sky, without paying attention to the galaxy distances. To construct the velocity field, we compute the weighted mean of the peculiar velocities by averaging over all galaxies with the following statistical weights:

$$V(l, b) = \sum V_i w_i / \sum w_i, \qquad (9)$$

where

$$w_i = \exp(-\sin^2\theta_i / \sin^2\theta_0) \text{ if } \theta_i < 3\theta_0$$
$$w_i = 0 \text{ if } \theta_i > 3\theta_0.$$

Here, θ_i is the angle between the direction l, b and the sky position of the ith galaxy. We adopted $\theta_0 = 30°$. Smaller θ_0 values yield velocity fields with closely spaced maxima and minima due primarily to statistical noise. Figure 7 shows contours of equal peculiar veloc-
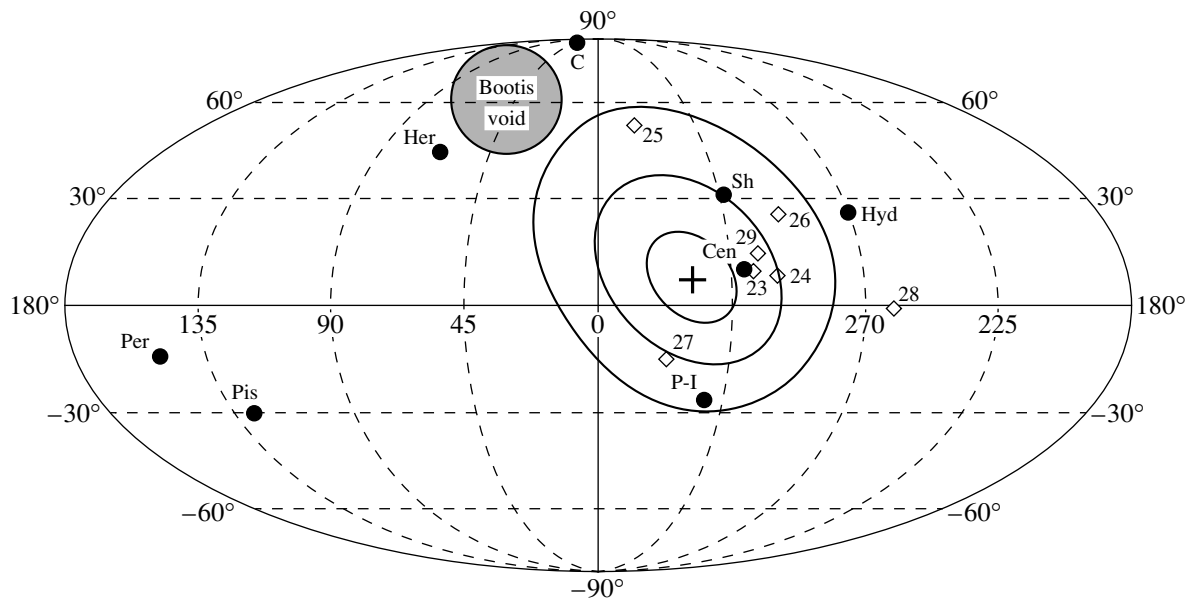
Fig. 6. The apex of the FGC galaxies (cross) and its 1σ, 2σ, and 3σ confidence intervals. The diamonds show the apices for other samples and the numbers are the references in Table 7. The circles indicate nearby clusters of galaxies and the Bootis void.
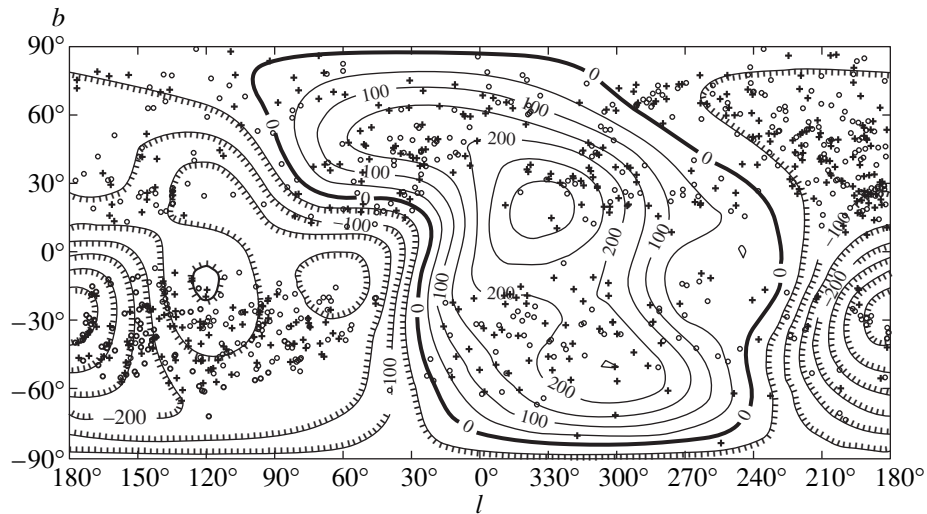

Fig. 7. The distribution of FGC galaxies with positive (crosses) and negative (circles) peculiar velocities in Galactic coordinates. The contours of mean velocity are drawn at 50 km s^{-1} intervals.

ity. The smooth and jagged curves correspond to positive and negative mean peculiar velocities, respectively. We use the l, b Cartesian sky projection, so that the upper and lower sides of the rectangle correspond to the Galactic poles. The circles and crosses show the positions of galaxies with negative and positive radial peculiar velocities, respectively. Figure 8 is a three-dimensional depiction of the $V_{pec}(l, b)$ field.

We can see from Figs. 7 and 8 that the apex of the dipole solution ($328°$, $+7°$) is located in the immediate vicinity of the absolute maximum of the $V_{pec}(l, b)$ field, whereas the antiapex ($148°$, $-7°$) is $\sim 40°$ from the absolute minimum ($180°$, $-30°$). On the whole, the dipole solution provides only a coarse approximation to the peculiar velocity map shown in the figure. We will not attempt to interpret the V_{pec} profile here, and, in particular, estimation of the quadruple component is beyond the framework of this paper.

We computed the above maps by averaging the peculiar velocities over areas of sky independent of the

Table 7. Published apex values

V^B, km s^{-1}	l, deg	b, deg	N	Sample	Reference
570	307°	+9°	400	E, 3200–8000	Lynden-Bell *et al.* [23]
455	299	+8	689	E + S, 0–8000	Hudson [24]
689	343	+52	124	Clusters, 0–15000	Lauer, Postman [25]
200	295	+25	1289	S, 0–6500	Giovanelli *et al.* [26]
310	337	−15	374	S in 24 clusters, 1000–9200	Giovanelli *et al.* [27]
630	260	−1	699	E and S in clusters, 3000–14000	Hudson *et al.* [28]
370	305	+14	~3000	Mark III, 0–5000	Dekel *et al.* [29]
300	328	+7	983	FGC galaxies, 0–18000	This paper

galaxy distances. To analyze the distance dependence of the V_{pec} field, we averaged the data separately over four distance-limited subsamples: $Hr \le 3500$ km s^{-1}; 3500 km s$^{-1} \le Hr \le 5500$ km s^{-1}; 5500 km s$^{-1} \le Hr \le 7500$ km s^{-1}; and $Hr \ge 7500$ km s^{-1}. The resulting apex parameters are summarized in Table 6. Figure 9 shows the corresponding $V_{pec}(l, b)$ maps in order of increasing Hr from top to down.

The distribution of maxima and minima for these peculiar-velocity-field sections exhibit rather complex patterns. Without going into detail, we point out some of the main features of the velocity maps.

(1) The nearest ($Hr \le 3500$ km s^{-1}) and farthest ($Hr \ge 7500$ km s^{-1}) subsamples exhibit the most conspicuous global V_{pec} maxima. The global maxima in the intermediate-distance samples split into two to three local peaks whose centroids are in approximately the same region. The global maximum ($l = 310°$, $b = +15°$) is located between the Centaurus cluster ($cz \sim 4200$ km s^{-1}) [23] and the Shapley supercluster (~14000 km s^{-1}) [30], and the total gravitational force of these features could be responsible for the well-known Great Attractor effect.

(2) The region of negative V_{pec} in the above sections appears less stable and more multiply connected. The locations of minima of V_{pec} are completely uncorrelated with the position of the giant Bootes void.

(3) Given the adopted width of the window averaging function ($\theta_0 = 30°$), the four Hr distance-limited sections yield the following V_{pec} intervals: +400 to –300 km s^{-1}; +350 to –300 km s^{-1}; +500 to –400 km s^{-1}, and +900 to –700 km s^{-1}. The positive and negative extremes of V_{pec} are more or less symmetric with respect to zero; however, their amplitude does not decrease with distance.
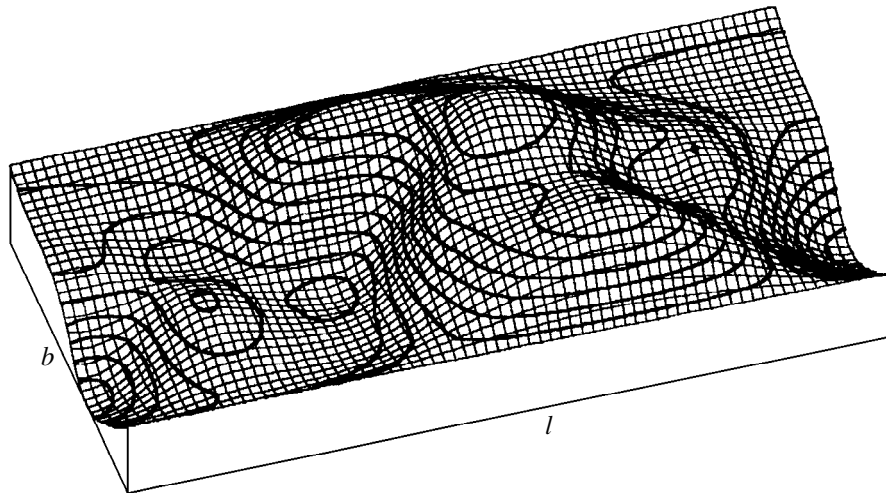

Fig. 8. Three-dimensional profile of the averaged field of the peculiar velocities in the 3K-radiation frame in Galactic coordinates. The orientation of l, b is the same as in Fig. 7.
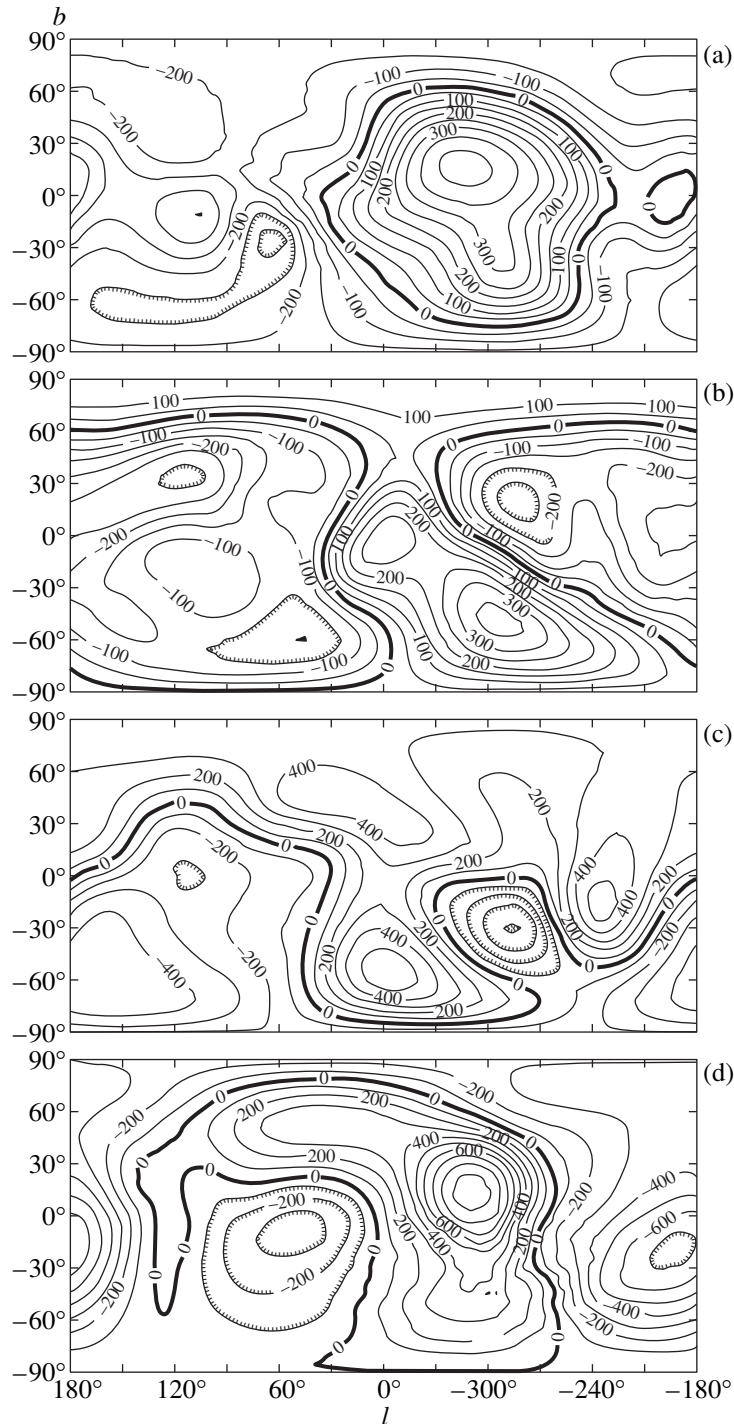
Fig. 9. The peculiar-velocity field in Galactic coordinates for four distance-limited subsamples: (a) $Hr < 3500$ km s^{-1}; (b) $3500 < Hr < 5500$ km s^{-1}; (c) $5500 < Hr < 7500$ km s^{-1}; and (d) $Hr > 7500$ km s^{-1}.

6. CONCLUSION

We have used a sample of 983 thin, edge-on spiral galaxies with measured radial velocities and rotation-curve amplitudes to determine the amplitude and direction of their bulk velocity on scales of ~100 Mpc. To this end, we used various regression relations between observ-able parameters and the galaxy distances. The FGC galaxies exhibit a streaming motion with a velocity of $V^B = (300 \pm 75)$ km s^{-1} toward ($l = 328°$, $b = +7°$) $\pm 15°$ with respect to the frame of the cosmic background radiation. This result is in satisfactory agreement (within $\pm 3\sigma$) with previously published apex parameters [23, 24, 26, 27, 29]. Our amplitude and direction

for the bulk motion agrees best with the results obtained by analyzing the Mark III galaxy sample [29] (370 km s^{-1}; 305°, +14°). Note, however, that our sample has no objects in common with the Mark III compilation.

The regions of positive and negative V_{pec} in our smoothed map of the galaxy peculiar velocities exhibit a rather complex pattern, with a dipole solution providing only a coarse approximation. The zones of extrema of V_{pec} bear no obvious association to known clusters and voids.

We subdivided our sample into four approximately equal distance-limited subsamples in order to derive the corresponding independent apex parameters. The resulting apices agree to within the errors. It is safe to say that the velocity of the bulk motion of the galaxies with respect to the 3K background frame does not decrease with distance in the interval $Hr < 10000$ km s^{-1}. This result is at variance with the predictions of many cosmological models. The direction of the bulk motion of FGC galaxies derived here differs substantially from the gravitational dipoles (259°, +34°) for IRAS point sources [31] and rich X-ray clusters (250°, +12°) [32]. However, it follows from Fig. 1 that there is some excess concentration of FGC galaxies in a wide vertical band near $l = 320°$. This low-contrast pattern of field galaxies (not outlined by rich clusters) is capable of producing the observed galaxy streaming. Another, more distant, attractor could be the well-known Shapley concentration of rich clusters [30] with $cz \sim 14000$ km s^{-1}, which is located 28° (i.e., 2σ) from the apex of the FGC galaxy stream.

We consider it important to note the promise of the FGC as a tool for studies of galaxy streaming on scales of 100–200 Mpc. Currently, about 80% of the FGC galaxies, primarily faint and distant ones, lack radial velocities and hydrogen-line widths W. We determined the parameters of the large-scale galaxy streaming based only on angular sizes and other catalogued parameters. The experience of other studies leads us to believe that the accuracy of the peculiar velocities of FGC galaxies could be improved substantially by systematic I-band CCD photometry of these objects.

The FGC catalog remains the deepest and most homogeneous sample of field spirals covering both the Northern and Southern sky, and, as such, remains a tool of fundamental importance for investigations of large-scale streaming.

REFERENCES

1. P. J. E. Peebles, *The Large-Scale Structure of the Universe* (Princeton University Press, Princeton, 1980; Mir, Moscow, 1983).
2. M. A. Strauss and J. A. Willick, Phys. Rev. **261**, 271 (1995).
3. J. A. Willick, S. Courteau, S. M. Faber, *et al.*, Astrophys. J., Suppl. Ser. **109**, 333 (1997).
4. J. A. Willick, S. Courteau, S. M. Faber, *et al.*, Astrophys. J. **457**, 460 (1996).
5. P. Nilson, *Uppsala General Catalogue of Galaxies*, Uppsala Astron. Obs. Ann. **6** (1973).
6. A. Lauberts, *The ESO/Uppsala Survey of the ESO (B) Atlas* (ESO, Munich, 1982).
7. B. A. Vorontsov-Vel'yaminov, A. A. Krasnogorskaya, and V. P. Arkhipova, *Morphological Catalog of Galaxies, Parts I-IV* [in Russian].
8. I. D. Karachentsev, V. E. Karachentseva, and S. L. Parnovsky, Astron. Nachr. **313**, 97 (1995).
9. I. D. Karachentsev, Astron. J. **97**, 1566 (1989).
10. I. D. Karachentsev, V. E. Karachentseva, Yu. N. Kudrya, *et al.*, Astron. Nachr. **316**, 369 (1995).
11. I. D. Karachentsev, V. E. Karachentseva, Yu. N. Kudrya, *et al.*, Pis'ma Astron. Zh. **22**, 330 (1996).
12. I. D. Karachentsev, V. E. Karachentseva, Yu. N. Kudrya, *et al.*, Pis'ma Astron. Zh. **23**, 652 (1997).
13. Yu. N. Kudrya, I. D. Karachentsev, V. E. Karachentseva, *et al.*, Pis'ma Astron. Zh. **23**, 15 (1997).
14. D. I. Makarov, I. D. Karachentsev, A. N. Burenkov, *et al.*, Pis'ma Astron. Zh. **23**, 736 (1997).
15. D. I. Makarov, I. D. Karachentsev, N. V. Tyurina, *et al.*, Pis'ma Astron. Zh. **23**, 445 (1997).
16. D. S. Mathewson and V. L. Ford, Astrophys. J., Suppl. Ser. **107**, 97 (1996).
17. D. S. Mathewson, V. L. Ford, and M. Buchhorn, Astrophys. J., Suppl. Ser. **81**, 413 (1992).
18. R. Giovanelli, E. Avera, and I. D. Karachentsev, Astron. J. **114**, 122 (1997).
19. I. D. Karachentsev, Pis'ma Astron. Zh. **17**, 97 (1991).
20. A. Kogut, C. Lineweaver, G. F. Smoot, *et al.*, Astrophys. J. **419**, 1 (1993).
21. R. Giovanelli, M. P. Haynes, J. J. Salzer, *et al.*, Astron. J. **110**, 1059 (1995).
22. R. B. Tully, M. J. Pierce, J.-S. Huang, *et al.*, astro-ph/9802247 (1998).
23. D. Lynden-Bell, S. M. Faber, D. Burstein, *et al.*, Astrophys. J. **326**, 19 (1988).
24. M. J. Hudson, Mon. Not. R. Astron. Soc. **266**, 475 (1994).
25. T. R. Lauer and M. Postman, Astrophys. J. **425**, 418 (1994).
26. R. Giovanelli, M. P. Haynes, W. Freudling, *et al.*, Astrophys. J. Lett. **505**, L91 (1998).
27. R. Giovanelli, M. P. Haynes, J. J. Salzer, *et al.*, astro-ph/9808158 (1998).
28. M. J. Hudson, R. J. Smith, J. R. Lucey, *et al.*, astro-ph/9901001 (1999).
29. A. Dekel, A. Eldar, T. Kolatt, *et al.*, astro-ph/981297 (1998).
30. R. Scaramella, G. Baiesi-Pillastrini, G. Chincarini, *et al.*, Nature **338**, 562 (1989).
31. I. Schmoldt, E. Branchini, L. Teodoro, *et al.*, astro-ph/9901087 (1999).
32. M. Plionis and V. Kolokotronis, Astrophys. J. **500**, 1 (1998).

Translated by A. Dambis

Rapid Variability of the Radio Flux Density of 0524 + 034

A. G. Gorshkov[1], V. K. Konnikova[1], and M. G. Mingaliev[2]

[1] Sternberg Astronomical Institute,
Universitetskiĭ prospekt 13, Moscow, 119899 Russia
[2] Special Astrophysical Observatory, Russian Academy of Sciences,
Nizhni Arkhyz, 357147 Russia

Abstract—Simultaneous observations on the RATAN-600 radio telescope at 0.97, 2.3, 3.9, 7.7, 11.1, and 21.7 GHz during the period from January 3 to February 25, 1998, revealed variability of 0524 + 034 on time scales not exceeding 10 days. The variations are correlated at all frequencies where the parameters of the variability could be determined, including in the optically thick part of the spectrum. The mean spectrum of the variable component was derived and is in agreement with the spectrum of a homogeneous, spherically symmetrical source. In the optically thin part of the spectrum, the spectral index of the variable component is $\alpha = -0.2$, reflecting the initial energy distribution of the relativistic electrons. It is argued that the variable emission is associated with the acceleration of electrons and amplification of the magnetic field and that adiabatic expansion can be neglected. It is proposed that the observed variability is due to illumination of inhomogeneities in the jet by a shock front passing through them and that the light curve reflects the distribution and characteristic sizes of these inhomogeneities (0.14–0.5 pc for angles to the line of sight not exceeding 10°, Lorentz factor $\gamma = 10$, and adopted redshift $z = 0.5$). In 0524 + 034, in addition to the rapidly variable component, there are two slowly varying components, one of which has $\alpha = -0.7$ in the optically thin part of the spectrum. © 2000 MAIK "Nauka/Interperiodica".

1. INTRODUCTION

In [1], we reported the unusually large amplitude of the long-term flux variability of the radio source 0524 + 034 at centimeter and decimeter waves. This source was detected for the first time in 1979 in the Zelenchuk Survey, carried out on the RATAN-600 radio telescope at 8.7 GHz [2]; its flux at that time was 460 mJy. The radio source is identified with a 19th-magnitude object on the Palomar Survey O map; its 2000.0 coordinates are [3]

$$RA = 05^h27^m32^s.70, \quad DEC = 03°31'31''.44.$$

In 1996–1998, the flux density continued to increase. Over the last ten years of observations, its flux at 7.7 GHz has increased by more than a factor of 20. Here, we report the detection of flux variability on time scales shorter than 10 days at frequencies 2.3–21.7 GHz.

At centimeter wavelengths, the variability of BL Lac objects on time scales from weeks to months has been known for a long time and has been intensely studied (see, for example, [4, 5]). Variability has also been found on shorter time scales, from several hours [6] at 1.42 GHz to about one day over a wide frequency range [7]. These variations could arise within the source itself or could result from propagation of the radiation through a nonuniform medium.

If the variability is intrinsic to the source, then such short time scales for the variability result in brightness temperatures considerably exceeding the Compton limit of 10^{12} K. Therefore, the rapid variability cannot

be explained within the framework of the standard model of a spherically symmetric, homogeneous, adiabatically expanding cloud of relativistic electrons [8, 9]. Brightness temperatures exceeding the Compton limit can be explained using models with relativistic motion of the emitting plasma under a small angle to the observer's line of sight.

The behavior of variable radio sources on various time scales and over a wide frequency range can best be explained in the framework of models with shock waves propagating in relativistic plasma [10]. Our studies support such a mechanism for the variability.

2. OBSERVATIONS

Observations were carried out daily from January 3 to February 25, 1998, as part of a program to study rapid variability of sources from a complete flux-limited sample. The sample contains all sources with fluxes $S_{3.9 \, GHz} > 200$ mJy near 24 h in right ascension and in the declination zone 3°30'–6°.

We included 73 sources in the observational program, among them 39 objects with flat and 34 objects with power-law spectra. We used sources with power-law spectra, which have constant fluxes, as a control group in statistical studies of the parameters of small-amplitude variability, and also for studies of instrumental effects that could result in additional errors in the flux-density determinations. The observations were carried out on the meridian on the Northern sector of
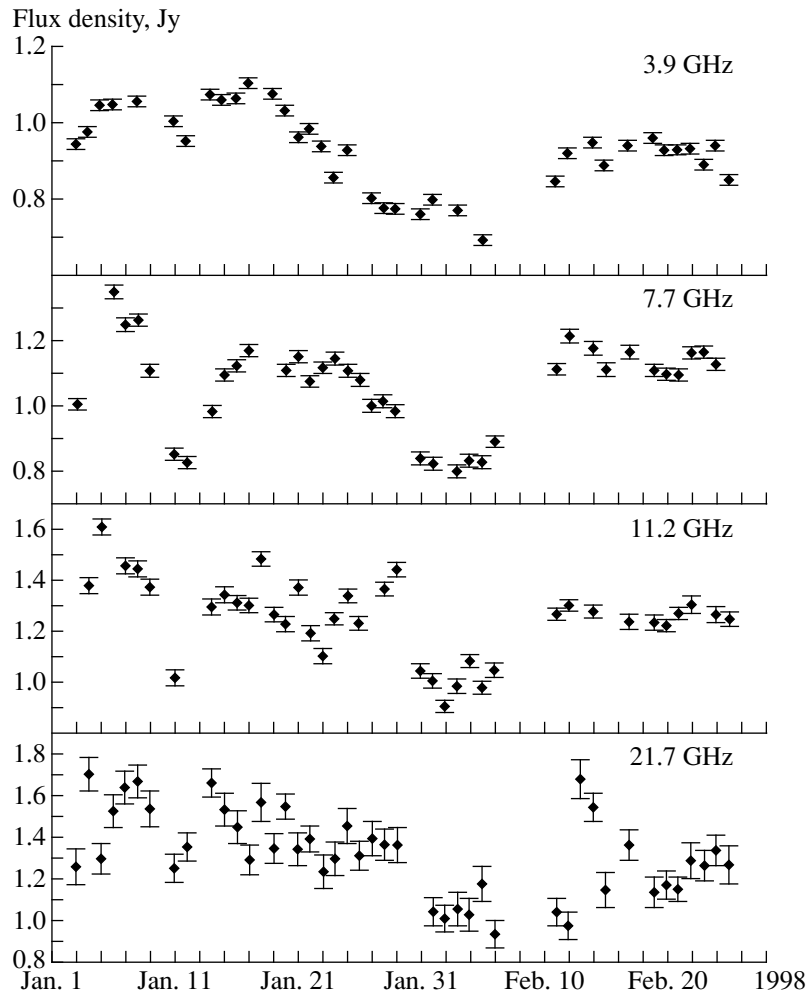
Fig. 1. Flux densities of the source 0524 + 034 at 3.9, 7.7. 11.1, and 21.7 GHz from January 3 to February 25, 1998.

RATAN-600 in the fixed-focus regime [11], simultaneously at 0.97, 2.3, 3.9, 7.7, 11.1, and 21.7 GHz, using the standard receivers for feed no. 1. Use of the fixed-focus regime enabled us to eliminate flux errors due to displacements of the feed (secondary mirror). The parameters of the receivers and antenna beam at all frequencies are given in [12]. Using beam switching for the short-wavelength receivers at 7.7, 11.1, and 21.7 GHz enabled us to considerably reduce drifts due to atmospheric irregularities.

We matched the flux density scale to the scale for the reference sources with power-law spectra published in [13]. The data processing procedure and error estimates are described in [14].

3. RESULTS

The radio source 0524 + 034 is the only object in the sample in which we found such a large variability amplitude during the observing period. Figure 1 presents the flux densities of 0524 + 034 at 2.3, 3.9, 7.7,

11.1, and 21.7 GHz obtained during the observing session. No observations were carried out on January 10, 13, and 30 and February, 7–10, 16, and 18 due to poor weather conditions.

Considerable variability at 3.9, 7.7 and 11.1 GHz is clearly visible in the figure. This is a real effect, not an artifact, since no similar brightness curves are observed for any source from the control group. The variability index $V = \Delta S/\langle S \rangle$ was defined in [15] and represents the mean relative variability amplitude for the observing period. These indices were 0.20, 0.57, 0.76, 0.63, and 0.54 at 2.3, 3.9, 7.7, 11.1, and 21.7 GHz, respectively.

The spectrum of the source (Fig. 2) based on the mean fluxes grows toward higher frequencies. There is a minor local minimum near 7.7 GHz, testifying to the presence of at least two compact components at different stages of development in the radio source.

We studied the parameters of the variability using various methods. It proved most informative to construct the first- and second-order structure functions.

3.1. Properties of the Structure Functions

The definition of the structure functions and their basic properties are given in [16, 17]. For a measurement time series $f(t)$, the first-order and second-order structure functions $D^1(\tau)$ and $D^2(\tau)$ are defined

$$D^1(\tau) = \langle [f(t) - f(t+\tau)]^2 \rangle, \qquad (1)$$

$$D^2(\tau) = \langle [f(t+2\tau) - 2f(t+\tau) + f(t)]^2 \rangle, \qquad (2)$$

where τ is the time shift. The mth-order structure function is equal to zero for polynomials of order $m - 1$; therefore, the form of the structure function will depend only on the character of random processes and on higher order trends.

The "ideal" structure function for a random process has a characteristic appearance: two plateaus connected by a curve. For time delays larger than the longest correlation timescale for the process, the plateau amplitude $D^1(\tau)$ is equal to twice the sum of the dispersions of the instrumental noise and the process studied. For small time delays, the plateau amplitude $D^1(\tau)$ is equal to twice the dispersion of the instrumental noise. For the structure functions $D^2(\tau)$, the plateau amplitudes are equal to six times the corresponding dispersions. These plateaus are connected by a curve, whose slope depends on the nature of the process in action.

The structure function is usually represented on a logarithmic scale, so that the slope of the line connecting the two plateaus $\mu = d\log D / d\log\tau$ is determined by the power spectrum of the process $P(f)$. If $P(f) \propto f^{-1}$ (flicker noise), $D^1(\tau) \propto \tau^0$; if $P(f) \propto f^{-2}$ (shot noise), $D^1(\tau) \propto \tau^1$. In most cases, the structure function has a more complicated form, but these simple cases can be useful for analyses of radio-source variability. The presence of harmonic (or cyclic) components in the process studied decreases the magnitude of the structure function at delays comparable to the period of these components.

We constructed the structure functions $D^1(\tau)$ (Fig. 3) and $D^2(\tau)$ (Fig. 4) for all the observing frequencies. We normalized the functions to the process dispersion, which was defined

$$\sigma_{pr}^2 = \sum (f_i - \langle f \rangle)^2 / (n-1), \qquad (3)$$

where f_i is the flux measured on the ith day and $\langle f \rangle$ is the weighted-mean flux for n days of observations. This dispersion is the sum of the variable-component dispersion σ_{var}^2 and the mean dispersion for a single measurement σ_m^2. Note that the measurement dispersion includes all sources of measurement error: instrumental noise, instability of the calibration signal, inaccuracy of the antenna pointing, etc. With this normalization, the upper plateau of the "ideal" structure function asymptotically approaches the values $\log 2$ and $\log 6$ for the
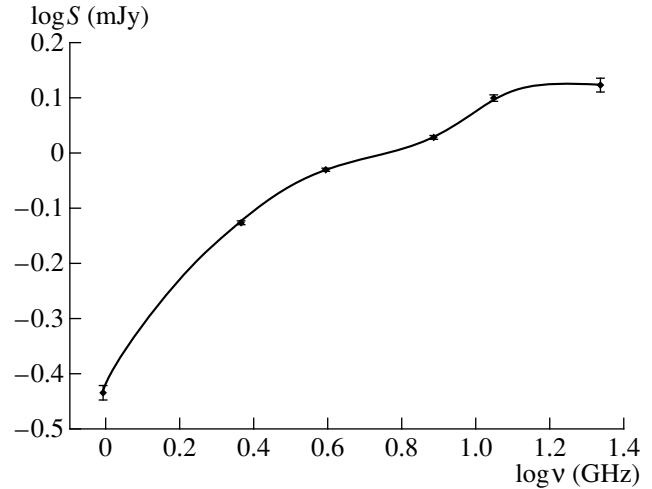

Fig. 2. The spectrum of 0524 + 034 based on the averaged data for the period from January 3 to February 25, 1998.

first- and second-order structure functions, respectively (thin horizontal lines in Figs. 3 and 4).

Both the first- and second-order structure functions for 0524 + 034 display a second plateau at 3.9, 7.7, 11.1, and 21.7 GHz. At 2.3 GHz, there are only hints of a second plateau, due to large instrumental errors and small amplitude of the variability; it is obvious that there is only instrumental noise at 0.97 GHz.

The first-order structure functions. The second plateau reaches a value of $\log 2$ for delays of 6–8 days at all frequencies. The second plateau is most obvious at 3.9 and 7.7 GHz, due to the lower instrumental noise. At 3.9 GHz, we can see a decrease of the plateau magnitude at delays longer than 20 days, with the minimum achieved at delays of about 40 days. This behavior, in combination with the fact that the plateau maximum exceeds $\log 2$, is typical of the presence of a harmonic (or cyclic) component. At the remaining frequencies, there are only hints of such a decrease.

One characteristic feature of the structure functions is the absence of a pronounced plateau due to instrumental noise at frequencies below 21.7 GHz. This testifies to the small width of the correlation function of the variable component; its magnitude changes appreciably when the delay varies from 1 to 2 days. The plateau at 21.7 GHz is most likely connected to the poorer sensitivity of the equipment at this frequency.

The slopes μ of the structure functions at 11.1, 7.7, and 3.9 GHz are close to unity. In Fig. 3, a slope corresponding to $\mu = 1$ is indicated by an arrow.

The second-order structure functions. The behavior of the second-order structure functions is similar to that of the first-order structure functions at the corresponding frequencies. The main difference from $D^1(\tau)$ is the appearance of a clearly visible first plateau at 7.7 and 3.9 GHz; the extent of the plateau varies from two days at 7.7 GHz to three days at 3.9 GHz. The decrease
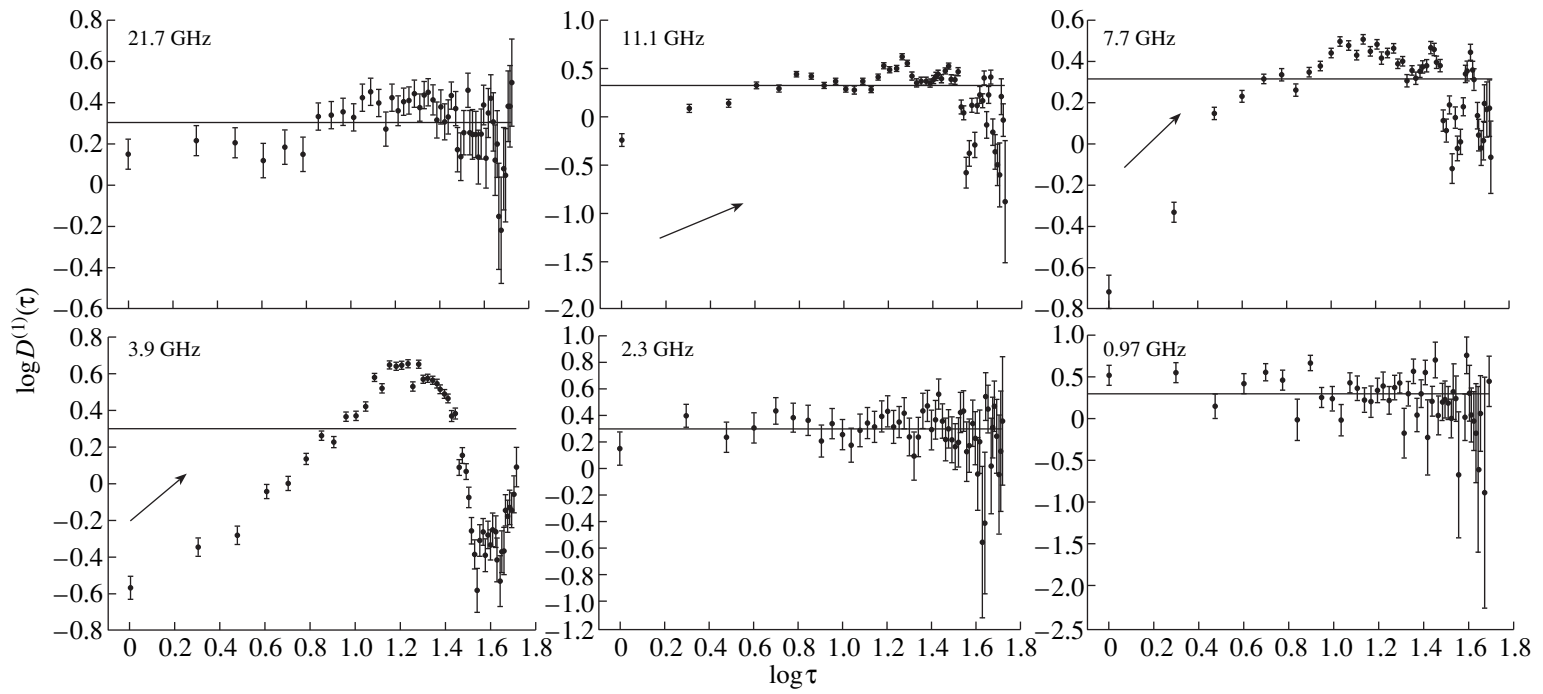
Fig. 3. The first-order structure functions $D^1(\tau)$ normalized to the dispersion on a logarithmic scale for the period from January 3 to February 25, 1998, at 0.97, 2.3, 3.9, 7.7. 11.1, and 21.7 GHz. The dashed line designates a value of $\log 2$. The arrow shows a slope corresponding to $\mu = 1$.
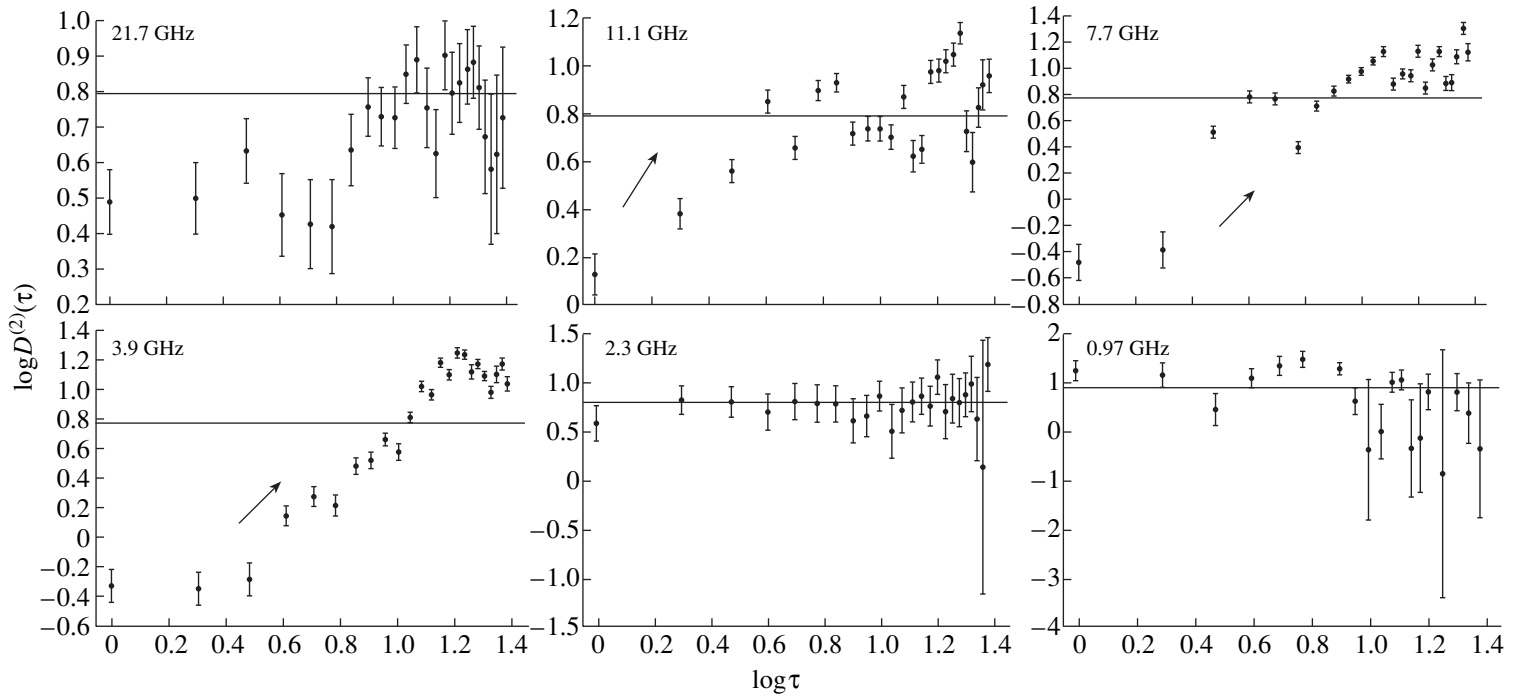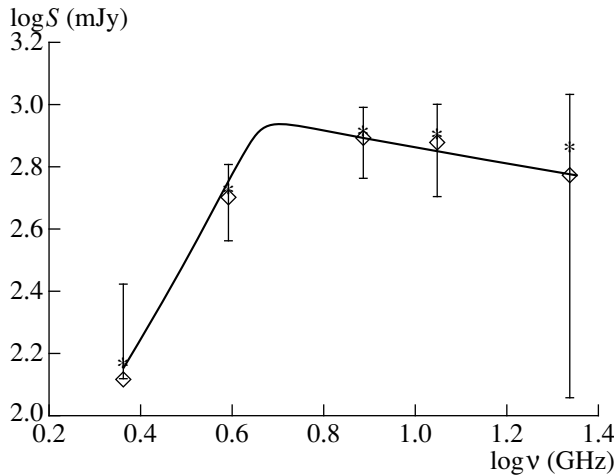
Fig. 4. The second-order structure functions $D^2(\tau)$ normalized to the dispersion on a logarithmic scale for the period from January 3 to February 25, 1998, at 0.97, 2.3, 3.9, 7.7. 11.1, and 21.7 GHz. The dashed line designates a value of $\log 6$. The arrow shows a slope corresponding to $\mu = 2$.

logS (mJy)

Fig. 5. The mean spectrum of the variable component of 0524 + 034 over the observation period. The diamonds show the spectrum of the flux variations, defined as $S_{var} = 6\sigma_{var}$ (the error is given for this definition of the spectrum). The asterisks show the spectrum calculated using formula (4). The solid curve corresponds to an optically thick spectral index $\alpha = 2.5$ and an optically thin spectral index $\alpha = -0.2$.

of the amplitude of the second plateau is not visible due to the halving of the maximum delay time. The slope of the structure functions is close to $\mu = 2$. For $D^2(\tau)$, this value of μ describes shot noise; in Fig. 4, this slope is also shown with an arrow.

3.2. The Frequency Spectrum of the Variations

The mean frequency spectrum of the variations for the observing period can be derived in several ways.

(1) The lower plateau of the first-order structure function (without any normalization) is twice the measurement dispersion, $2\sigma_m^2$. Hence, $\sigma_{var}^2 = \sigma_{pr}^2 - \sigma_m^2$ is the dispersion of the variable component of the radio emission. We took $D^1(1)/2$ for the value of σ_m^2, and σ_{pr}^2 was calculated using formula (3). As noted above, the lower plateau is poorly defined in the $D^1(\tau)$ structure functions; therefore, σ_m^2 is an upper estimate of the measurement dispersion. The frequency spectrum of the flux variations, defined to be $S_{var} = 6\sigma_{var}$, is shown in Fig. 5 by the diamonds.

(2) We use the formula for the variability amplitude given in [15]:

$$S_{var} = \{(n-1)[Y - (n-1)]/\sum \sigma_i^{-2}\},$$
$$Y = \sum (S_i - \langle S \rangle)^2/\sigma_i^2. \tag{4}$$

In this case, the dispersion of a single measurement is taken to be $\sigma_i^2 = \sigma_{iform}^2 \sigma_m^2/\sigma_{form}^2$, where σ_{iform}^2 is the formal dispersion of a single measurement and σ_{form}^2 is

the mean measurement dispersion, taking into account only the instrument noise and the instability of the calibration signal. The introduction of σ_i^2 allows us to take into account the remaining errors. The resulting spectrum, which virtually coincides with the spectrum obtained using the first method, is presented in Fig. 5 by the asterisks.

The spectrum has the canonical form for a homogeneous, spherically symmetric radio source with synchrotron self absorption. The slope α ($S \propto \nu^\alpha$) in the optically thick and optically thin parts of the spectrum are 2.5 and –0.2, and the flux peaks at 5–6 GHz. In Fig. 5, a spectrum with the indicated parameters is approximated with a continuous curve. Precisely the same parameters for the mean spectrum of a flare were obtained in [18] based on the selection and analysis of 17 isolated flares at an early stage of evolution in 15 variable sources.

Usually, when determining the spectrum of a flare, the flux of the constant component is subtracted from the observed flux. This constant flux is typically taken to equal the minimum flux near the selected flare. The methods we propose for determining the flare spectrum do not involve any assumptions about the flux of the steady or slowly varying component. The derived spectrum of the variations is the mean spectrum for the 50 days of observations; the character of the structure functions testifies to the presence during this period of a process with a timescale of 6–8 days, rather than an isolated flare. In the case of an isolated flare, the slope of the structure function $D^1(\tau)$ should be considerably greater than unity. The reasons why the mean spectrum of the variations coincides with that of an isolated flare will be analyzed below.

3.3. Correlation Functions

The autocorrelation functions at 21.7 and 2.3 GHz have no significant values for any time shifts, due to the large amplitudes of the instrumental noise at 21.7 GHz and the small amplitudes of the variations at 2.3 GHz. The autocorrelation functions at 11.1 GHz (Fig. 6a) and 7.7 GHz (Fig. 6b) display a rapid drop in their amplitudes, as expected from our analysis of the structure functions. The magnitudes of the correlation functions become insignificant for time delays exceeding three days (we chose the significance level to be 2%).

The correlation function at 3.9 GHz (Fig. 6c) is an exception: Significant values persist for time delays as long as six days, and a significant anticorrelation is observed for delays of 16–22 days. The autocorrelation function at this frequency is very smooth. This behavior of the autocorrelation function, as well as that of the structure function, testify to the presence of a periodic component with a period of 35–40 days. The autocorrelation function is broader, due to the appearance of the lower plateau in the second-order structure function at this frequency.
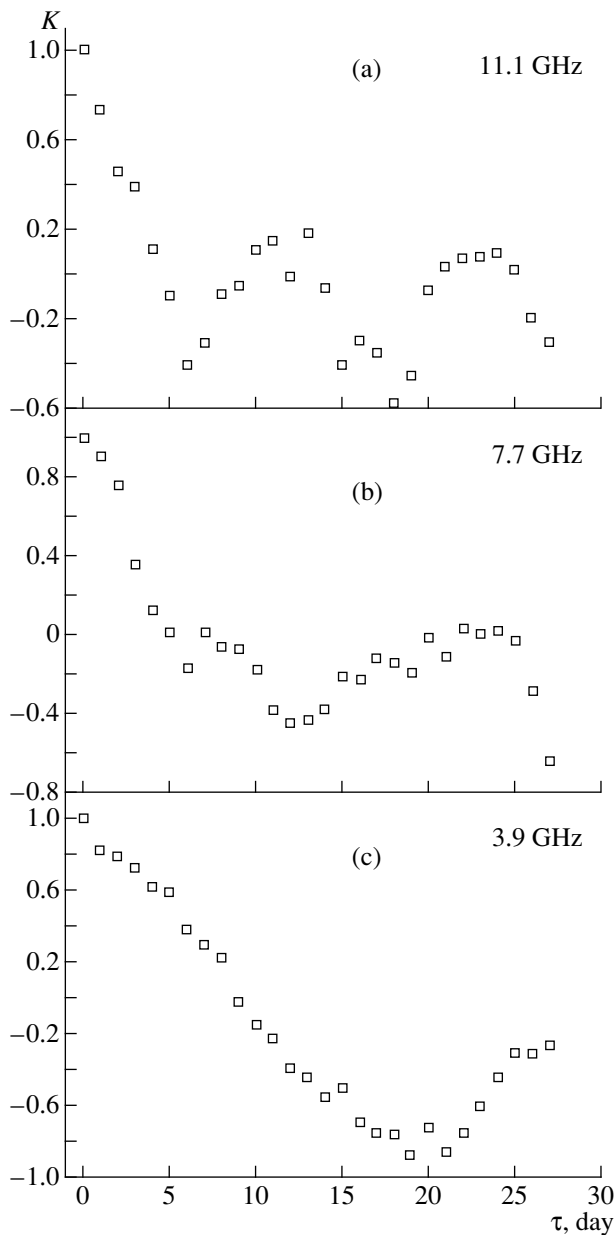
Fig. 6. Autocorrelation functions of the fluxes of 0524 + 034 at (a) 11.1, (b) 7.7, and (c) 3.9 GHz.

Fig. 7. Cross-correlation functions of the fluxes of 0524 + 034 between 11.1 and 7.7 GHz (squares) and between 7.7 and 3.9 GHz (crosses). For comparison, the autocorrelation function at 7.7 GHz (triangles) is presented.

We have constructed the cross-correlation functions for the data at 11.1–7.7 GHz and 7.7–3.9 GHz (Fig. 7). Their behavior is very similar to that of the autocorrelation functions at these frequencies. The effect of a periodic component is visible in the 7.7–3.9-GHz cross-correlation function, though it is much less pronounced than in the 3.9-GHz autocorrelation function.

Analysis of the auto- and cross-correlation functions suggests that a uniform process is responsible for flux density variations observed in the radio source 0524 + 034 at centimeter wavelengths. The small amplitude of the variations at 2.3 GHz prevents us from drawing
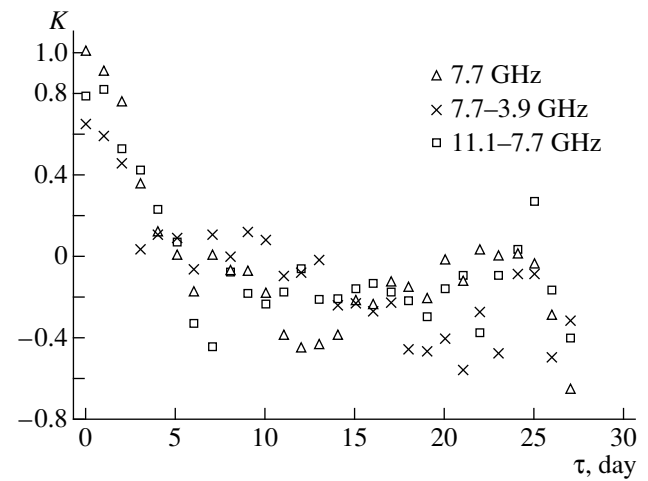
any conclusions about the character of the variability at this frequency.

It appears that the timescale for the variations at 3.9 GHz is longer than at higher frequencies. This is no surprise, since the variations at this frequency are already observed in the optically thick part of the spectrum.

There is some inconsistency between the short time scales of the variations and the presence of a periodic component in the 3.9-GHz variations. It is possible that two processes coexist simultaneously—one with short time scales and the other with longer ones. In this picture, the development of one process is followed over the observation period. In this case, such a process could resemble a periodic process.

4. DISCUSSION

Our analysis of the cross-correlation functions indicates that the variations at 11.1, 7.7, and 3.9 GHz occur simultaneously, though the lowest frequency is already in the optically thick part of the spectrum. There is every reason to believe that the variations at 21.7 GHz are also simultaneous with those at the remaining frequencies.

The simultaneity of the variations over a broad frequency range suggest that electron acceleration and amplification of the magnetic field are important, whereas adiabatic expansion is insignificant [19]. Therefore, if the ejection of material is nonuniform along the direction of propagation of a shock, the resulting inhomogeneous structures will be illuminated when the shock passes through them, so that the light curve will reflect the distribution and characteristic sizes of the inhomogeneities. It is noted in [7] that, in shock models, the effects of expansion can be neglected
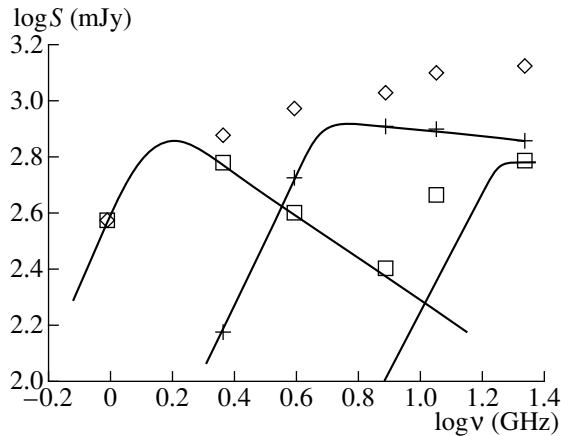
Fig. 8. Separation of the observed spectrum of 0524 + 034 into components. The diamonds show the observed spectrum. The crosses show the spectrum of the variable component; the solid curve passing through the crosses corresponds to an optically thick spectral index $\alpha = 2.5$ and an optically thin spectral index $\alpha = -0.2$. The squares show the spectrum of the slowly varying component separated into two components (solid lines); the optically thin spectral index α is –0.7.

if the jet opening angle is very small, and the sizes of the structural inhomogeneities are smaller than 1 pc. A formula relating the variation timescale to the distance covered by the shock in the jet over this time is given in [7]. For 0524 + 034, with a variation timescale of 6 days and a Lorentz factor $\gamma = 10$, this distance (the size of an inhomogeneity) is 0.14–0.5 pc for angles to the line of sight of 10° to ~0° and an adopted redshift $z = 0.5$.

In the optically thick part of the spectrum (in our case, below 5–6 GHz), the variations can be extended in time, and individual features may not coincide with those in the optically thin part of the spectrum. Precisely such a flattening could give rise to the appearance of the periodic component at 3.9 GHz, which may reflect the existence of larger inhomogeneities corresponding to variations with time scales of about 20 days.

In this case, the fact that the shape of the mean spectrum of the variations coincides with that of a spherically symmetric, homogeneous synchrotron source implies similarity of the physical conditions (electron density, electron energy distribution, and magnetic field intensity) for various inhomogeneities traversed by the shock during the observations.

Similar conclusions were drawn in [7] based on simultaneous observations of the quasar 0917 + 624 at five wavelengths spanning 2–20 cm. The timescale for the variations in 0917 + 624 is 1.3 days. The spectrum of the variations also coincides with that of a homogeneous synchrotron source, but the flux peaks at about 3 GHz and the spectral index α in the optically thin domain is –0.7. The size of the inhomogeneities is 0.16 pc for a Lorentz factor $\gamma = 14$ and angle θ close to zero. As for 0524 + 034, the spectrum of the variable compo-

nent remains virtually constant on time scales comparable to the variability timescale.

The difference in the optically-thin spectral indices of these two sources can be explained as follows. In a number of cases of long-timescale variability, the optically-thin spectrum of the variable component evolves from being flat ($\alpha = -0.2$) at an early stage to being power-law ($\alpha = -0.7$) at later stages [18]. This could be the effect of considerable radiative losses in late stages of the jet evolution. The value $\alpha = -0.2$ is typical for VLBI core components of radio sources, which are probably located close to the central engine. For noncore components, which are much more distant from the nucleus, the spectral index increases to $\alpha = -0.7$ [20].

We believe that the optically thin spectral indices of 0524 + 034 and 0917 + 624 are different because the variability is observed in components with different ages. In the former case, the variability is due to a shock propagating in a region that is close to the nucleus, and an initial electron spectrum with $\gamma = 1.4$ is observed. In the latter case, the shock is propagating in a component that is far from the nucleus, and the energetic electrons have already had time to lose some of their energy ($\gamma = 2.4$).

This interpretation is supported by the separation of the observed spectrum of 0524 + 034 into components. Since we have determined the frequency spectrum of the variations, we can remove it from the observed spectrum, yielding the spectrum of the constant or (more correctly) slowly varying component. The results of our separation of the spectrum into components are presented in Fig. 8; the diamonds denote the initial spectrum, crosses the spectrum of the variations, and squares the residual spectrum, which, in turn, consists of two components. Both components have spectra close to that of a spherically symmetric, homogeneous source; the low-frequency component has a maximum at about 1.5 GHz and an optically thin spectral index of about –0.7. Note that, according to [1], the integrated flux of the source in July 1988 did not exceed 80 mJy at 3.9 GHz. In the frequency range considered, only the optically thick part of the spectrum of the high-frequency component is observed; judging from its behavior, we expect that the maximum in the spectrum lies somewhere in the range 30–50 GHz.

We believe that the low-frequency component is a jet located at a considerable distance from the nucleus, which has already had time to evolve. Its spectral characteristics are similar to those of 0917 + 624, but it does not display any rapid variability.

5. CONCLUSION

We have observed rapid variability in the source 0524 + 034 with a timescale of about six days. The variations bear the character of shot noise and result from damping pulses of white noise with a limited spectrum.

The variations are correlated at all frequencies where the parameters of the variability could be determined, including in the optically thick part of the spectrum. In this part of the spectrum, we observe an increase of the correlation timescale.

We suggest that the variability is due to the illumination of inhomogeneities in the jet by a shock front passing through them and that the light curve reflects the distribution and characteristic sizes of these inhomogeneities (0.14–0.5 pc for angles to the line of sight not exceeding $10°$, a Lorentz factor $\gamma = 10$, and adopted redshift $z = 0.5$).

The simultaneity of the variations over a broad frequency range and the fact that the mean spectrum of the variable component coincides with the spectrum of a homogeneous, spherically symmetric source suggest the importance of acceleration of electrons and amplification of the magnetic field, whereas adiabatic expansion can be neglected.

In the variable component, we infer an initial electron spectrum with $\gamma = 1.4$. Therefore, this component should be located in the immediate vicinity of the "central engine."

In addition to the variable component, 0524 + 034 has two stationary or slowly varying components, one of which has $\gamma = 2.4$ in the optically thin part of the spectrum.

ACKNOWLEDGMENTS

REFERENCES

1. A. G. Gorshkov and V. K. Konnikova, Astron. Zh. **74**, 374 (1997).
2. V. R. Amirkhanyan, A. G. Gorshkov, and A. A. Kapustkin, Astron. Zh. **58**, 717 (1981).
3. R. Perley, private communication (1997).
4. D. R. Altschuler, Astron. J. **85**, 1559 (1980).
5. H. D. Aller, M. F. Aller, and P. E. Hodge, Astron. J. **86**, 325 (1981).
6. G. T. Romero, G. Surpi, and H. Vicetich, Astron. Astrophys. **301**, 64 (1995).
7. S. J. Qian, A. Quirrenbach, A. Witzel, *et al.*, Astron. Astrophys. **241**, 15 (1991).
8. I. S. Shklovskiǐ, Astron. Zh. **37**, 256 (1960).
9. H. Van der Laan, Nature **211**, 1131 (1966).
10. A. P. Marscher and W. K. Gear, Astrophys. J. **298**, 114 (1985).
11. N. S. Soboleva, A. V. Temirova, and T. B. Pyatunina, Preprint No. 32L (Special Astrophysical Observatory, 1986).
12. A. B. Berlin, A. A. Maksyasheva, N. A. Nizhel'skiǐ, *et al.*, *Abstracts of the XXVII Radio Astronomy Conference* [in Russian] (St. Petersburg, 1997), Vol. 3, p. 115.
13. A.M. Botashev, A. G. Gorshkov, V. K. Konnikova, and M. G. Mingaliev, Astron. Zh. **76**, 723 (1999).
14. A. G. Gorshkov and O. I. Khromov, Izv. SAO **14**, 15 (1981).
15. G. A. Seielstad, T. J. Pearson, and A. C. S. Readhead, Publ. Astron. Soc. Pacif. **95**, 842 (1983).
16. J. H. Simmonetti, J. M. Cordes, and D. S. Heeschen, Astrophys. J. **296**, 46 (1985).
17. P. A. Hughes, H. D. Aller, and V. F. Aller, Astrophys. J. **396**, 469 (1992).
18. E. Valtaoja, S. Haarala, H. Lehto, *et al.*, Astron. Astrophys. **203**, 1 (1988).
19. A. G. Pacholczyk and J. S. Scott, Astrophys. J. **210**, 311 (1976).
20. M. V. Popov and Yu. Yu. Kovalev, Astron. Zh. **76**, 643 (1999).

Translated by G. Rudnitskiǐ

Synthesis of Radioactive Isotopes and Gamma Radiation in Nova Outbursts

A. D. Kudryashov[1], N. N. Chugaĭ[2], and A. V. Tutukov[2]

[1]*All-Russia Institute for Science and Technical Information (VINITI),*
ul. Usievicha 20a, Moscow, Russia

[2]*Institute of Astronomy, Russian Academy of Sciences,*
ul. Pyatnitskaya 48, Moscow, 109017 Russia

Received March 1, 1999

Abstract—The range of abundances of radioactive nuclei in material ejected during novae is derived from kinetic calculations of thermonuclear burning in a hydrogen-rich, single-zone envelope at the surface of a CO or ONeMg dwarf. The total amount of radioactive N, O, and F isotopes in the envelope is approximately equal to the mass of CO in the dwarf that is admixed during accretion and/or the outburst. The mass fraction of synthesized ^{18}F is 10^{-3}–10^{-2}. In the case of ONeMg dwarfs, the abundances of ^{22}Na and ^{26}Al are substantially higher and reach several percent and one percent of the mass, respectively. We derived light curves in the annihilation line from short-lived NOF-isotopes and studied the effect of varying the envelope parameters. The light curves are most sensitive to the degree of mixing of the radioactive isotopes in the envelope. Even having as little as 1% of unmixed material in the outer layer results in appreciable suppression of the first luminosity peak due to radioactive NO isotopes. The second luminosity peak, due to ^{18}F decay, is appreciably suppressed only when the relative mass of unmixed material in the outer layer exceeds 10%. We suggest observations of the ^{18}F annihilation-line flux with independent observational estimates of the ^{18}F mass in the ejected envelope as a means to determine the degree of mixing and the mass of synthesized ^{18}O. Calculations of the synthesis of ^{22}Na and ^{26}Al isotopes are compared to estimates of the masses of these isotopes in the envelopes of novae derived from observations of their gamma radiation. © *2000 MAIK "Nauka/Interperiodica"*.

1. INTRODUCTION

Thermonuclear burning of hydrogen at the surface of a white dwarf during a nova outburst results in the synthesis of radioactive NOF isotopes ^{13}N, ^{14}O, ^{15}O, ^{17}F, ^{18}F, which have lifetimes shorter than three hours (see Table 1), and also of ^{22}Na, with a lifetime of 3.75 yrs, and ^{26}Al, with a lifetime of 1.04×10^6 yrs [1–12]. Gamma radiation at 1.275 MeV (^{22}Na) and 1.809 MeV (^{26}Al) freely leaves the envelope after it becomes transparent, several days after the outburst. Attempts have been made to detect the ^{22}Na gamma line from novae [13], both for individual outbursts [14] and in the diffuse radiation from the region of the Galactic center [15]. The possible contribution of novae to the observed Galactic ^{26}Al gamma radiation [16] is discussed in [17–22].

Like ^{22}Na and ^{26}Al, the gamma radiation from short-lived NOF isotopes (primarily annihilation gamma radiation and the ^{14}O 2.312-MeV line) is essentially completely absorbed in the nova envelope, since the lifetime of these isotopes is appreciably shorter than the characteristic time scale for the envelope to become transparent. Nonetheless, it is still possible to observe gamma radiation from NOF isotopes. If there is efficient mixing in the envelope during the outburst, some fraction of the isotopes can end up in the outer layers of the expanding envelope, and gamma radiation from the

layer with optical depth equal to unity freely leaves the envelope [13]. Observations of the annihilation line at early stages of novae could provide important information about thermonuclear burning and mixing, as well as the structure of the nova envelope.

Calculations of the gamma radiation during a nova outburst when the envelope is still opaque, based on the first simple estimates made in [13], are given in [23, 24]. Note, however, that modern theories are unable to provide reliable predictions for gamma radiation and, in particular, for the luminosity of novae in the annihilation line from NOF isotopes, since descriptions of core–envelope mixing and of mixing in the envelope itself are not yet sufficiently accurate. In addition, difficulties are encountered in modeling the dynamics and structure of the ejected envelope.

Taking these circumstances into consideration, we aim to answer the following questions: To what extent do uncertainties in modeling affect the calculated luminosity of the nova in the annihilation line? To what extent is the possible interval of predicted fluxes consistent with available observations? We use here a single-zone model for nucleosynthesis occurring during a thermonuclear outburst on the surface of a white dwarf, which makes it possible to vary the burning parameters over a broad range. The resulting abundances of radio-

active isotopes are used to synthesize light curves in the annihilation line. We considered several models for the ejected envelope, with different kinematics, density distributions, and degrees of isotope mixing in the envelope. We will also examine the observational consequences implied by our calculations of the nucleosynthesis of the long-lived isotopes ^{22}Na and ^{26}Al.

2. THE MODEL AND RESULTS OF THE NUCLEOSYNTHESIS CALCULATIONS

To calculate nucleosynthesis in thermonuclear outburst, we used an updated version of the kinetic scheme from [25, 26]. In addition to hydrogen and helium, it includes nuclei from carbon to calcium and takes into account all nuclear reactions with charged particles. We use a single-zone isothermal approximation, in which the entire envelope is modeled as a uniform spherical layer [25]. The temperature and density were chosen to be within the well established ranges of values for the base of a nova envelope [1–3] and are assumed to be constant in the course of the burning, up to the point when a specified amount of hydrogen is exhausted ($\Delta X = 0.01$ and 0.1). Depending on the adopted value for the burning temperature, this process lasts $10–10^3$ s.

The burning temperature was varied in the interval $(1–3) \times 10^8$ K; the density was taken to be 10^4 g/cm^{-3} in all cases. We assumed the accreted matter to have solar composition. The CO dwarf's composition was [25] $X(^{12}C) = 0.49$, $X(^{16}O) = 0.49$, $X(^{22}Ne) = 0.01$, $X(^{25}Mg) = 0.01$; the ONeMg dwarf's composition was [27] $X(^{16}O) = 0.3$, $X(^{20}Ne) = 0.5$, $X(^{24}Mg) = 0.2$. The chemical composition of the hydrogen envelope at the beginning of the outburst is determined by the mixing parameter q, which is the ratio of the mass of admixed dwarf material and the total mass of the envelope; this parameter varies from 0.1–0.9.

Figures 1 and 2 present the results of our calculations for the most abundant radioactive isotopes as a function of the burning temperature $T_8 = T/10^8$ K for the CO and ONeMg dwarfs, respectively, and for mixing parameter $q = 0.5$. In the case of the CO dwarf, at the burning stage $\Delta X = 0.01$ (Fig. 1), the most abundant isotope for any temperature is ^{13}N, and the mass abundance is 11–12% and is virtually independent of the temperature. This isotope is followed by ^{14}O, ^{17}F and ^{15}O, whose fraction is comparatively small, and does not exceed 1% in total. At this burning stage, the ^{18}F abundance is very low, even taking into account the transformation of ^{18}Ne into ^{18}F. In the case of the ONeMg dwarf (Fig. 2), the most abundant isotope at essentially any temperature is ^{17}F, whose abundance for $T_8 \geq 0.15$ is 6–7%. The ^{13}N abundance for the same temperature does not exceed 10^{-4}, due to the fact that ^{17}F is produced by proton capture by ^{16}O, while ^{13}N is produced from ^{12}C. The fractions of ^{14}O and ^{15}O do not exceed 0.5% in total; the ^{18}F fraction for $T_8 = 1.0$ reaches 0.01, while at higher temperatures, it is near 10^{-3}, taking into account the transformation of ^{18}Ne.
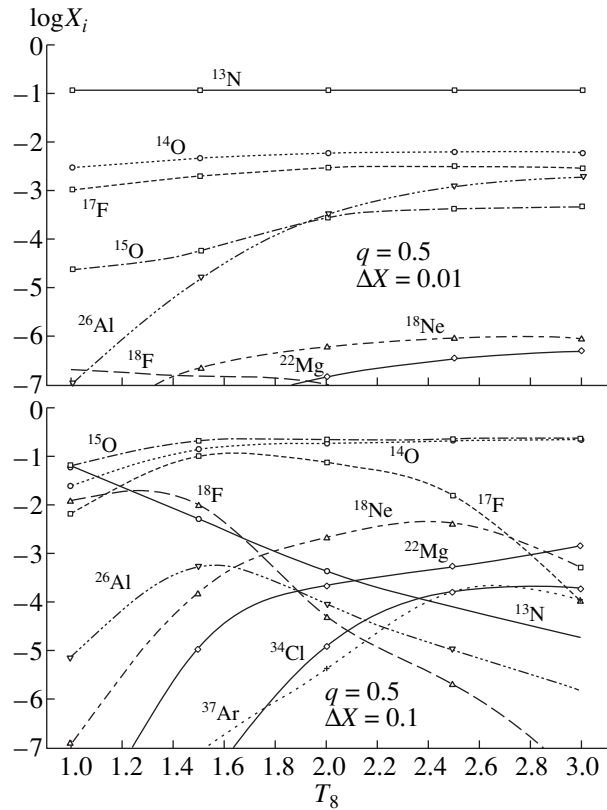

Fig. 1. Abundance of radioactive isotopes in the envelope as a function of burning temperature for a CO dwarf. The fraction of dwarf material in the total mass of the envelope before outburst is 0.5. The initial abundance of hydrogen is decreased by $\Delta X = 0.01$ (above) and by $\Delta X = 0.1$ (below).

For $\Delta X = 0.1$, the most abundant isotopes in the CO dwarf are ^{14}O and ^{15}O, whose combined abundance increases with temperature from 0.1 for $T_8 = 1.0$ to more than 0.5 for $T_8 = 3.0$. The ^{17}F mass abundance for the average temperature is several percent. The ^{18}F abundance for $T_8 \leq 0.15$ exceeds 1% and, at higher temperatures, its mass fraction is several tenths of a percent, taking into account the transformation of ^{18}Ne. The ^{13}N mass abundance is appreciable only for low temperatures (7% for $T_8 = 1.0$). The behavior of the most abundant isotopes in the ONeMg dwarf at the burning stage $\Delta X = 0.1$ is already quite similar to that for the CO dwarf. The most abundant isotopes are ^{15}O, ^{14}O and ^{17}F. ^{18}F has an appreciable abundance (around 1%) for both low and high temperatures, taking into account the contribution from ^{18}Ne. Note that the abundance of the main isotopes of this group, excluding ^{18}F, and their total fraction in the envelope of the ONeMg dwarf is somewhat lower than for the CO dwarf. This is due to the fact that the initial abundance of CNO elements in the envelope is substantially higher for the CO dwarf, since, for the same q, it is determined by the composition of the dwarf.
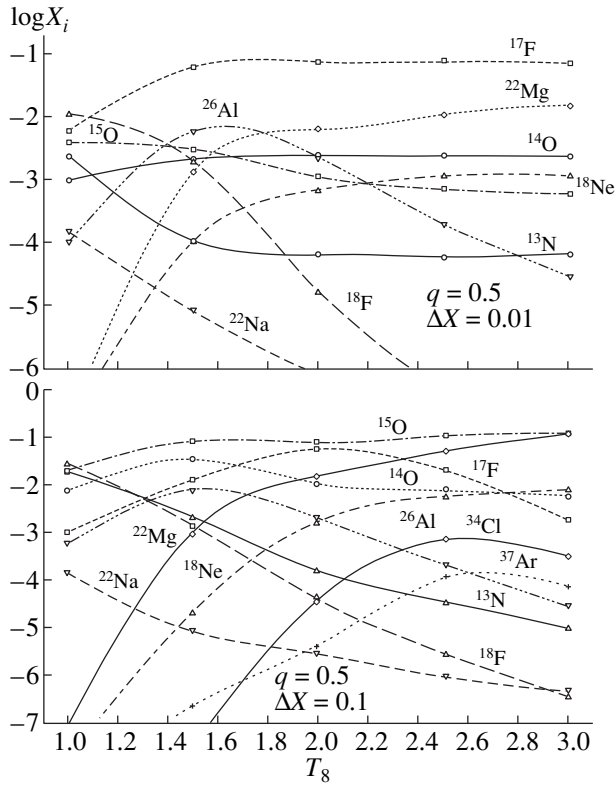
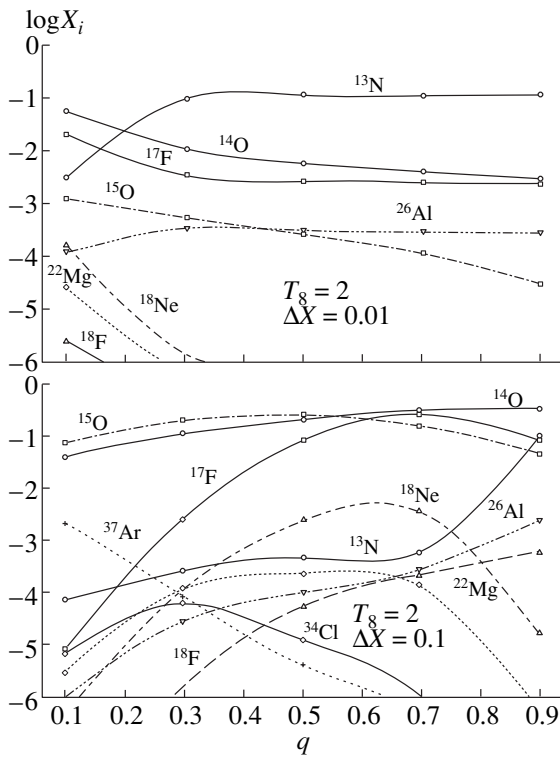**Fig. 2.** Same as Fig. 1 for an ONeMg dwarf.

Figures 3 and 4 present the abundances of the main radioactive isotopes for the CO and ONeMg dwarfs as a function of q for $T_8 = 2.0$. In the case of the CO dwarf (Fig. 3), at the burning stage $\Delta X = 0.01$, the sequence and number of main unstable isotopes (^{13}N, ^{14}O, ^{17}F, ^{15}O, ^{18}F) differ little from the $q = 0.5$ case described above for all $q > 0.3$. For the ONeMg dwarf (Fig. 4), the main product of burning at this stage is ^{17}F for all q, while ^{18}F (in the form of ^{18}Ne) exceeds 10^{-3} when $q < 0.4$.

At the burning stage $\Delta X = 0.1$, the most abundant isotopes in the CO dwarf are ^{15}O (20–25% of the mass for $q = 0.3$–0.5), ^{14}O (20–34% for $q \geq 0.5$), ^{17}F (8–26% for $q \geq 0.5$) and ^{13}N (1–10% for $q > 0.8$). The abundance of ^{18}F (in the form of ^{18}Ne) exceeds 10^{-3} for q from 0.35 to 0.75. In the ONeMg dwarf envelope, the main isotopes are ^{15}O (3–9% of the mass), ^{17}F (1–15% for $q > 0.3$), and ^{14}O (more than 1% for $q < 0.7$). The abundances of ^{18}F (together with ^{18}Ne) and ^{13}N exceed 10^{-3} for $q > 0.35$ and $q > 0.85$, respectively.

Thus, the total abundances of NOF isotopes in the envelopes of both types of dwarf after burning several percent of their hydrogen are essentially equal to the initial CO fraction in the dwarf; i.e. they are proportional to q. The relative abundances of individual isotopes depend substantially on the fraction of hydrogen burned ΔX, the temperature, and the mixing parameter. Under the same conditions, the NOF-isotope abun-

Fig. 3. Abundance of radioactive isotopes in the envelope as a function of the fraction of CO dwarf material in the envelope for a burning temperature $T = 2 \times 10^8$ K. The initial hydrogen abundance is decreased by $\Delta X = 0.01$ (above) and $\Delta X = 0.1$ (below).
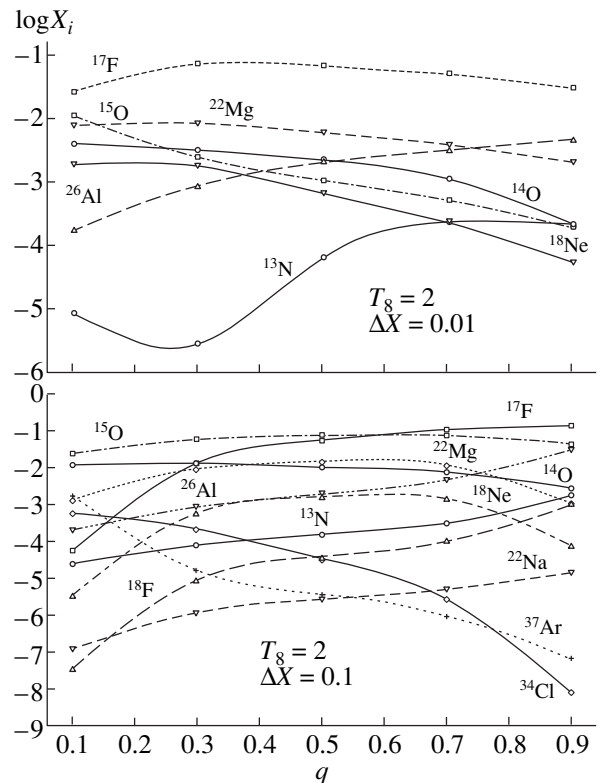

Fig. 4. Same as Fig. 3 for an ONeMg dwarf.

Table 1. Isotope composition for the typical ($T_8 = 2$, $q = 0.5$) and optimistic ($T_8 = 1$, $q = 0.7$) cases

White dwarf type	ε, 10^{17} erg/g	^{13}N (862 s)	^{14}O (102 s)	^{15}O (176 s)	^{17}F (95 s)	^{18}F (158 min)	^{22}Na (3.75 g)	^{26}Al (1.04×10^6 g)
CO	4.5	4.8e–4	2.1e–1	2.5e–1	8.4e–2	2.4e–3	2.3e–4	9.4e–5
ONeMg	5.6	1.6e–4	1.1e–2	8.1e–2	6.0e–2	1.7e–3	1.6e–2	2.0e–3
CO	6.1	1.0e–1	2.1e–2	5.8e–2	5.4e–3	7.4e–3	2.5e–7	5.5e–6
ONeMg	6	2.3e–2	4.2e–3	1.4e–2	1.0e–3	3.9e–2	2.0e–4	6.1e–4

Note: The lifetimes of the isotopes are given in parentheses.

dance in CO dwarfs is a factor of several higher than in ONeMg dwarfs, due to the different abundances of C and O in the admixed dwarf material. The abundance of the relatively longer lived ^{18}F is usually 10^{-3}–10^{-2}.

The abundance of ^{22}Na presented in Table 1 takes into account the fact that the short-lived isotope ^{22}Mg ($\tau = 5.6$ s) decays into ^{22}Na. As a result, if the burning temperature is sufficiently high, $T_8 > 2.0$, the ^{22}Na fraction in the ONeMg-dwarf envelope becomes higher than 0.01 over a broad interval $q = 0.3$–0.7 (Figs. 1–4). The ^{22}Na abundance in the CO-dwarf envelope is appreciably lower than for the ONeMg dwarf, and, as a rule, does not exceed 10^{-3}. The ^{26}Al fraction in the ONeMg dwarf (10^{-4}–10^{-2}) is also considerably higher than for the CO dwarf (10^{-5}–10^{-3}).

Table 1 presents the results of our abundance calculations for the main radioactive isotopes for the CO and ONeMg dwarfs in two cases. The first (typical) case corresponds to the average temperature and mixing parameter ($T_8 = 2$, $q = 0.5$). The second (optimistic) case reflects the conditions $T_8 = 1$ and $q = 0.7$, for which the abundance of ^{18}F is close to maximum for both types of dwarfs. Note that the mixing parameter $q = 0.7$ is close to the maximum abundance of heavy elements in nova envelopes [1]. We adopted $\Delta X = 0.1$ in all cases and assumed that the burning zone encompasses some fraction ψ of the envelope, to which the abundances in Table 1 correspond. This value will be determined from the energy balance: The nuclear energy released in this zone must equal the sum of the gravitational binding energy and kinetic energy of the envelope.

The distribution of radioactive isotopes in the expanding nova envelope depends on material from the burning zone mixing with the rest of the envelope. We will describe such mixing using the parameter f_{mix}, which represents the relative mass of the inner part of the envelope where the mixing of material from the burning zone is complete.

3. ANNIHILATION GAMMA-LINE LUMINOSITY

The NOF-isotope decays presented in Table 1 are all positron decays, with the exception of ^{18}F, for which a small fraction of decays (3%) occur via electron capture. We are interested here in the annihilation line

(0.511 MeV) and only directly emitted gamma photons, i.e., those that have not undergone any scattering.

Since the distribution of mass with radius and velocity in nova envelopes is not well known, it is reasonable to consider various models. We will take as a standard model a homologously expanding sphere ($v = r/t$, $v < v_1$) with a density that is constant with radius. In this case, naturally, the density decreases as a function of time according to a $\rho \propto t^{-3}$ law. We denote this model HH ("homologous homogeneous"). To estimate the effect of the density distribution, we will also consider a homologously expanding envelope with a power-law decrease of the density $\rho \propto t^{-3} v^{-7}$ in the velocity interval $v_0 < v < v_1$. In this type of envelope, the velocity at the outer boundary exceeds that at the inner boundary by a factor of three: $v_1 = 3v_0$ (we call this the HP, or "homologous power-law," model). A free-expansion model corresponds to a relatively rapid, burstlike acceleration of the envelope. As an alternative model, we also consider the case of a prolonged outflow of the envelope in the form of a stellar wind with constant velocity v_1 and constant mass-loss rate (the W, or "wind," model). In this case, we assume that the wind "switches on" sharply at the moment of the outburst.

The free parameters of these models are the total mass of the ejected envelope and the velocity of the matter at the outer boundary (or the wind velocity in the W model). We can easily calculate the kinetic energy of the envelope, and, for a given mass and radius of the dwarf ($M = 1M_\odot$, $R = 0.01R_\odot$), using energy conservation, we can also determine the fraction of the envelope (ψ) in which thermonuclear burning is complete. In the W model, the mass-loss rate is determined by setting the kinetic luminosity of the wind $L_k = \dot{M} v^2/2$ equal to the Eddington luminosity (10^{38} erg/s). The adopted parameters for the envelope expansion velocity correspond to the novae that are both photometrically and kinematically the fastest.

We can calculate the flux of directly emitted gamma photons assuming that they are emitted only from an optically thin outer layer ($\tau = 1$) with mass M_{em}. In this approximation, the nova luminosity in the gamma line is

$$L = 4\pi d^2 F = C(\tau)\eta M_{em},$$

where d is the distance; F, the flux; η, the coefficient of gamma radiation per gram of mass, which is deter-
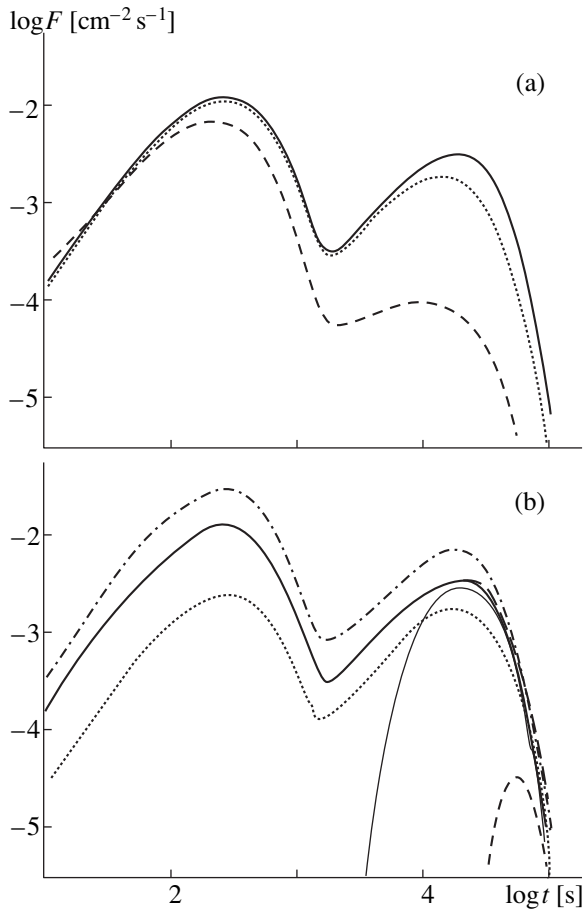
$\log F \ [\mathrm{cm}^{-2}\,\mathrm{s}^{-1}]$

Fig. 5. Annihilation-line flux from model nova outbursts at a distance of 1 kpc for the typical nucleosynthesis case. (a) The impact of different types of kinematics and density distributions for the homologous uniform model HH1 (solid), the homologous power-law HP model (dotted), and the wind model W (dashed). (b) The effect of varying the structure parameters and composition in the HH1 model (thick solid curve) for models without mixing HH2 (short-dashed curve), with partial mixing HH3 (thin solid curve), with larger mass HH4 (long-dashed curve), with larger velocity HH5 (dash–dotted curve), and for the case of an ONeMg dwarf HH6 (dotted curve).

mation of positronium [23]. Ultimately, the fraction of two-photon annihilations is determined by the degree of thermalization of the singlet and triplet states of positronium. When there is total thermalization at all levels, primarily two-photon annihilation occurs, since the probability for annihilation from the singlet state is substantially higher than from the triplet state. When the degree of thermalization is low, the fraction of three-photon annihilations becomes 3/4 of the rate of positronium annihilations (the probability of recombination is proportional to the statistical weight). We calculated the relative populations for the singlet and triplet levels of positronium using the collisional and radioactive transition rates from [23]. We assumed that the hydrogen and helium in the nova envelope were fully ionized, which is a reasonable assumption for the early stage of the outburst.

Figure 5a presents the fluxes for the HP and HH1 homologous models and the W model, providing an estimate of the impact of the envelope structure on the luminosity and evolution of the annihilation line. The light curve has two maxima: The first is due to short-lived ^{13}N, ^{14}O, and ^{15}O, while the second corresponds to relatively long-lived ^{18}F. Table 2 presents the initial parameters of the models (the type of dwarf, mass of the envelope, velocity at the outer boundary, fraction of mixed material in the envelope f_{mix}) and the resulting parameters: the mass of the burning zone as a fraction of the total envelope mass ψ, the maximum flux at the second maximum F, the "fluence" (time integral of the flux), and width of the second maximum Δt determined from the ratio of the fluence and maximum flux. In the first three models, the envelope mass and velocity at the outer boundary are the same, and we have assumed complete mixing of burning products in the envelope ($f_{mix} = 1$). In the W model, the mass-loss rate for the given parameters is $5 \times 10^{-5} \ M_\odot$, which corresponds to an envelope outflow time of around four months. The increased strength of the second flux maximum in the HH1 model compared to the HP model is due to the fact that the density in the outer layers is greater in the HH1 than in HP model. As a result, the average radius—and, consequently, the mass of the transparent outer layer—is larger in the HH1 model ($M_{em} \propto r^2$). In the wind model, the flux is lower still, since the wind density (and the mass of the transparent wind layer) is lower.

Figure 5b illustrates the impact of the remaining free parameters for a homologous envelope with constant density (Table 2, models HH1–HH6). The absence of mixing of the burning products with the bulk of the envelope ($f_{mix} = \psi$, model HH2) strongly decreases the flux compared to the case of complete mixing. Note that the first peak is substantially suppressed even when there is nearly complete mixing, when only 1% of the envelope material is unmixed (model HH3). This makes it unlikely that we will observe the first luminosity peak associated with short-lived isotopes. Increasing the envelope mass by a factor of five (model HH4) leaves the light curve virtually unaffected, since the mass of

mined by the isotope composition and probability of two-photon annihilation; and $C(\tau)$, a factor close to 0.25 for a total envelope optical depth $\tau_0 \gg 1$ (for a geometrically thin atmosphere, it is precisely 0.25). If the entire envelope is optically thin, C is obviously equal to 1. From this point on, we will use the approximation $C(\tau) = 1 - 0.75[1 - \exp(-\tau)]$, which is valid for any τ_0. The accuracy of this approximation is fairly high; for example, in the case of a uniform sphere, it deviates from the exact analytical solution of the radiation transfer equation by no more than 5%.

When calculating the radiation coefficient for the 0.511-MeV annihilation line, we must take into account the fact that only about 10% of annihilation events occur via free, two-photon annihilation, whereas the remaining 90% of positrons annihilate via the for-

Table 2. Nova-envelope parameters and annihilation-line fluxes ($d = 1$ kpc)

Model	White dwarf type	M, $10^{-5}\,M_\odot$	V_{max}, km s^{-1}	f_{mix}	ψ	F, 10^{-4} cm^{-2} s^{-1}	Φ, cm^{-2}	Δt, 10^4 s
HP	CO	2	2500	1	0.31	19	53	2.8
HH1	CO	2	2500	1	0.34	33	107	3.2
W	CO	2	2500	1	0.28	1	2.6	2.6
HH2	CO	2	2500	0.34	0.34	0.3	1	3.7
HH3	CO	2	2500	0.99	0.34	28	85	3.1
HH4	CO	10	2500	1	0.34	34	116	3.4
HH5	CO	2	3500	1	0.38	70	214	3
HH6	ONeMg	2	2500	1	0.25	17	56	3.2
HH7	CO	2	2500	1	0.34	83	280	3.4
HH8	ONeMg	2	2500	1	0.25	400	1300	3.3

the radiating transparent outer layer does not depend on the density ($M_{em} = 4\pi r^2/k_\gamma$, where k_γ is the gamma-photon absorption coefficient) in an optically thick envelope with the same kinematics and density distribution. However, over a longer time scale, the model with the larger mass yields a larger flux, since the two-photon annihilation probability increases with the density. The enhanced luminosity in model HH5, which has a larger expansion velocity, can be easily understood, since the radiating mass is $M_{em} \propto r^2$. Figure 5b also presents the case of an ONeMg dwarf outburst (model HH6). For this model, all other factors being the same, the annihilation-line fluxes at both maxima are appreciably smaller than for the CO dwarf nova (model HH1), due to the reduced NOF-isotope abundance in the neon nova.

To estimate the influence of various burning conditions, which determine the synthesis of radioactive nuclei in the envelope, we present the case of high ^{18}F abundance in both dwarfs (the optimistic case; Table 1, Fig. 6). In this case, the CO dwarf nova (model HH7) has a ^{18}F annihilation-line flux that is a factor of 2.7 higher than the typical value (model HH1). In addition, in the optimistic case for a CO dwarf, the first luminosity maximum occurs later and is broader, due to the increase of the ^{13}N abundance (by a factor of ≈ 200). For the ONeMg-dwarf optimistic case (model HH8), the annihilation-line flux resulting from ^{18}F decay is a factor of 23 higher at the maximum than in the typical ONeMg dwarf model (model HH6), while the first luminosity maximum is absent. Note that, in this case, the maximum flux for the ONeMg-dwarf outburst is a factor of five higher than the flux of the second maximum for the CO dwarf.

4. DISCUSSION AND CONCLUSION

Our single-zone kinetic calculations of thermonuclear burning in hydrogen-rich material for various nova-outburst parameters have yielded broad intervals for the abundances of NOF isotopes, and also of ^{22}Na

and ^{26}Al. These ranges for the abundances of radioactive nuclei encompass the results of the most well-known nova nucleosynthesis calculations [1–12]. Calculations for different parameters give rise to substantially different values for the annihilation-line flux.

In addition, for a constant isotope abundance, the annihilation-line flux exhibits an appreciable dependence on both the structure of the ejected envelope of the nova (compare, for example, the homologous-envelope and wind-outflow models) and, of course, on the velocity at the outer boundary. Even more substantial variations of the flux can result from incomplete mixing of the burning products in the envelope. This is especially important for the initial phase of the light curve, when the optical depth to gamma photons is large. For example, the luminosity peak associated with short-lived isotopes can be completely suppressed if only 1% of the mass outside the envelope does not contain radioactive nuclei. This fact, together with the low energy
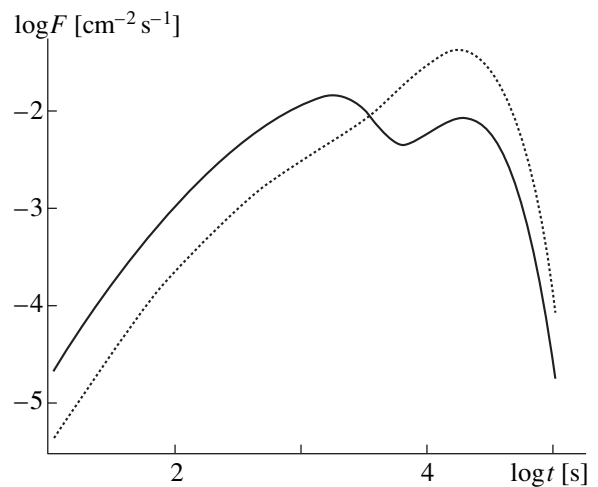

Fig. 6. Annihilation-line flux for the optimistic nucleosynthesis case in the HH7 model for the envelope of a CO dwarf (solid) and in the HH8 model for the envelope of an ONeMg dwarf (dotted).

(small fluence) involved, makes detection of the first peak problematic.

The maximum fluxes in the ^{18}F annihilation line presented in Table 2 obtained for various parameters fall within the range from 1×10^{-4} to 4×10^{-2} cm^{-2} s^{-1} at the distance of 1 kpc for an event duration of $(2–4) \times 10^4$ s. It is important that, in the optimistic case for the model with homogeneous mixing, the flux is close to the maximum possible value, since nearly the maximum values for the observed heavy-element abundance and the envelope velocity are used. The main characteristics of the light curves in the annihilation line noted in [23, 24] closely correspond to our results for the optimistic case (a short-time scale peak and subsequent maximum about six hours after the beginning of the thermonuclear outburst, maximum fluxes around 10^{-2} cm^{-2} s^{-1} for a distance of 1 kpc, duration of the events of about 12 hours). As noted in these studies, this implies that modern detectors make it possible to detect nova outbursts at distances of several kpc, while INTEGRAL could detect such events at the Galactic center.

How could the annihilation line observations be used to diagnose isotope synthesis and the structure of the envelope? Suppose an observational estimate of the flux (or an upper limit) is available. Since the luminosity of a nova at the second maximum is determined not only by the mass of synthesized ^{18}F but also by the envelope structure (i.e., by mixing), gamma observations alone cannot unambiguously yield the main parameters determining the flux. The situation changes substantially if subsequent observations of the nova provide us with the ^{18}O abundance in the ejected matter. No attempts to measure the isotopic compositions of novae envelopes have been made thus far; in the future, however, such measurements could be realized. For example, sensitive spectrometers could be used to try to analyze the abundances of CO molecules, which should appear at the stage of dust formation or the stage immediately preceding this. It will be possible to confidently measure isotope splitting (^{12}C^{16}O and ^{12}C^{18}O) in vibrational–rotational lines, even taking into account the expansion velocity. Given the ^{18}O abundance in a nova envelope and the ^{18}F annihilation-line flux (or an upper limit for it), conclusions could be drawn concerning the burning conditions in the thermonuclear outburst and the degree of mixing of radioactive nuclei in the envelope.

In addition to the annihilation line, novae should also radiate a comptonized gamma continuum. It was shown in [23, 24] that, for the standard energy resolution of a detector, the line flux is an order of magnitude higher than the continuum flux. For this reason, the gamma annihilation line should be clearly seen against the background of the intrinsic gamma continuum of a nova.

Currently, the most prolonged and complete searches [28] of gamma transients in the vicinity of 0.5 MeV, with durations of 0.5–3 days and sensitivities $\simeq 2 \times 10^{-3}$ cm^{-2} s^{-1} made with the CGRO BATSE detector, have not detected such transients over an observation time exceeding two years (June 1991–December 1993). For a flux of 4×10^{-2} $(d/1$ kpc$)^{-2}$ cm^{-2} s^{-1}, corresponding to the optimistic case for an ONeMg dwarf, and for the indicated sensitivity, the annihilation lines from novae should be detectable at distances $d < 4.5$ kpc. At least three neon novae have experienced outbursts over this time at distances closer than 3.5 kpc [14]. Unfortunately, no attempts to determine upper limits for the annihilation-line fluxes from these novae have been published. The next generation of detectors onboard the INTEGRAL satellite are very promising for observations of novae in the annihilation line.

In our models, the ^{22}Na abundance in the burning zone of an ONeMg dwarf is one or two orders of magnitude higher than for a CO dwarf and reaches 0.01–0.12. The mass of ^{22}Na in the ejected material is determined by the equality $M(^{22}\text{Na}) = X(^{22}\text{Na})\psi M$. Assuming the total mass of the envelope to be $M = 10^{-4} M_\odot$, which is a typical value according to modern observational estimates [1], and also assuming $\psi = 0.25$, we obtain a possible range for the ejected mass of ^{22}Na of 2.5×10^{-7} to 3×10^{-6} $M_\odot$. The observational upper limit for the ejected mass of ^{22}Na derived from the 1.275-MeV gamma line in the nearest ($d = 1.77$ kpc [29]) well studied neon nova, V1974 Cyg, is 2.4×10^{-8} $M_\odot$ [14]. This discrepancy suggests that, in reality, the ^{22}Na abundance in the burning zone is $X(^{22}\text{Na}) < 0.001$. It follows that, except for those made for the lowest temperatures and low values for the mixing parameter, most of our calculations are not consistent with the observations.

The low ^{22}Na abundance could be due to a low burning temperature. This would correspond to smaller dwarf masses, which could occur in an alternative model for neon novae with appreciable enrichment of the CO-dwarf outer layer with neon and magnesium [30]. Another possibility is that some of the true reaction rates in the NeNa-cycle differ [3] from those we have adopted. In any case, ^{22}Na should be formed in the process of hot hydrogen burning in the envelope and should be manifest observationally in sufficiently nearby events, given the increasing sensitivity of gamma detectors.

The mass of ^{26}Al in the ejected envelope of a neon nova for the M and ψ values adopted above is 2.5×10^{-9}–2.5×10^{-7} $M_\odot$. Given a neon nova rate of 10/year [31] and the known lifetime of ^{26}Al nuclei (Table 1), the total mass of ^{26}Al ejected by novae should be between 0.025–2.5 $M_\odot$. Needless to say, this estimate could change substantially if the properties and of neon novae and their outburst rate differ appreciably from the values we have adopted. Thus, in the optimistic limit, novae could provide the total amount of ^{26}Al observed in the Galaxy. Note that, in all studies of ^{26}Al synthesis, the calculations have assumed that CO dwarfs are made up of the two isotopes ^{12}C and ^{16}O. At the same time, CO dwarfs also contain other products of helium burning, among which ^{22}Ne and ^{25}Mg are fairly abundant [32, 33]. Taking this into account in our calculations

appreciably increases the ^{26}Al abundance for CO dwarfs [25, 34]. The contribution of CO novae to the synthesis of ^{26}Al is about 30%, which is comparable to the contribution of ONeMg novae.

Recently, however, estimates for the abundances of synthesized ^{26}Al in neon novae have tended to decrease, due to changes in estimates of the rates for some reactions in the MgAl cycle [1, 35] and of the compositions of the ONeMg dwarfs [3, 12], based on the most recent results on the formation of these dwarfs [36]. The uncertainties in the nuclear-reaction rates [37], lack of calculations for nova outbursts in CO dwarfs with Ne- and Mg-enriched outer layers, and poorly known properties of the Galactic nova population make it impossible to determine unambiguously the contribution of novae to the total amount of ^{26}Al in the Galaxy and, consequently, to the overall observed radiation in the aluminum line.

ACKNOWLEDGMENTS

REFERENCES

1. S. Starrfield, J. W. Truran, M. C. Wiescher, *et al.*, Mon. Not. R. Astron. Soc. **296**, 502 (1998).
2. A. Kovetz and D. Prialnik, Astrophys. J. **477**, 356 (1997).
3. J. José and M. Hernanz, Astrophys. J. **494**, 680 (1998).
4. W. Hillebrandt and F.-K. Thielemann, Astrophys. J. **255**, 617 (1982).
5. M. Wiescher, J. Gorres, F.-K. Thielemann, and H. Ritter, Astron. Astrophys. **160**, 56 (1986).
6. R. D. Hoffman and S. E. Woosley, Bull. Amer. Astron. Soc. **18**, 948 (1987).
7. M. T. Wolff and M. D. Leising, *Workshop on Nuclear Spectroscopy of Astrophysical Sources* (New York, 1988), p. 136.
8. A. Weiss and J. W. Truran, Astron. Astrophys. **238**, 178 (1990).
9. I. Nofar, G. Shaviv, and S. Starrfield, Astrophys. J. **369**, 440 (1991).
10. M. Politano, S. Starrfield, J. W. Truran, *et al.*, Astrophys. J. **448**, 807 (1995).
11. A. Coc, R. Mochkovitch, Y. Oberto, *et al.*, Astron. Astrophys. **299**, 479 (1995).
12. J. José, M. Hernanz, and A. Coc, Astrophys. J. Lett. **479**, L55 (1997).
13. D. D. Clayton and F. Hoyle, Astrophys. J. **187**, L101 (1974).
14. A. F. Iyudin, K. Bennett, H. Bloemen, *et al.*, Astron. Astrophys. **300**, 422 (1995).
15. M. J. Harris, W. R. Purcell, D. A. Grabelsky, *et al.*, Astron. Astrophys., Suppl. Ser. **120**, 343 (1996).
16. W. A. Mahoney, J. C. Ling, A. S. Jacobson, and R. E. Lingenfelter, Astrophys. J. **262**, 742 (1982).
17. R. Diehl, C. Dupraz, K. Bennett, *et al.*, Astron. Astrophys. **298**, 445 (1995).
18. U. Oberlack, R. Diehl, T. Montmerle, *et al.*, Astrophys. J., Suppl. Ser. **92**, 433 (1994).
19. R. Diehl, K. Bennett, H. Bloemen, *et al.*, Astron. Astrophys. **298**, L25 (1995).
20. R. Diehl, A. Iyudin, U. Oberlack, *et al.*, Nucl. Phys. A A**621**, 79 (1997).
21. J. Knoedlseder, K. Bennett, H. Bloemen, *et al.*, Astron. Astrophys., Suppl. Ser. **120**, 327 (1996).
22. U. Oberlack, K. Bennett, H. Bloemen, *et al.*, Astron. Astrophys., Suppl. Ser. **120**, 311 (1996).
23. M. D. Leising and D. D. Clayton, Astrophys. J. **323**, 159 (1987).
24. J. Gómez-Gomar, M. Hernanz, J. José, and J. Isern, Mon. Not. R. Astron. Soc. **296**, 913 (1998).
25. A. D. Kudryashov and A. V. Tutukov, Astron. Zh. **72**, 559 (1995).
26. O. A. Bessonov, A. D. Kudryashov, and É. V. Érgma, Astrofizika **14**, 161 (1978).
27. W. D. Arnett and J. W. Truran, Astrophys. J. **157**, 339 (1969).
28. D. M. Smith, M. Leventhal, R. Cavallo, *et al.*, Astrophys. J. **471**, 783 (1996).
29. D. Chochol, J. Grygar, T. Pribulla, *et al.*, Astron. Astrophys. **318**, 908 (1997).
30. D. Prialnik and M. M. Shara, Astron. J. **109**, 1735 (1995).
31. U. Kolb and M. Politano, Astron. Astrophys. **319**, 909 (1997).
32. I. Iben and A. V. Tutukov, Astrophys. J., Suppl. Ser. **58**, 661 (1985).
33. W. D. Arnett and F.-K. Thielemann, Astrophys. J. **295**, 589 (1985).
34. A. D. Kudryashov, *Eruptive Stars* [in Russian] (1996), p. 117.
35. S. Starrfield, J. W. Truran, M. Wiescher, *et al.,* Nucl. Phys. A A**621**, 495 (1997).
36. C. Ritossa, E. García-Berro, and I. Iben, Astrophys. J. **460**, 489 (1996).
37. J. José, A. Coc, and M. Hernanz, astro-ph/9811335.

Translated by K. Maslennikov

UBVRI Photometry and Polarimetry
of the Spotted Red Dwarf MS Ser

I. Yu. Alekseev

Crimean Astrophysical Observatory, Ukrainian Academy of Sciences,
Nauchnyĭ, Crimea, 334413 Ukraine
Received August 18, 1998

Abstract—*UBVRI* photometry of the poorly studied spotted star HD 143313 (MS Ser) was carried out in 1991–1997, supplemented with polarization observations in 1996–1997. These observations confirmed the presence of BY Dra-type variability and reliably detected the star's intrinsic polarization, which is variable in the *U* band. A model for the star's spottedness that is consistent with the polarimetry data was constructed based on the collected photometric data. The model calculations suggest that the spotted areas cover up to 15% of the total stellar surface and are about 1500 K cooler than the surrounding photosphere. © *2000 MAIK "Nauka/Interperiodica".*

1. INTRODUCTION

Spottedness is a quite common phenomenon among cool, low-luminosity stars. The axial rotation of a nonuniformly spotted star and slow changes of its spot configuration on time scales of several months can give rise to BY Dra-type photometric variability: rotational brightness modulations and slow changes of the mean brightness of the star (see, for example, the review in [1]).

Like sunspots, spotted areas on red dwarf stars have rather strong magnetic fields (~1–2 kG). These fields result in Zeeman splitting and polarization of absorption lines in the stellar spectrum. For observations in broad photometric bands, the effects of the lines in the band add, and the resultant polarization of the stellar radiation is weak.

In the late 1950s and early 1960s, broadband linear polarization of light from solar active regions was discovered [2, 3]. Later, there were many attempts to detect linear polarization in a variety of dwarf stars. Piirola [4] detected variable intrinsic linear polarization in the F8 dwarf HD 142373. Based on data for the nearest stars, Piirola [4] also found a tendency for the polarization to grow toward later spectral types. A similar result was obtained by Tinbergen and Zwaan [5]. Koch and Pfeiffer [6] considered the linear polarization of the known spotted star BY Dra and found variability in the *R* band that did not correlate with the orbital revolution. Pettersen and Hsu [7] investigated the polarization of 19 flaring and spotted stars and failed to detect rotational modulation in BY Dra and EV Lac. Pettersen *et al.* [8] found rotational modulation of the *V*-band polarization in HK Aqr, with the same period as that of the brightness variations. The polarization maxima were shifted with respect to the brightness minimum by 0.29 and 0.58 of the period. Huovelin *et al.* [9–11] studied rotational modulation of the polarization of ten solar-type stars, including the spotted star BE Cet, and compared it with the variability of the CaII H and K emission lines.

Here, we consider variability of the brightness and linear polarization of the active spotted star MS Ser, associated with spotted regions on its surface. MS Ser (HD 143313) is a spectral binary whose components have spectral types K2Ve and K6Ve [12]. The earliest photometric data for this star were published by Eggen [13]: $V = 8^{m}.33$, $U–B = 0^{m}.72$, $B–V = 1^{m}.00$. It was found to be a photometric variable by Rucinski [14] and Bopp *et al.* [15], who also identified the period of the star to be $P_{rot} = 9^{d}.60$, slightly different from the orbital period ($9^{d}.01$). The star's light curve could abruptly change its shape, accompanied by the complete disappearance of rotational modulation [16]. Alekseev and Shakhovskaya [17] confirmed the existence of variability of MS Ser with the indicated period. Ours are the first polarization observations of this star.

2. OBSERVATIONS AND RESULTS

Our observations were carried out on the 1.25-m AZT-11 reflector of the Crimean Observatory. The telescope was equipped with the *UBVRI* photometer-polarimeter of Piirola [18]. We obtained only photometric observations in 1991, 1994, and 1995 (10, 14, and 4 nights, respectively) and quasi-simultaneous photometric and polarization observations in 1996 and 1997 (10 and 9 nights, respectively). The observation procedures are described in detail by Alekseev and Shakhovskaya [17] (photometry) and Huovelin *et al.* [9–11] (polarization). We used BD + 26°2762 as a comparison star ($V = 8^{m}.08$, $U–B = 0^{m}.73$, $B–V = 1^{m}.08$); $V–R = 0^{m}.65$, $V–I = 1^{m}.28$, tying it to HD 143455) [14], and BD +

$26°2623$ as a control star ($V = 10\overset{m}{.}71$, $U–B = 1\overset{m}{.}30$, $B–V = 1\overset{m}{.}29$, $V–R = 1\overset{m}{.}02$, $V–I = 1\overset{m}{.}86$) [19]. The errors in the brightness of MS Ser and its color indices do not exceed $0\overset{m}{.}01$.

Preliminary results of the 1991, 1994, and 1995 observations were published in [17, 20]. Figure 1 shows the light curves of the star convolved with the ephemeris of Bopp *et al.* [15]:

$$\min \mathrm{JD} = 2\,444\,311.96 + 9\overset{d}{.}60E. \tag{1}$$

The light curves differ rather strongly from sine waves. In 1991 and 1994, there is a wide scatter in the data, probably due to rapid changes in the light curve. Changes of the amplitude, mean brightness, and phase of the rotational-modulation minimum from season to season are clearly visible in the figure; this is characteristic of BY Dra-type variability.

Table 1 lists the main results of the photometric observations: the observation epochs, mean brightness of the star, amplitude of the rotational modulation, color indices, and phase of the brightness minimum. Based on our own observations and data taken from the literature [13–17], we plotted a master light curve for MS Ser (Fig. 2). Figure 2 shows that the amplitude of the rotational modulation in our observations was between $0\overset{m}{.}05$ and $0\overset{m}{.}15$ (this is the largest value for this quantity over the entire observation time), while the mean brightness varied by $0\overset{m}{.}13$ (the corresponding variations for the entire observation time constituted $0\overset{m}{.}18$), in good agreement with earlier results. The color indices we have found are also consistent with the data of [13, 14] (except for *V–R*). A comparison of our results with the data of [13–17] showed that the star reached its maximum brightness in 1980: $V_{\max} = 8\overset{m}{.}11$.

In May 1996–June 1997, we carried out measurements of the linear polarization of MS Ser simultaneously with the photometry. We obtained nine observations in each season. Tables 2 and 3 present the results of these observations. For each Stokes parameter, P_x and P_y, we give its variance σ, the value of χ^2, and the corresponding probability F_{var} of the parameter being variable. Tables 2 and 3 also list the mean degree of polarization with its variance, together with the
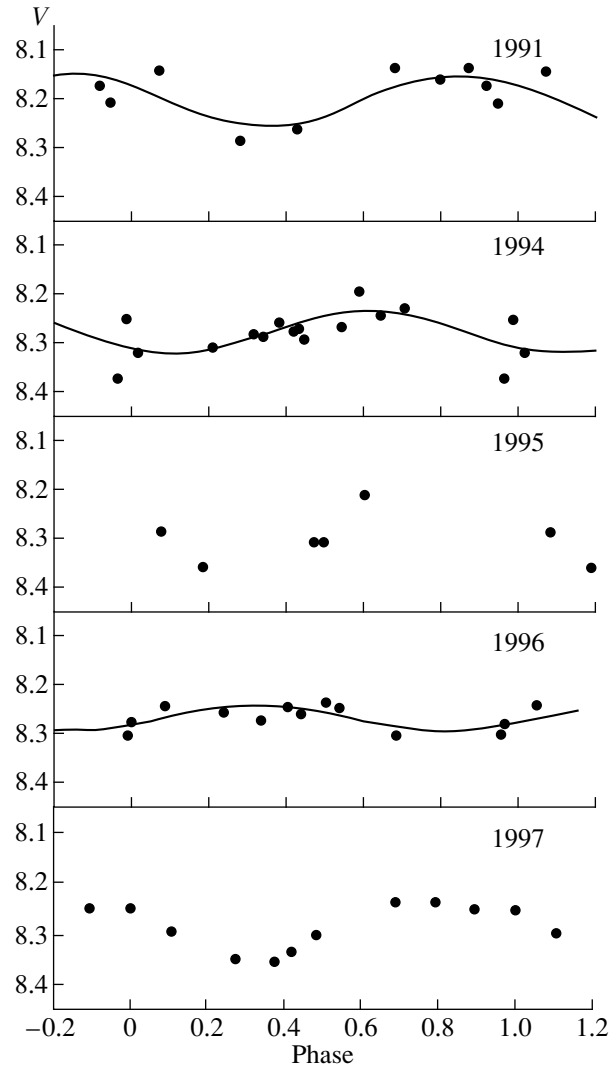

Fig. 1. *V*-band light curves of MS Ser; the points show the observational data, and the solid curve the best-fit sine wave.

quantity P_s introduced by Huovelin *et al.* [10]—the mean value of all degrees of polarization differing from zero by more than 2σ. According to [10], this quantity can serve as an estimate of the maximum observed degree of polarization.

We can see from Tables 2 and 3 that the emission of the star is weakly polarized in all bands. Polarization

Table 1. Photometry of MS Ser

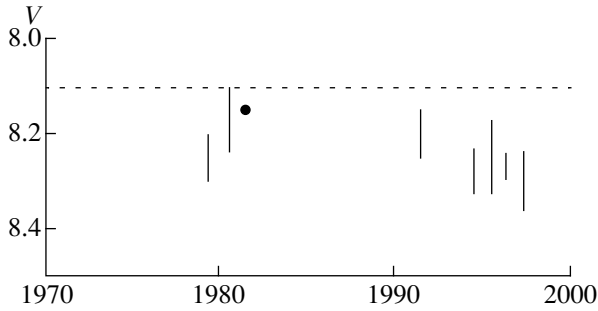| Epoch	$\langle V \rangle$	ΔV	*U–B*	*B–V*	*V–R*	*V–I*	Phase
1991.5	8.20	0.10	0.66	1.04	0.74	1.44	0.34
1994.5	8.28	0.09	0.67	1.04	0.74	1.44	0.11
1995.5	8.25	0.15	0.66	1.03	0.72	1.41	0.30
1996.3	8.27	0.05	0.67	1.04	0.74	1.45	0.84
1997.4	8.30	0.12	0.66	1.04	0.73	1.45	0.38

Fig. 2. Master *V*-band light curve of MS Ser.

where

$$X_\lambda = L_2/(L_1 + L_2), \qquad (3)$$

and L_1 and L_2 are the luminosities of the system's components at this wavelength [22]. We assume that only the primary component is spotted and that the role of the secondary is reduced to "smearing" the photometric effect of the spotting. Formula (2) contains two temperature parameters,

$$a_\lambda = 1 - u_\lambda^{ph} - (1 - u_\lambda^{sp})\beta_\lambda \qquad (4)$$

and

$$b_\lambda = u_\lambda^{ph} - u_\lambda^{sp}\beta_\lambda \qquad (5)$$

and two geometric parameters: the projected area *I* of the spots, expressed in terms of the visible stellar disk area

$$\pi I = \int \cos\alpha \sin\theta d\theta d\phi \qquad (6)$$

and the mean cosine *J* of the angular distance α between the geometric centroid of the spot and the stellar disk center

$$\pi J = \int \cos^2\alpha \sin\theta d\theta d\phi. \qquad (7)$$

The integration in (5) and (6) is performed over the visible part of the spotted area (θ and ϕ are the polar angle and longitude of a point, u_λ are limb-darkening coefficients, and β_λ is the brightness ratio of the spot and quiescent photosphere). The magnitude difference Δm_λ is measured from the brightness level of the spot-free photosphere.

To determine the area and temperature of the spotted region, we need to know the brightness of the spot-free photosphere and the relationships between the values

variability is detected only in the *U* band, marginally in 1996 but quite reliably in 1997. Figure 3 presents the run of the polarization degree and position angle convolved with the period of the rotational modulation and shown with the light curve of the star. The phase shift between the brightness minimum and the maximum of the degree of polarization is 0.2 in 1996 and 0.1 in 1997. This agrees well with the value expected theoretically (0.12–0.25, depending on the area of the magnetized region [21]).

3. MODELING

A cool, spotted region on the surface of a binary star creates a deficit of the emission flux at the wavelength λ, determined from the formula

$$\Delta m_\lambda = -2.5\log((1 - (a_\lambda I + b_\lambda J)/(1 - u_\lambda^{ph}/3)) \times ((1 - X_\lambda) + X_\lambda), \qquad (2)$$

Table 2. Linear Polarization of MS Ser in 1996

Band	$\langle P_x \rangle$	σ	χ^2	F_{var}	$\langle P_y \rangle$	σ	χ^2	F_{var}	$\langle P \rangle$	σ	P_s
U	0.064	0.083	0.67	28.2	0.023	0.111	1.10	63.1	0.137	0.057	0.170 ± 0.016
B	−0.049	0.050	0.67	28.1	0.026	0.040	0.30	3.5	0.077	0.028	0.093 ± 0.020
V	0.025	0.037	0.36	7.6	0.001	0.036	0.30	3.7	0.050	0.024	0.076 ± 0.011
R	−0.023	0.025	0.26	2.1	0.010	0.026	0.24	1.7	0.039	0.018	0.066 ± 0.004
I	0.007	0.027	0.28	1.7	0.029	0.025	0.18	<1	0.045	0.012	0.047 ± 0.003

Table 3. Linear Polarization of MS Ser in 1997

Band	$\langle P_x \rangle$	σ	χ^2	F_{var}	$\langle P_y \rangle$	σ	χ^2	F_{var}	$\langle P \rangle$	σ	P_s
U	0.077	0.152	2.42	99.6	0.046	0.149	1.60	87.4	0.206	0.080	0.241 ± 0.018
B	−0.023	0.050	0.45	10.6	0.045	0.050	0.53	17.1	0.076	0.037	0.111 ± 0.010
V	0.017	0.050	0.42	9.2	0.053	0.044	0.43	9.5	0.081	0.022	0.081 ± 0.007
R	0.008	0.022	0.18	<1	0.014	0.030	0.27	2.7	0.037	0.014	0.047 ± 0.004
I	−0.003	0.026	0.25	1.9	−0.005	0.042	0.25	2.0	0.040	0.027	0.069 ± 0.011

Table 4. Input Model Parameters

Year	$\Delta B/\Delta V$	$\Delta R/\Delta V$	$\Delta I/\Delta V$
1991	1.08 ± 0.01	0.75 ± 0.06	0.70 ± 0.02
1994	1.06 ± 0.02	0.75 ± 0.05	0.69 ± 0.03
1995	1.08 ± 0.01	0.64 ± 0.08	0.70 ± 0.01
1996	1.04 ± 0.02	0.64 ± 0.09	0.78 ± 0.03
1997	1.05 ± 0.02	0.86 ± 0.04	0.79 ± 0.01
Average	1.06 ± 0.01	0.81 ± 0.03	0.74 ± 0.01

of Δm at various wavelengths (estimated from observations); we must also adopt an *a priori* hypothesis about the configuration of the spotted regions.

3.1. The Zonal Model

Alekseev and Gershberg [1, 20, 23, 24] showed that the set of spotted regions on a star can be represented by two spotted belts that are symmetric with respect to the equator, which occupy regions with latitudes from $\pm\phi_0$ to $\pm(\phi_0 + \Delta\phi)$, with the spot-filling density linear in longitude and ranging from unity to some fraction f_{min}, where $0 < f_{min} < 1$. This zonal model was applied to seventeen spotted dwarf stars [20, 24] and displayed a qualitative agreement with the solar spottedness pattern.

Table 4 presents the ratios of the amplitudes of the rotational modulation $\Delta B/\Delta V$, $\Delta R/\Delta V$, and $\Delta I/\Delta V$ we determined for MS Ser in individual observational seasons. The probabilities that the changes of these magnitudes from season to season are due to statistical fluctuations are 99% for $\Delta B/\Delta V$ and 65% for $\Delta R/\Delta V$ and $\Delta I/\Delta V$. In our calculations, we used the amplitude ratios determined from our entire set of 1991–1997 observations (the last line of Table 4), which take into account both rotational modulation and mean-brightness variability.

We estimated the luminosity ratios of the components of MS Ser from the characteristic values of M_V and the color indices given by Johnson [25]. We are not aware of any measurements of $v\sin\iota$ for this star; thus,

we will assume that $\iota = 90^\circ$. This assumption is supported by the system's orbital inclination, which is close to 90° [12]. In [23], we estimated the effect of uncertainty in the angle ι on the calculation results. The calculations show that, when ι decreases to 30°, the estimates of $\Delta\phi$ systematically increase by a factor of a few; the estimated f_{min} passes through a small maximum at about $\iota = 70^\circ$ and then decreases slightly, and the estimates of β_V increase by an amount corresponding to an increase of the blackbody temperatures by approximately 100 K. Thus, the assumption that $\iota = 90^\circ$ yields a lower limit for $\Delta\phi$, somewhat underestimates β_V, and virtually does not affect the filling factor. We estimated the temperature of MS Ser $T_{phot} = 4800$ K using Johnson's calibration and the color indices we derived from our data. The calculated parameters for the zonal spottedness models for MS Ser are given in Table 5.

It follows from Table 5 that the model with ϕ_0 is sufficient to describe the variability of MS Ser. In this case, the total width of the spotted equatorial belt $2\Delta\phi$ varies from 4° to 24°, the parameter f_{min} varies from 0.00 to 0.96, and this yields an area of the spotted regions not exceeding 15%. The spotted regions are rather cool: Their contrast is 0.08, corresponding to a temperature difference of 1500 K between the photosphere and spots.

The results of our modeling of the spottedness depend on the adopted geometry for the spots. To take this into account, we have also considered a traditional model with a round, high-latitude spot [26] and an intermediate model, in which

$$J = 2I/3, \qquad (8)$$

which is mathematically similar to a model without limb-darkening (see, for example, [17]). In our calculations in the round-spot approximation, the spotted regions are 2200 K cooler than the photosphere and their area reaches 26%; in the calculations using approximation (8), the temperature contrast is 2000 K, and the total spot area reaches 21% of the stellar surface. All three models describe the photometric observations of the star to roughly the same accuracy.

Table 5. Zonal Spottedness Models for MS Ser

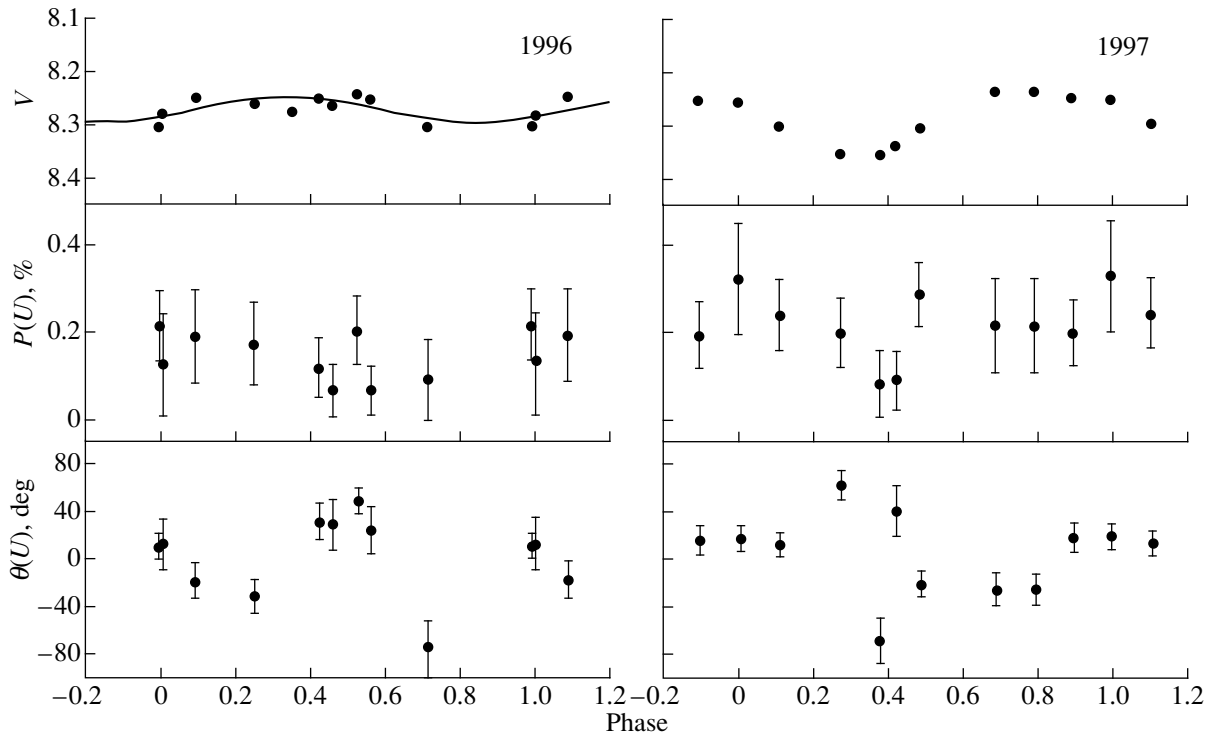| Epoch	ΔV_{max}	ΔV	ϕ_0	$\Delta\phi$	f_{min}	β_V	S_{max}	S_{min}	Reference
1979.3	0.09	0.10	0	10.6	0.26	0.07	7.5	4.1	[14]
1980.5	0.00	0.13	0	6.0	0.00	0.08	4.6	1.5	[15]
1981.4	0.04	0.00	0	1.9	0.96	0.09	1.6	1.6	[16]
1991.5	0.04	0.10	0	7.2	0.11	0.08	4.8	2.1	[17]
1994.5	0.12	0.09	0	10.0	0.45	0.07	7.4	5.0	[20]
1995.5	0.08	0.15	0	9.5	0.19	0.08	7.8	3.8	[20]
1996.3	0.13	0.05	0	8.3	0.63	0.09	6.5	5.2	This paper
1997.4	0.13	0.12	0	11.7	0.39	0.07	8.6	5.5	This paper

Fig. 3. Degree of polarization P and position angle θ in the U band as a function of phase of the rotational brightness modulation.

It is argued in [1, 24] that the zonal model is most preferred, since it fits well the observed solar spottedness pattern—namely, localization of the spots at low latitudes and an absence of large circumpolar spots—for all the BY Dra-type stars studied.

3.2. Polarimetry

Here, we will consider only a magnetic mechanism for the polarization. The MS Ser system is rather loosely bound and has no gaseous envelope; therefore, we can neglect the affect of its binarity on the polarization. Magnetic polarization has been modeled in a number of studies [27–30]; the degree of polarization is assumed to depend linearly on the size of the magnetized region. However, Huovelin and Saar [21, 31] showed that this dependence is nonlinear when the region is large. They also showed that the polarization in dwarf stars primarily results from the magnetic mechanism and found a nonlinear dependence of the degree of polarization on the size of the active region.

In particular, for a single, round region, the degree of linear polarization will be proportional to the factor A, which approximately depends on the area of the region as

$$A(S) = -2.128 \times 10^{-4} + 1.076S - 4.812S^2 + 9.058S^3 - 6.26S^4. \quad (9)$$

Huovelin and Saar [21, 31] also calculated a grid of expected degrees of polarization in the $UBVRI$ bands for stars with temperatures from 4000 to 5000 K and $\log g$ from 2.0 to 4.5. We have used their results to estimate the parameters of the magnetized regions for MS Ser.

Figure 3 shows the quantity P_s, the mean of all values of the degree of polarization differing from zero by more than 2σ in the $UBVRI$ bands in the 1996 and 1997 observations, together with the maximum possible degree of polarization (achieved when $S = 24\%$) obtained in the calculations of [31] for a K2V star with a characteristic magnetic field of 2.1 kG. For both seasons, the observed polarization in the VRI bands is slightly higher than the theoretical predictions. The B-band degrees of polarization, as well as the U-band values for 1997, agree well with the theoretical value for $S = 24\%$. The 1996 degree of polarization in the U band corresponds to an S of the order of 10% of the stellar surface. Thus, the polarization observations are consistent with our estimates of the area of the spotted regions in 1996–1997 (from 11 to 26% of the stellar surface, depending on the model) but do not allow us to discriminate between different configurations for the spotted regions.

4. CONCLUSION

Our $UBVRI$ photometry of the poorly studied red dwarf star MS Ser has confirmed the existence of BY Dra-type variability associated with cool spots on its
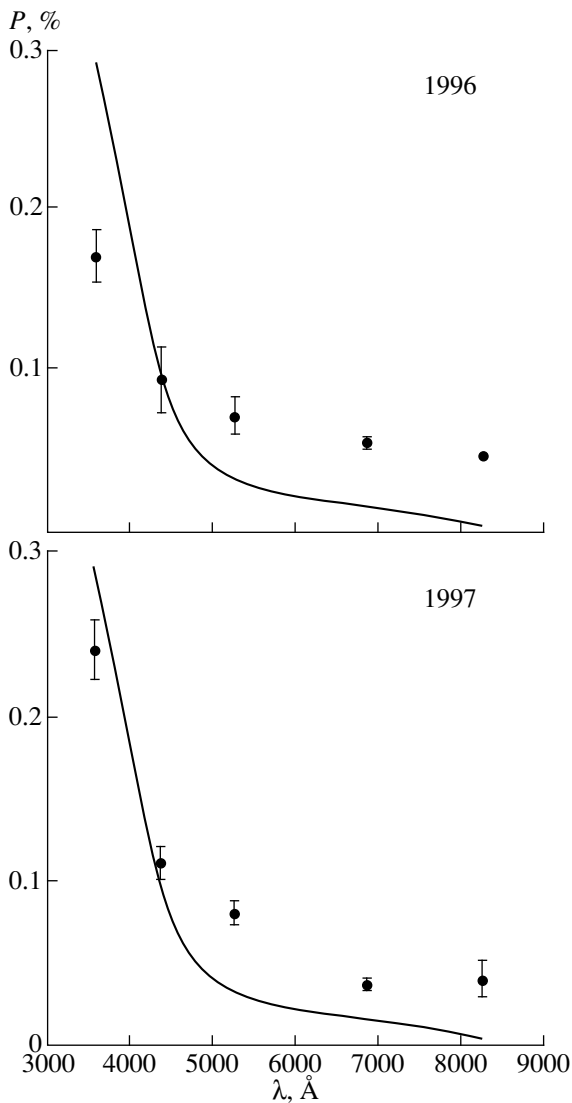
Fig. 4. Wavelength dependence of the degree of polarization. The points show observational estimates of the maximum polarization P_s, and the solid curve shows the expected theoretical dependence.

Fig. 5. Degree of polarization P_s for MS Ser (filled circle) and ten red dwarf stars (open circles) as a function of $B–V$ and Rossby number.

Using all available photometric data for MS Ser, we have modeled its spottedness under various assumptions about the spot geometry: a zonal model, round-spot model, and model without limb-darkening. Depending on the model, the spots are cooler than the surrounding photosphere by 1500, 2200, and 2000 K, and their total area may be as large as 15, 26, and 21% of the stellar surface. Based on the inferred similarity to the solar spottedness pattern, we consider the zonal model to be preferable. A comparison of the polarization observations with calculations of the linear polarization expected for a K2V star [31] yields results that are consistent with the photometric analysis.

surface (rotational modulation of the brightness with an amplitude of up to $0\overset{m}{.}15$ and variations of its mean value up to $0\overset{m}{.}13$). Simultaneously, we confidently detected rotational modulation of the linear polarization of the star's *U*-band brightness in 1997, presumably resulting from the magnetic field associated with the spotted regions. We have compared our estimate of the maximum degree of polarization, $P_s = 0.24 \pm 0.02\%$, with observations for ten red dwarf stars carried out using the same equipment and with a similar procedure by Huovelin *et al.* [10]. Our result for MS Ser agrees well with the dependences of the degree of polarization on spectral type (or *B–V* color index) and Rossby number (Fig. 4) found in [10].
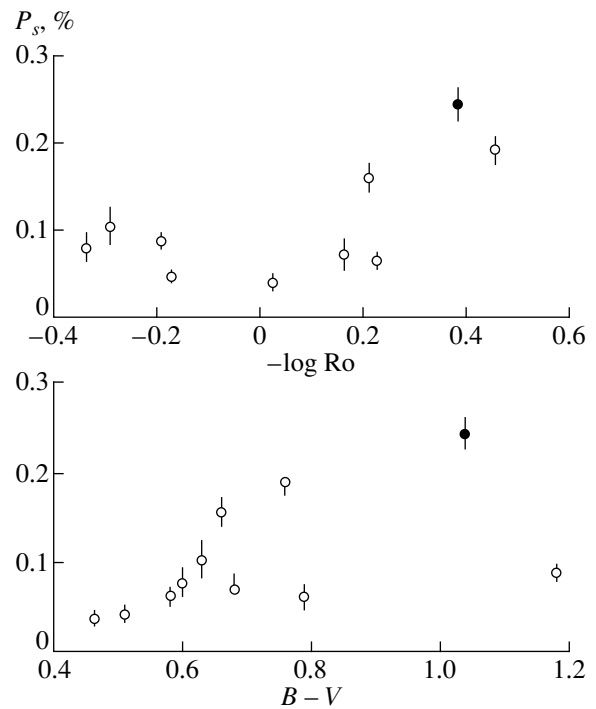
REFERENCES

1. I. Yu. Alekseev and R. E. Gershberg, Astron. Zh. **73**, 589 (1996).

2. A. Dollfus, Compt. Rend. **246**, 3590 (1958).

3. J. L. Leroy, Ann. Astrophys. **25**, 127 (1962).

4. V. Piirola, Astron. Astrophys., Suppl. Ser. **30**, 213 (1977).

5. J. Tinbergen and C. Zwaan, Astron. Astrophys. **101**, 223 (1981).

6. R. H. Koch and R. J. Pfeiffer, Astrophys. J. Lett. **204**, L47 (1976).

7. B. R. Pettersen and J. Hsu, Astrophys. J. **247**, 1013 (1981).

8. C. De Jager, J. Heise, S. Avgoloupis, *et al.*, Astron. Astrophys. **156**, 95 (1986).

9. Ju. Huovelin, S. Linnaluoto, V. Piirola, *et al.*, Astron. Astrophys. **152**, 357 (1985).

10. Ju. Huovelin, S. H. Saar, and I. Tuominen, Astrophys. J. **329**, 882 (1988).

11. Ju. Huovelin, S. Linnaluoto, I. Tuominen, I., *et al.*, Astron. Astrophys., Suppl. Ser. **78**, 129 (1989).

12. R. F. Griffin, Observatory **98**, 257 (1978).

13. O. J. Eggen, Astron. J. **69**, 570 (1964).

14. S. M. Rucinski, Acta Astron. **31**, 363 (1981).

15. B. W. Bopp, P. V. Noah, A. Klimke, *et al.*, Astrophys. J. **249**, 210 (1981).

16. B. W. Bopp, J. L. Africano, P. E. Stencel, *et al.*, Astrophys. J. **275**, 691 (1983).

17. I. Yu. Alekseev and N. I. Shakhovskaya, Izv. Krym. Astrofiz. Obs. **89**, 93 (1995).

18. V. Piirola, Observ. Astrophys. Lab. Rep. No. 6 (Univ. Helsinki, 1984), p. 151.

19. G. Rossello, R. Calafat, F. Figueras, *et al.*, Astron. Astrophys., Suppl. Ser. **59**, 399 (1985).

20. I. Yu. Alekseev and R. E. Gershberg, Astrofizika **39**, 67 (1996).

21. Ju. Huovelin and S. H. Saar, Astrophys. J. **374**, 319 (1991).

22. J. D. Dorren, Astrophys. J. **320**, 756 (1987).

23. I. Yu. Alekseev and R. E. Gershberg, Astron. Zh. **73**, 579 (1996).

24. I. Yu. Alekseev and R. E. Gershberg, Astron. Zh. **74**, 240 (1997).

25. H. L. Johnson, Ann. Rev. Astron. Astrophys. **4**, 193 (1966).

26. E. Budding, Astrophys. Space Sci. **48**, 207 (1977).

27. M. Landi Degl'Innocenti, Astron. Astrophys. **110**, 25 (1982).

28. G. Calamai and E. Landi Degl'Innocenti, Astron. Astrophys., Suppl. Ser. **53**, 311 (1983).

29. D. J. Mullan and R. A. Bell, Astrophys. J. **204**, 818 (1976).

30. M. Landi Degl'Innocenti, G. Calamai, E. Landi Degl'Innocenti, *et al.*, Astrophys. J. **249**, 228 (1981).

31. S. H. Saar and Ju. Huovelin, Astrophys. J. **404**, 739 (1993).

Translated by G. Rudnitskiǐ

Hydrodynamical Models for W Vir Pulsating Variables

Yu. A. Fadeev

Institute of Astronomy, Russian Academy of Sciences,
ul. Pyatnitskaya 48, Moscow, 109017 Russia
Received February 25, 1999

Abstract—We have calculated a grid of hydrodynamical models for W Vir pulsating variable stars with mass $M = 0.6M_\odot$ and bolometric luminosity $200 \leq L_{\mathrm{bol}}/L_\odot \leq 1.2 \times 10^3$. The positions of the blue edge of the instability strip and the boundary separating the domains of periodic and semi-regular pulsation in the H–R diagram were determined. These two boundaries converge for $L_{\mathrm{bol}} \approx 10^3 L_\odot$. Two different groups of models can be distinguished in the region of periodic solutions, characterized by oscillations with alternating amplitude and duration of the pulsation cycle. For the first group of models, the alternation of the pulsations occurs over a time interval of two periods of the fundamental mode; this is due to the $2\Pi_0 = 3\Pi_1$ resonance between the fundamental mode and first overtone. The models of the second group have larger luminosities and are located near the boundary separating the domains of periodic and semiregular pulsations. A discrete Fourier transformation analysis shows that, as we approach the region of semiregular pulsations, additional peaks appear in the spectra of the oscillatory moment of inertia and kinetic energy. These peaks correspond to period doubling bifurcations (a Feigenbaum sequence) of order $n \leq 4$. Approximate formulas are presented for the pulsation constant Q as a function of the mass-to-radius ratio $(M/M_\odot)/(R/R_\odot)$ and the luminosity of the star L_{bol}. © 2000 MAIK "Nauka/Interperiodica".

1. INTRODUCTION

W Vir pulsating variables are a group of long-period Population II Cepheids with periods for their brightness variations from 8–30 days. From the standpoint of stellar evolution theory, W Vir stars with masses $M \approx 0.6M_\odot$ are evolving along the asymptotic giant branch. Thermonuclear burning in a double layer source surrounding the carbon-oxygen core produces thermal instabilities, which result in the contraction of the star, with subsequent expansion accompanied by slight variations of its luminosity. As a result, the evolutionary track of the star in the H–R diagram forms loops that intersect the pulsation instability strip. W Vir pulsating variables are associated precisely with this evolutionary phase [1–4].

The appreciable role of Population-II Cepheids in various astrophysical applications is due to the fact that, like classical Cepheids, these pulsating variables follow a period–luminosity relation and, consequently, can be used to derive distances to globular clusters. Moreover, analyses of the pulsations of Population-II Cepheids is of considerable interest for verifying calculations of stellar evolution along the asymptotic giant branch. Due to the smaller gravitational acceleration and simultaneously larger amplitude of the radial shift compared to that of classical Cepheids, the pulsations of W Vir stars are followed by mass loss via periodic shock waves that propagate in the atmosphere of the pulsating star. These shock waves are indicated by the presence of hydrogen emission lines in the stellar spectra and also by splitting of hydrogen and metal absorption lines (see, for example, [5, 6]). Another piece of observational evidence for matter outflow is the presence of excess infrared radiation, which indicates the formation

of dust particles in the outer layers of the atmospheres of some W Vir variables [7, 8].

Unlike classical Cepheids with relatively small surface pulsation amplitudes ($\Delta R/R \lesssim 0.1$), the radial shift in Population-II Cepheids increases with luminosity, up to $\Delta R/R \sim 1$ for $L_{\mathrm{bol}} > 10^3 L_\odot$. Therefore, as a rule, linear approximations are inadequate for analyses of the pulsations of W Vir stars, and a system of radiative hydrodynamics equations must be solved (see, for example, [9, 10]). A few calculation results for W Vir star pulsations are presented in [11–16]. All these calculations are based on data from the Los Alamos opacity library [17], which, as later became clear [18, 19], do not take into account many sources of absorption. Until very recently, there have been no studies of nonlinear pulsations of W Vir stars using new opacity tables; to help fill this gap, we have made hydrodynamical calculations for models of W Vir variables with luminosities $200L_\odot \leq L_{\mathrm{bol}} \leq 1200L_\odot$. Our new results extend our previously calculated grid of hydrodynamical models for BL Her stars [20] (short-period Population-II Cepheids) toward higher luminosities.

2. CALCULATION RESULTS

In our hydrodynamical calculations of radial stellar pulsations, we assumed radiative energy transfer in the envelope of the star without taking convective heat exchange into account. As in [20], the equation of state and opacity were calculated for relative mass abundances of hydrogen and helium $X = 0.7$ and $Y = 0.299$. The heavy-element content corresponds to a Grevesse-91 mixture [21]. We determined the Rosseland mean opacity by interpolating over tables calculated for the given
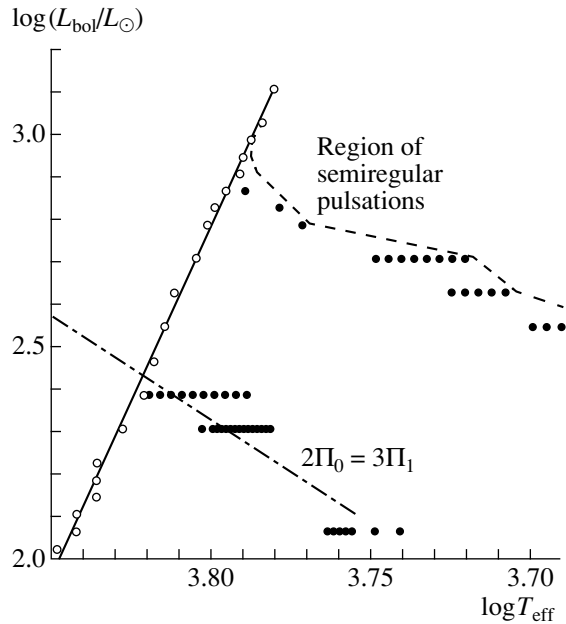
Fig. 1. Hydrodynamical models for Population-II Cepheids in the H–R diagram. The solid line shows a linear approximation for individual T_{eff} estimates (empty circles) at the boundary of the instability strip. The dashed line marks the boundary of the domain for strictly periodic pulsations, and the dash–dot line indicates the center of the $2\Pi_0 = 3\Pi_0$ resonance. The filled circles mark models with alternating pulsations.

chemical composition by A. E. Linas-Gray (private communication) in the framework of the OP Project [19].

We examined the pulsation instability of a star, considering self-excited radial oscillations that develop from the state of thermal and hydrostatic equilibrium. As the initial hydrodynamical perturbation, we used a velocity distribution U that decreased toward the center of the star proportional to the amplitude of the eigenfunction of the fundamental mode and was $U = -3$ km/s at the surface of the star. Therefore, in the case of pulsation instability, integration of the hydrodynamics equations displayed an exponential increase of the pulsation amplitude in the initial time interval, followed by the establishment of self-excited oscillations of the limiting cycle. The duration of the stage of exponential increase of the instability is determined by the envelope structure of the star and ranges from several dozen to several hundred cycles for the models considered.

We restricted our consideration to hydrodynamical models with good repeatability of the pulsation motions ($\delta\Pi/\Pi < 10^{-3}$). Therefore, for models where the limiting-cycle stage was reached, we calculated the Fourier coefficients for the main gas dynamical variables (velocity U, radial coordinate r, luminosity L_r, gas density ρ, total pressure P, and temperature T) in all Lagrange zones $1 \le j \le N$. The total number of Lagrange intervals was $100 \le N \le 300$, depending on the luminos-

ity of the star. We determined the Fourier coefficients for harmonics of order $k \le 15$. The technique for calculating the Fourier coefficients is described in [22].

If a star appeared to be stable to radial pulsations, integration of the hydrodynamics equations displayed an exponential decrease of the oscillation amplitude as a function of time t. For both stable and unstable stellar models, we determined the quantity $\eta = \Pi d\ln E_K/dt$, which describes the rate of attenuation ($\eta < 0$) or of the increase ($\eta > 0$) of the kinetic energy E_K of the stellar envelope. The effective temperature at the boundary of the instability strip ($\eta = 0$) was determined by interpolating between η values for models with the same luminosity L_{bol}. We derived the dependence of the effective temperature of the instability-strip boundary on the bolometric luminosity using the models for W Vir stars considered here and the models for BL Her variables considered previously in [20]. This dependence can be described by the expression

$$\log(L_{\mathrm{bol}}/L_\odot) = 64.977 - 16.368\log T_{\mathrm{eff}},$$
$$(10^2 \le L_{\mathrm{bol}}/L_\odot \le 1.2 \times 10^3). \tag{1}$$

In the H–R diagram, hydrodynamical models that are unstable to pulsations are located to the right of the boundary (1), marked in Fig. 1 by the solid line. Although most models considered here are characterized by good repeatability of the pulsations, a transition from regular to semiregular pulsations occurs as the effective temperature T_{eff} decreases for models with constant luminosity L_{bol}. The effective temperature corresponding to this transition increases with the luminosity of the star, so that the boundary separating the domains of periodic and semiregular pulsations intersects the boundary of the instability strip at a luminosity $L_{\mathrm{bol}} \approx 10^3 L_\odot$. In Fig. 1, the boundary of the domain of periodic solutions is shown by the dashed line.

Within the domain of periodic solutions, we can distinguish two distinct groups of models whose pulsation motions are periodic over a time interval of two or more fundamental-mode periods. In Fig. 1, these models are marked by the filled circles. The first group of models is concentrated in the lower part of the H–R diagram, along the line where the ratio of the fundamental mode period and the first overtone has the value $\Pi_0/\Pi_1 = 2/3$. (Note that the models presented in Fig. 1 with $\log L_{\mathrm{bol}} = 2.068$ are taken from [20]). The main feature of these hydrodynamical models is that the pulsation motions are characterized by alternation of the pulsation amplitude and of the pulsation cycle duration over a time interval $2\Pi_0$. The amplitude of the pulsation

alternation is $\delta\Pi/\Pi = |\Pi_a - \Pi_b|/\left(\frac{1}{2}(\Pi_a + \Pi_b)\right)$, where

Π_a and Π_b are the durations of the two alternating cycles; it reaches a maximum near the point corresponding to the resonance $\Pi_0/\Pi_1 = 2/3$ and decreases on both sides of the resonance point. The resonance

nature of the alternating pulsations also follows from an expansion of the main hydrodynamical variables in a Fourier series over the interval $2\Pi_0$. In particular, the normalized amplitudes of the $k = 2$ and $k = 3$ Fourier harmonics coincide with the radial eigenfunctions for the fundamental mode and first overtone [20]. Figure 2 presents typical curves for the hydrodynamical velocity U and bolometric luminosity L_{bol} in the model with pulsation alternation due to the $\Pi_0/\Pi_1 = 2/3$ resonance.

The second group of models with alternating pulsations is concentrated along the boundary separating the domains of periodic and semiregular pulsations. As we approach this boundary, the oscillations become less regular. Therefore, we analyzed the models using discrete Fourier transformations of the radius $r_j(t)$ and velocity $U_j(t)$ for all Lagrange zones $1 \leq j \leq N$ in time intervals ranging from several hundred to $\sim 10^3$ cycles of the fundamental mode. Figure 3 plots the spectral density of the oscillatory moment of inertia for several hydrodynamical models with bolometric luminosity $L_{bol} = 510 L_\odot$

$$J(\nu) = \int_0^M \mathcal{R}^2(m, \nu) dm, \qquad (2)$$

where

$$\mathcal{R}(m, \nu) = \int_{-\infty}^{\infty} r(m, t) e^{2\pi i \nu t} dt \qquad (3)$$

is the Fourier transformation of the radius $r(m, t)$ of the Lagrange layer with mass coordinate m.

Models with $L_{bol} = 510 L_\odot$ and $T_{eff} \geq 5650$ are characterized by good pulsation repeatability ($\delta\Pi/\Pi < 2 \times 10^{-4}$). Therefore, the largest fraction of the energy of pulsation motions is concentrated in Fourier harmonics with frequency $\nu = k\nu_0$, where $\nu_0 = 1/\Pi_0$ and $k = 1, 2, 3, \ldots$. Moreover, for $\nu = k\nu_0$, the real and imaginary parts of $\mathcal{R}(m, \nu)$ coincide with the kth-order Fourier coefficients: $\mathrm{Re}\,\mathcal{R}(\nu) = B_{rk}$, $\mathrm{Im}\,\mathcal{R}(\nu) = A_{rk}$. Figure 3 presents a typical spectrum of the periodic pulsations $J(\nu)$ for the model with effective temperature $T_{eff} = 5650$ K.

The transition from periodic to alternating pulsations occurs when variations of the effective temperature are smaller than 50 K. For example, for $T_{eff} = 5600$ K, the amplitude of the radial shift at the surface and the duration of the pulsation cycle vary from cycle to cycle by $|\Delta R_a - \Delta R_b|/\left(\frac{1}{2}(\Delta R_a + \Delta R_b)\right) = 0.17$ and $|\Pi_a - \Pi_b|/\left(\frac{1}{2}(\Pi_a + \Pi_b)\right) = 0.04$. (Here, the indexes a and b denote values corresponding to the first and second cycle, respectively). Note that the alternating pulsations display good repeatability ($\delta\Pi/\Pi < 1 \times 10^{-3}$), however, only for a time interval equal to two fundamental-mode periods. In the spectrum of the oscillatory moment of
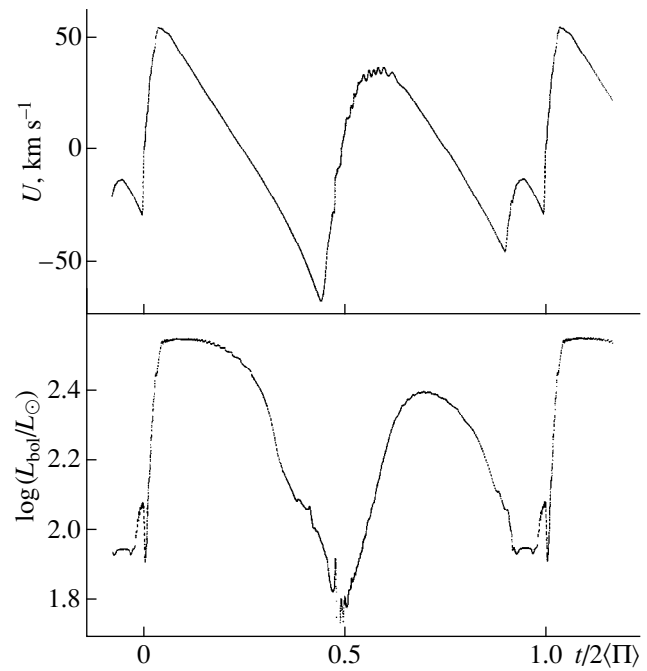
Fig. 2. Hydrodynamical velocity of the outer envelope layers U and bolometric luminosity L_{bol} as functions of the phase of the doubled average cycle for the hydrodynamical model with periods for alternating pulsations $\Pi_a = 2.780$ and $\Pi_b = 2.885$ days.

inertia, peaks representing Fourier harmonics of the pulsation can clearly be seen at equal distances from the main maxima. Figure 3 presents the spectrum of pulsations alternating over the time interval $2\Pi_0$ for the model with $T_{eff} = 5600$ K. If the effective temperature is further decreased by 20 K, the periodicity condition for the pulsations becomes valid over a time interval $4\Pi_0$, and a new set of peaks appears in the spectrum $J(\nu)$ with frequency interval $\Delta\nu = \nu_0/4$. Such an alternation of pulsations was obtained for $T_{eff} = 5580$ K (Fig. 3). We obtained a more complicated spectrum with a frequency interval for the peaks $\Delta\nu = \nu_0/8$ for the model with effective temperature $T_{eff} = 5560$ K. Note that, for all the hydrodynamical models considered, the spectra of the kinetic energy $E_K(\nu)$ display the same features as the $J(\nu)$ spectra.

Unfortunately, the amplitudes for peaks corresponding to frequency intervals $\Delta\nu = \nu_0/2^n$ for $n > 4$ appear to be too small, and it is difficult to distinguish them in the power spectrum due to the noise associated with the limited accuracy of the calculations. Nonetheless, we can conclude, based on the results presented above, that at least the initial stage in the transition from periodic to semiregular pulsations results from period doubling bifurcations of the self-oscillations and can be represented by a Feigenbaum sequence (see, for example, [23]). The idea of a transition from periodic to semiregular stellar pulsations in the form of a Feigenbaum sequence was formulated for the first time by Buchler
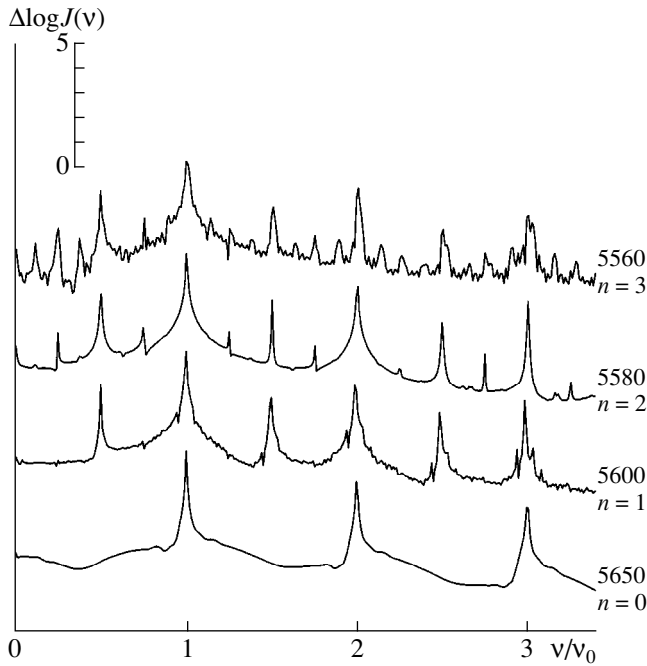
Fig. 3. Spectra of the oscillator moment of inertia $J(\nu)$ for hydrodynamical models $L_{\mathrm{bol}} = 510L_{\odot}$ as a function of the normalized frequency ν/ν_0. The numbers near the curves indicate the effective temperature of the star and the bifurcation order n.

and Kovacs [13, 14]. They drew their conclusions, however, based on analysis of the motion of an individual fixed Lagrange layer in their hydrodynamical model. Here, the sequence of hydrodynamical models in the vicinity of the boundary of the periodic solution domain is studied more correctly, based on a spectral analysis of the oscillator moment of inertia $J(\nu)$ and kinetic energy $E_K(\nu)$, which are integrated values and thus describe oscillations of the stellar envelope as a whole.

The values for the pulsation constant Q are of considerable interest for many astrophysical applications. In general, it depends on the internal constitution of a star, and, for a given chemical composition, is a slowly varying function of the star's mass M, average radius R, and bolometric luminosity L_{bol}. For the hydrodynamical models considered here, for constant luminosity in the function for the mass-to-radius ratio of the star, the pulsation constant can to good accuracy be approximated:

$$Q = a_0 + a_1 f, \qquad (4)$$

where $f = \log[(M/M_{\odot})/(R/R_{\odot})]$. The relative rms error for our approximation of the calculated Q values for $L_{\mathrm{bol}} = \mathrm{const}$ using formula (4) does not exceed 0.5%. To estimate Q for different luminosities, we must take into account the relation between the coefficients a_0 and a_1 and L_{bol}. Unfortunately, a polynomial approximation for a_0 and a_1 ultimately leads to unacceptably large errors in the Q estimates. Therefore, it is more expedient to use (4) and take into account the luminosity dependence by interpolating the resulting Q values in L_{bol}. The coefficients a_0 and a_1 are presented in the table.

3. DISCUSSION

The results of our hydrodynamical calculations presented in [20] and in the present paper form a uniform grid of more than 400 hydrodynamical models for Population-II Cepheids with mass $M = 0.6\,M_{\odot}$ and bolometric luminosities $100 \le L_{\mathrm{bol}}/L_{\odot} \le 10^3$. We have determined upper limits for the luminosity using an approach based on calculating the Fourier coefficients for the main hydrodynamical variables; these values are therefore applicable only for periodic solutions. Approximations obtained in the form of Fourier series make it possible to easily estimate hydrodynamical variables as functions of the pulsation cycle phase and Lagrange mass coordinate without elaborate calculations. Unfortunately, this approach fails for models with higher luminosities, since the oscillations cease to be periodic when $L_{\mathrm{bol}} > 10^3 L_{\odot}$, even in the immediate vicinity of the boundary for pulsation instability.

The consideration of hydrodynamical models for brighter Population-II Cepheids is of considerable interest for gaining insight into the relation of these variables to RV Tau pulsating stars. For pulsation periods from 20 to 30 days, the differences between W Vir and RV Tau variables are often so insignificant that the assignment of a pulsating variable to one of these classes becomes ambiguous (see, for example, the review [24]). Clarification of the relation between these pulsating variables requires detailed investigation of the resonance between the fundamental mode and first overtone $\Pi_1/\Pi_0 = 1/2$. The condition for this resonance assumes that the $k = 2$ Fourier harmonic is an eigenfunction of order $l = 1$ (i.e., the first overtone) and that 3/2 of the pulsation wave of this Fourier harmonic fits in the radius of the star R. As the independent variable, we used the acoustic coordinate $\tau(r)$, equal to the time for propagation of an acoustic wave from the center of

Approximation coefficients in formula (4)

$\log L_{\mathrm{bol}}$	a_0	a_1
2.308	0.003879	−0.03219
2.548	−0.103018	−0.10378
2.628	−0.101033	−0.10182
2.708	−0.127588	−0.11761
2.788	−0.117687	−0.10883
2.828	−0.384925	−0.27744
2.868	−0.465786	−0.32551

the star to the layer with radius r and measured in units of the pulsation period Π:

$$\tau(r) = \frac{1}{\Pi}\int_0^r \frac{dr'}{a}. \tag{5}$$

Here, a is the adiabatic sound speed. For the models for Population-II Cepheids considered, the acoustic coordinate at the stellar surface $\tau(R)$ decreases as the luminosity increases as

$$\tau(R) = 1.835 - 0.457\log L_{bol}, \tag{6}$$

whereas the acoustic interval for each Fourier harmonic, measured as the difference of the acoustic coordinates for two adjacent nodes, is constant and does not depend on the pulsation period Π. As for classical Cepheids [22], the acoustic interval for the second-order Fourier harmonic is $\Delta\tau_2 = 0.3$, so that the resonance condition $\Pi_1/\Pi_0 = 1/2$ will hold for $\tau(R) = 0.45$, i.e., for luminosities $L_{bol} \approx 1.1 \times 10^3 L_\odot$.

Thus, a resonance between the fundamental mode and first overtone occurs in Population-II Cepheids in the absence of strict periodicity of the pulsation motions, so that analysis of this resonance requires use of the discrete Fourier transformation to solve the hydrodynamics equations over sufficiently long time intervals. For Population-II Cepheids, this analysis is complicated by the fact that the transition from periodic to semiregular oscillations is accompanied by an appreciable increase of the role of the shock waves that arise in the presence of nonlinear pulsations. In particular, even though the velocity of the gas motion behind the shock is smaller than the local escape velocity, the average radius for each Lagrange layer in the stellar atmosphere gradually increases, since the time for it to return due to gravity exceeds the pulsation period. This mass-loss model was considered analytically in an isothermal approach in [25] and later confirmed using hydrodynamical calculations applied to W Vir stars [16]. Thus, the considerable difficulties in analyses of semiregular pulsations are primarily due to the fact that, for calculations over time intervals up to 10^3 pulsation cycles, the outermost layers of the Lagrange grid become so remote that they not only substantially increase the error in approximating the differential grid but also impede convergence of the Newton–Raphson iteration scheme used to solve the energy conservation equation.

Results for a discrete Fourier analysis for hydrodynamical models of Population-II Cepheids with luminosities $L_{bol} > 10^3 L_\odot$ will be presented in a future paper.

REFERENCES

1. M. Schwarzchild and R. Härm, Astrophys. J. **160**, 341 (1970).
2. R. A. Gingold, Astrophys. J. **193**, 177 (1974).
3. R. A. Gingold, Astrophys. J. **198**, 425 (1975).
4. R. A. Gingold, Astrophys. J. **204**, 116 (1976).
5. H. A. Abt, Astrophys. J., Suppl. Ser. **1**, 63 (1954).
6. G. Wallerstein, Astrophys. J. **130**, 560 (1959).
7. R. D. Gehrz and J. A. Hackwell, Astrophys. J. **193**, 385 (1974).
8. T. Lloyd Evans, Mon. Not. R. Astron. Soc. **217**, 493 (1985).
9. R. F. Christy, Methods Comput. Phys. **7**, 191 (1967).
10. Yu. A. Fadeev, Nauchn. Inform. Astron. Soveta Akad. Nauk SSSR **52**, 3 (1983).
11. R. F. Christy, Astrophys. J. **145**, 337 (1966).
12. Yu. A. Fadeyev and A. B. Fokin, Astrophys. Space Sci. **111**, 355 (1985).
13. J. R. Buchler and G. Kovács, Astrophys. J. Lett. **320**, L57 (1987).
14. G. Kovács and J. R. Buchler, Astrophys. J. **334**, 971 (1988).
15. P. Moskalik and J. R. Buchler, Astrophys. J. **355**, 590 (1990).
16. Yu. A. Fadeyev and H. Muthsam, Astron. Astrophys. **234**, 188 (1990).
17. W. F. Hübner, A. L. Merts, N. H. Magee, *et al.*, Los Alamos Report LA-6760-M (1977).
18. C. A. Iglesias, F. J. Rogers, and B. G. Wilson, Astrophys. J. **397**, 717 (1992).
19. M. J. Seaton, Yu Yan, D. Mihalas, *et al.*, Mon. Not. R. Astron. Soc. **266**, 805 (1994).
20. Yu. A. Fadeev, Astron. Zh. **74**, 720 (1997).
21. E. Anders and N. Grevesse, Geochim. Cosmochim. Acta **53**, 197 (1989).
22. Yu. A. Fadeev, Astrophys. Space Sci. **213**, 75 (1993).
23. H. Haken, *Synergetics: An Introduction* (Springer, Berlin, 1977; Mir, Moscow, 1983).
24. G. Wallerstein and A. N. Cox, Publ. Astron. Soc. Pacif. **96**, 677 (1984).
25. L. A. Willson and S. J. Hill, Astrophys. J. **228**, 854 (1979).

Translated by K. Maslennikov

Photometric and Spectrophotometric Observations of the Evolution of a Strong Outburst of the Classical Symbiotic Star YY Herculis

A. A. Tatarnikova[1], M. Rejkuba[2], L. M. Buson[2], E. A. Kolotilov[1], U. Munari[2], and B. F. Yudin[1]

*[1] Sternberg Astronomical Institute,
Universitetskiĭ pr. 13, Moscow, 119899 Russia*
[2] Padua Astronomical Observatory (Asiago Station), Italy
Received December 30, 1998

Abstract—We present spectrophotometric (3400–7500 Å) observations of the evolution of a strong outburst of the classical symbiotic star YY Her in 1993 and photoelectric *UBV* observations of the star's eclipse in 1997. The duration of the phase of lowest brightness, when the *U* brightness had decreased by ~1.3^m, was ~$0.17P_{orb}$ (P_{orb} is the orbital period). If this phase is due to the total eclipse of ~70% of the radiation of the circumstellar envelope, this duration implies that the cool component of YY Her fills its Roche lobe, the bulk of the envelope's volume emission measure is concentrated around the hot component in a region with rather sharp boundaries $r \ll R_{giant}$ (R_{giant} is the giant's radius), and the line of sight is close to the binary orbital plane. We model fit the spectral energy distribution of YY Her to obtain estimates of the parameters of several structural components of the system. The red giant's spectral type correlates with its visual brightness and does not correlate with the hot component's brightness. At minimum brightness, the hot component's luminosity fluctuates about that of its cool companion ($L_{h, bol}/L_{c, bol} \approx 0.9$), and its temperature is $T_h \approx (9–11) \times 10^4$ K. Activity of the hot component of YY Her is accompanied by increased brightness and reduced temperature ($L_{h, bol} \propto T_h^{-5}$), though the relation between these parameters is not unique. At maximum brightness, $L_{h, bol}/L_{c, bol} \approx 10$ and $T_h \approx 6.0 \times 10^4$ K. If the red giant fills its Roche lobe, the hot component's luminosity is ~$3.3 \times 10^4 L_\odot$. The active period of YY Her lasted about 5 years, and the activity decrease was not monotonic. © *2000 MAIK "Nauka/Interperiodica".*

1. INTRODUCTION

YY Her is a classical symbiotic star; the prototype of the class is Z And. This type of symbiotic star is characterized by special novalike outbursts with the following characteristics. The brightness increase occurs within one to three months, while the decrease lasts from one to three years. Strong outbursts recur at intervals of several decades. The strongest outbursts have *U* amplitudes reaching 3^m. Some symbiotic stars show dramatic spectral changes during major outbursts. Their high-excitation emission spectra become much fainter or even disappear completely. In this latter case, the star begins to resemble a B–F supergiant [1, 2].

Munari *et al.* [3] studied the photographic and visual light curves of YY Her for the entire period covered by photometric observations since 1890. These light curves reveal four novalike outbursts of the sort characteristic of Z And stars; a periodic component with $P = 590$ days and an amplitude of $\leq 0.3^m$ were detected in the visual measurements. Studies of classical symbiotic stars for which both light curves and radial-velocity curves have been constructed indicate that periodic brightness variations are due to the orbital motion of the binary system. The minimum brightness occurs when the red giant is in lower conjunction, i.e., when it is in front of the hot component. On these grounds, it was concluded that the orbital period of YY Her is 590 days [3].

Munari *et al.* [4] present UV spectra of YY Her in a subsequent paper. Three of the spectra were taken during the star's quiescent state and one was taken at the beginning of a strong outburst in 1993. Two of the UV spectra were supplemented with optical spectra. These indicated that the hot component of YY Her, which ionizes the circumstellar envelope and contributes appreciably to the star's UV spectral continuum, cannot always be represented as a spherically symmetrical radiation source similar to the hot components of symbiotic novae. Sometimes, a "warm" (~1.5×10^4 K) nonspherical radiation source (possibly an accretion disk) adds to the radiation of the hot (~10^5 K) subdwarf, appreciably influencing the shape of the energy distribution towards long UV wavelengths. This source's appearance and relative intensity are not uniquely related to the star's bolometric brightness.
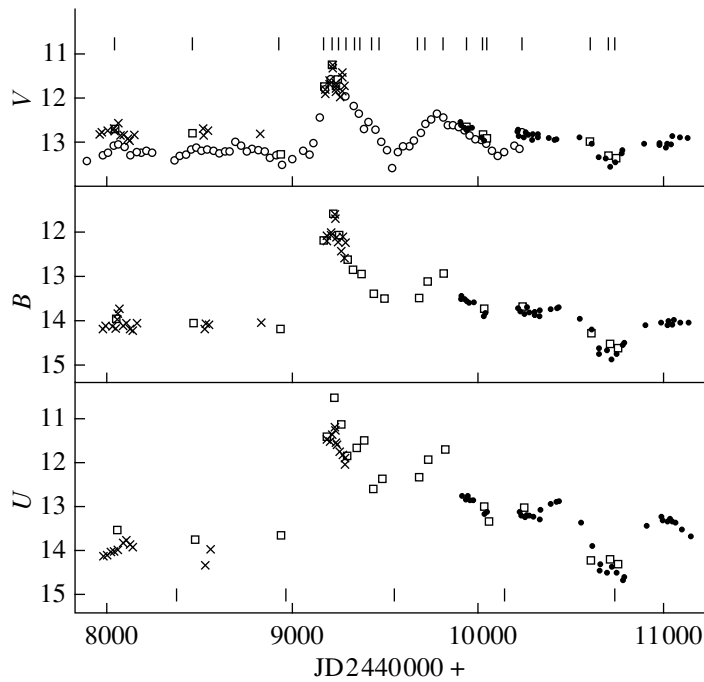
Fig. 1. Light curves of YY Her in the *U*, *B*, and *V* bands. Open circles and crosses are, respectively, visual and photoelectric brightness estimates from Munari *et al.* [3]; filled circles show data from the present paper. Open squares are brightness estimates obtained by convolving the spectra with the transmission curves of the corresponding filters. The vertical ticks near the horizontal axis (bottom) indicate the dates of minima in the visual light curve calculated using the ephemeris from [3]. For the visual light curve, the vertical ticks indicate dates of spectrophotometric observations.

The current paper continues the studies of Munari *et al.* [3, 4] and presents a detailed investigation of the evolution of the strong outburst of YY Her that started in 1993 and, also, of the most recent photometric minimum in 1997. The origins of the outbursts of classical symbiotic stars are still being actively discussed (see [4] and references therein). Elucidation of this question requires following the evolution of outbursts of a star in the temperature–luminosity diagram together with changes of its other physical characteristics. We have done this for YY Her using spectra taken in 1990–1997. The shape of the periodic component of the light curve reflects the main parameters of the symbiotic binary system. We present for the first time photoelectric *UBV* observations for a complete period of the brightness variations of YY Her. Earlier, fairly accurate observations were available only at visual wavelengths, where the contribution of the red giant to the total radiation of the symbiotic star is already large.

2. OBSERVATIONS

We carried out photometric *UBV* observations of YY Her using the 0.6-m telescope of the Crimean Laboratory of the Sternberg Astronomical Institute. HD 168957 was used as a comparison star: $U = 6.35$, $B = 6.91$, $V = 7.01$. The results of our observations are collected in Table 1. The measurement errors do not exceed $0\overset{m}{.}03$. Figure 1 shows the *UBV* light curves of YY Her, including the data already published in [3].

The spectrophotometric observations of YY Her at 3400–7500 Å were carried out using the 1.8-m telescope of the Padua Observatory in Asiago (Italy). The spectrophotometer is equipped with a CCD array and has a dispersion ~8 Å/pixel. Table 2 presents emission-line fluxes determined by fitting Gaussians to the line profiles. The errors in the fluxes do not exceed 25% for the weakest lines and are primarily due to the complicated shape of the continuum. The Hα line was usually saturated and so is not included in Table 2. All spectra in subsequent figures were dereddened using the color excess $E(B - V) = 0.2$ [4]. The original spectra can be found at http://infra.sai.msu.su/observations.html.

Table 2 also contains *U* magnitudes for YY Her determined by convolving its spectra with the *U* filter transmission curve. Even at minimum brightness of the hot radiation source (hot component + ionized envelope), the contribution of the red giant does not exceed 20%. Thus, the *U* magnitudes characterize the brightness of the hot source. In addition, Table 2 presents equivalent widths of the He II λ4686 (W(He II)) and Hβ, (W(Hβ)) lines, computed relative to the radiation flux near 3600 Å (F(3600)), i.e., below the Balmer jump. These are important parameters describing the physical

Table 1. Results of photometric *UBV*- observations of YY Her

JD 2 440 000+	U	B	V	JD 2 440 000+	U	B	V
4029	14.26	14.01	12.66	10304	13.11	13.80	12.84
5124	13.71	13.98	12.84	10362	12.96	13.77	12.91
5513	13.64	13.70	12.96	10395	12.92	13.75	12.95
9886	12.78	13.57	12.61	10403	12.92	13.75	12.93
9887	12.67	13.39	12.55	10521	13.40	13.99	12.89
9903	12.87	13.54	12.67	10584	13.94	14.24	13.02
9917	12.79	13.61	12.71	10624	14.34	14.79	13.35
9921	12.81	13.57	12.67	10625	14.47	14.68	13.36
9924	12.88	13.57	12.69	10667	14.50	14.69	13.35
9944	12.89	13.63	12.67	10690	14.40	14.90	13.55
10005	13.20	13.93	12.92	10714	14.51	14.78	13.45
10015	13.16	13.87	12.96	10748	14.67	14.58	13.27
10194	13.16	13.79	12.77	10754	14.60	14.53	13.20
10199	13.25	13.82	12.85	10874	13.48	14.14	13.02
10200	13.20	13.76	12.73	10957	13.28	14.08	13.01
10222	13.25	13.89	12.88	10958	13.34	14.08	13.04
10224	13.28	13.86	12.84	10988	13.36	14.13	13.14
10233	13.23	13.73	12.76	10998	13.31	14.03	13.04
10245	13.25	13.85	12.83	11013	13.36	14.11	13.04
10269	13.26	13.84	12.82	11025	13.41	14.02	12.88
10270	13.27	13.88	12.93	11062	13.55	14.07	12.88
10301	13.30	13.93	12.88	11111	13.71	14.07	12.90

conditions of the hot radiation source. Note again that, when discussing parameters of the radiation or structural components of the symbiotic star YY Her, we must distinguish between the hot component and the hot radiation source. We take the latter to be the combination of the hot component and the ionized envelope.

Spectral classification of red giants is based on measurements of the intensities of titanium oxide bands. For this purpose, we used the indices introduced and calibrated for the TiO $\lambda\lambda$ 5448, 5905, 6215, 6717, and 7125 bands by Beshenova and Kharitonov [5]. However, it is evident that, in order to calculate these indices using observations of a symbiotic star, we must isolate the red giant's radiation and separate it out from the radiation of the hot source. This was achieved during the spectral fitting, and the five jumps in the spectral radiation flux at the short-wavelength edges of the TiO bands presented in Table 3 were determined after separating the radiation of YY Her into components. At this stage, we can estimate the red giant's magnitudes, which are obviously most reliable for *V* filter. Table 3 gives these magnitudes along with those of the hot radiation source. Together, they correspond to the total brightness of YY Her. Prior to estimating the spectral type of the cool component, we convolved our spectra

in accordance with the spectra of Beshenova and Kharitonov [5].

Note that earlier estimates of the TiO indices were based directly on observed spectra, and therefore depend on the brightness of the symbiotic star's hot radiation source (see [6, 7] and references therein). In particular, estimates of the red giant's spectral type contained a periodic component reflecting the orbital motion of the binary system, giving the impression that the hot component appreciably heated the upper atmosphere of the red giant. However, correct estimates of the TiO indices must be obtained before such conclusions can be drawn.

3. ANALYSIS

In the *U* light curve (Fig. 1), the vertical ticks indicate the dates of minima of the periodic ($P = 590$ days) component derived for the visual light curve when YY Her was in the quiescent state [3]. Figure 1 shows that the latest calculated date is near the middle of the minimum observed in 1997. More precisely, the minimum occurred ≤ 25 days earlier (O–$C \leq$ –25 days). Since the difference does not exceed $0.05P$, we used the ephemerides from [3] to calculate the brightness phases presented in the tables. By analogy with other classical symbiotic stars, we assume that the date of photometric minimum ($\varphi = 0$) corresponds to the red giant's lower conjunction. It was noted earlier that these two dates coincided fairly accurately when only the quiescent sections of symbiotic light curves are taken into consideration (see [8] and references therein).

Our analysis of the *U* light curve of YY Her reveals a periodic component with $P \approx 590$ days. In particular, the calculated date of the latest minimum would coincide with the observed date for $P = 587$ days and

$$\text{Min}(U) = 2\,448\,919 + 587^{\text{d}}E.$$

With these parameters for the periodic component of YY Her, the tabulated values $\varphi = 1.15$ and 4.15 would become $\varphi = 1.17$ and 4.20; the difference is insignificant for our analysis of the phase dependences of the radiation parameters of YY Her.

Note that, in principle, small-amplitude periodic variations at visual wavelengths could be due to variability of the red giant. For example, in the case of T CrB, they are due to the ellipsoidal shape of the red giant, and therefore have a period that is half the orbital period. However, for YY Her, the contribution of the red giant to the *U* radiation is negligible. Thus, the variations with $P \approx 590$ days can be safely interpreted as resulting from the eclipse of the hot radiation source.

At the same time, since there are reasons to believe that the cool component of YY Her fills its Roche lobe [4], we analyzed the visual light curve of YY Her from [3] to search for a period equal to half the orbital period. This revealed a harmonic with a period of ~283 days and an of amplitude ~$0^{m}_{.}1$. This is not exactly half the

Table 2. Emission-line fluxes and equivalent widths of H_β and He II λ4686*

Date	U	Phase	H I 3968	H I 4101	H I 4340	N III 4645	He II 4686	H I 4861	He I 4922	[OIII] 5007	He I 5876	He I 6678	W_{H_β} 4861	$W_{He II}$ 4686
May 9, 1990	13.45	0.43	–	4.7	6.2	–	3.3	16.7	–	–	5.6	4.6	87.9	17.4
July 2, 1991	13.79	1.15	2.3	1.9	1.3	–	3.3	3.6	–	–	–	–	30.0	27.5
Oct. 8, 1992	13.70	1.93	–	2.3	2.5	–	3.3	5.4	–	–	2.0	0.7	37.0	22.6
June 10, 1993	11.44	2.34	9.4	11.8	13.9	5.7	7.7	29.7	5.9	5.4	7.4	7.1	31.9	8.3
July 26, 1993	10.55	2.42	–	10.2	11.9	4.9	4.2	36.9	7.2	6.2	3.6	6.1	13.0	1.5
Aug. 25, 1993	11.16	2.47	–	10.0	11.4	4.8	4.5	35.6	4.8	4.5	5.4	5.1	21.7	2.7
Oct. 7, 1993	11.87	2.55	–	–	10.1	–	7.2	25.8	4.9	5.0	5.2	5.8	36.3	10.1
Nov. 22, 1993	11.69	2.61	–	7.4	10.6	3.2	8.2	24.1	7.2	–	4.4	6.5	27.7	9.4
Dec. 16, 1993	11.58	2.67	–	–	15.1	–	7.2	21.4	5.9	–	3.9	5.8	21.0	7.1
Feb. 25, 1994	12.61	2.79	1.9	3.5	5.0	–	5.5	15.3	4.0	–	3.7	3.6	41.4	14.9
Apr. 7, 1994	12.40	2.86	2.0	3.3	5.2	1.8	4.7	11.2	–	–	3.2	3.0	25.5	10.7
Oct. 24, 1994	12.34	3.19	2.5	3.7	5.2	–	3.7	9.1	–	–	0.9	2.1	19.0	7.7
Dec. 10, 1994	11.95	3.27	3.3	3.5	5.1	2.5	5.1	11.0	–	–	–	2.6	16.7	7.7
Mar. 11, 1995	11.72	3.43	5.0	6.8	10.3	4.2	7.1	24.0	4.3	3.8	2.8	3.2	28.9	8.6
July 22, 1995	12.81	3.65	3.8	5.6	6.9	–	4.5	12.5	3.2	2.3	2.9	4.2	32.9	11.8
Oct. 14, 1995	13.05	3.80	2.4	2.7	3.9	–	3.5	7.8	–	1.4	1.5	1.8	32.5	14.6
Nov. 2, 1995	13.37	3.83	–	–	5.3	–	3.0	7.0	–	–	–	1.3	38.9	16.7
May 7, 1996	13.07	4.15	1.8	2.3	3.0	–	3.0	6.6	–	1.2	1.1	1.7	26.4	12.0
May 12, 1997	14.25	4.77	–	1.5	3.3	–	3.2	5.7	–	–	–	1.5	66.3	37.2
Aug. 21, 1997	14.23	4.94	–	1.6	1.9	–	3.1	4.3	–	–	2.1	1.1	48.9	35.2
Sep. 26, 1997	14.32	5.00	–	1.1	1.3	–	2.2	2.9	–	–	1.4	1.1	37.2	28.2

* The fluxes and equivalent widths are in 10^{-13} erg cm^{-2} s^{-1} and Å, respectively. The O[III] λ5007 line is blended with the He I λ5015 line; both lines have approximately equal intensities in the quiescent state. For these lines, the table presents a combined flux.

orbital period (295 days), but the two values are fairly close.

It is apparent from Fig. 1 that, during the last eclipse, the U brightness of YY Her was near its minimum level for a long time (~100 days, or ~$0.17P_{orb}$), with ~70% of the radiation from the hot source hidden from the observer. If we explain this effect solely as the result of an eclipse, this would mean that, at this time, a dense, compact, gaseous envelope with rather well-defined boundaries was present around the hot component and that ~70% of the volume emission measure of the entire circumstellar envelope of YY Her was concentrated in this envelope. In this case, the duration of the total eclipse of this compact structure implies that the binary is observed nearly edge-on, with the line of sight close to the orbital plane. In addition, the cool component fills its Roche lobe. Note that gaps in the photoelectric observations of YY Her near the two minima preceding the minimum of 1997 coincide with the duration of the phase of constant minimum brightness (Fig. 1). Thus, we cannot say whether the same phenomenon occurred during those minima.

Table 2 shows that the He II λ4686 line is never absent from the spectrum of YY Her. In particular, it does not disappear at phases close to zero. This is true for states both prior to and following the outburst. Formally, from the first and last three lines of Table 2, which correspond to these states, we might conclude that there is no appreciable dependence of the radiation flux in this line on the phase. However, since this parameter is very sensitive to the hot component's temperature, many more observations of the star in quiescence are required before such a conclusion could be drawn. Nevertheless, models of the star as an eclipsing variable must take into account the constant presence of the He II λ4686 line in the spectrum of YY Her.

Figure 2 presents two color–magnitude diagrams. The $(B - V)$–U diagram shows that B–V becomes independent of the U brightness of YY Her when $U \geq 14^m$. This means that, when the brightness of the hot radiation source reaches this level, it ceases to appreciably influence the star's B brightness and does not influence its V brightness at all. In other words, in this case, the visual brightness of YY Her is completely determined by the red giant. It is apparent from the $(B - V)$–V diagram that, at the maximum B–V, the range of changes of the visual brightness is ~1^m. This coincides with the

Table 3. Dependence of the molecular TiO absorption indices on the visual brightness of the red giant in YY Her*

Date	Phase	V_h	V_g	λ5448	λ5905	λ6215	λ6717	λ7125
May 9, 1990	0.43	14.80	12.88	0.07	0.14	0.21	0.11	0.20
July 2, 1991	1.15	14.15	13.18	0.16	0.20	0.31	0.19	0.32
Oct. 8, 1992	1.93	14.88	13.64	0.20	0.29	0.30	0.18	0.37
June 10, 1993	2.34	12.07	13.22	0.09	0.15	0.15	0.08	0.22
Aug. 25, 1993	2.47	11.87	13.26	0.10	0.20	0.18	0.17	0.29
Oct. 7, 1993	2.55	12.42	13.08	0.05	0.09	0.16	0.13	0.26
Nov. 22, 1993	2.61	12.81	13.26	0.11	0.13	0.27	0.21	0.24
Dec. 16, 1993	2.67	12.89	13.28	0.13	0.20	0.30	0.18	0.27
Feb. 25, 1994	2.79	13.39	13.29	0.15	0.17	0.27	0.19	0.28
Apr. 7, 1994	2.86	13.50	13.87	0.18	0.21	0.29	0.25	0.36
Oct. 24, 1994	3.19	13.36	13.97	0.16	0.25	0.41	0.23	0.37
Dec. 10, 1994	3.27	13.00	13.98	0.18	0.33	0.47	0.25	0.40
Mar. 11, 1995	3.43	12.86	13.78	0.16	0.21	0.29	0.23	0.32
July 22, 1995	3.65	14.19	12.92	0.13	0.16	0.23	0.16	0.30
Oct. 14, 1995	3.80	13.82	13.46	0.15	0.18	0.30	0.20	0.31
Nov. 2, 1995	3.83	14.11	13.36	0.16	0.21	0.30	0.19	0.31
May 7, 1996	4.15	13.58	13.45	0.17	0.22	0.33	0.18	0.33
May 12, 1997	4.77	15.08	13.16	0.13	0.23	0.28	0.15	0.29
Aug. 21, 1997	4.94	14.74	13.66	0.19	0.24	0.33	0.19	0.38
Sep. 26, 1997	5.00	15.08	13.66	0.18	0.19	0.35	0.22	0.36

* V_h and V_g are the magnitudes of the hot radiation source (hot component + ionized envelope) and of the red giant in YY Her.

amplitude of the magnitude changes of the red giant of YY Her in this spectral range.

It is clear from Fig. 3 that the red giant's spectral type estimated from the TiO indices correlates with its brightness in a manner similar to that of single red giants: As the brightness decreases, the spectral type becomes later. In general, the spectral type varies in the range M3.5–M4.5. If we plot the dependence of the
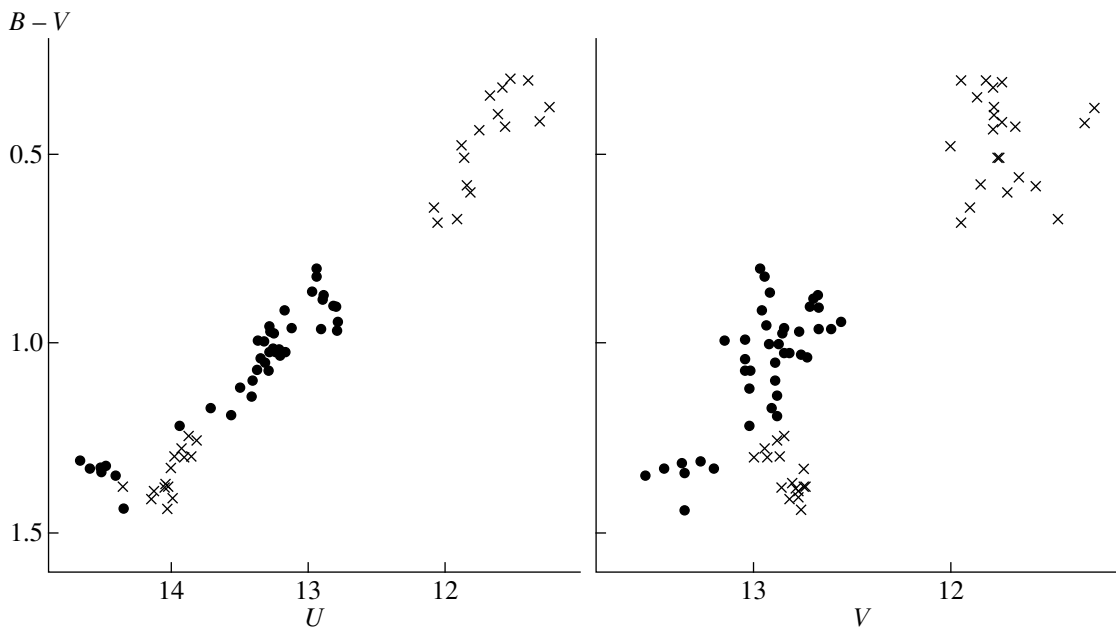

Fig. 2. $(B - V)$–U and $(B - V)$–V diagrams. The crosses are photoelectric brightness estimates of YY Her from [3]; the circles show data from the present paper.
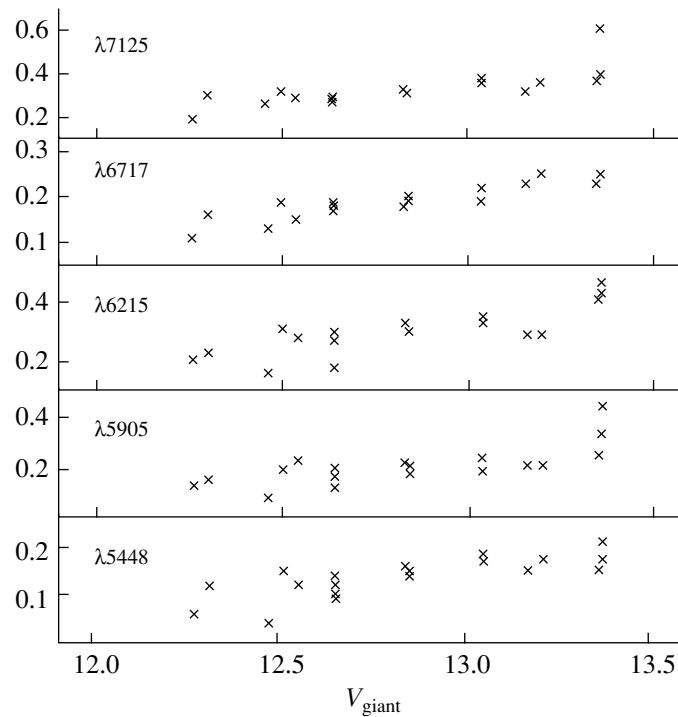
Fig. 3. The dependence of the TiO-band spectral indices introduced in [5] on the V magnitude of the red giant of YY Her.

spectral index—e.g., for the TiO $\lambda7125$ line—on the orbital phase and approximate it with a second-order polynomial, formally, its minimum will coincide with phase $\varphi \approx 0.5$. In other words, at different times, on average, the side of the red giant illuminated by the hot component has an earlier spectral type than the shaded side based on the TiO indices. Taking into account the correlation between spectral type and visual brightness, this suggests that the illuminated side also appears somewhat brighter ($\Delta V \approx 0.3$) than the shaded one. However, the rather large scatter of data points due to the intrinsic variability of the red giant prevents drawing firm conclusions about this.

If we plot an V_h–V_g diagram (Table 3), we do not find any obvious relation between the brightnesses of the two components of YY Her. Moreover, the visual brightness of the red giant during our observations (Table 3), which included a strong outburst of YY Her, lies completely within the range of its variations during the minimum brightness of the hot component (estimated earlier from Fig. 2). This also casts doubt on the question of whether heating of the red giant's atmosphere by the companion's radiation exerts a significant effect.

Figure 4 shows the dependences of the parameters W(He II), W(H$_\beta$), and F(He II) on F(3600). For increased clarity, we have plotted along the horizontal axis not the spectral radiation flux, but a function close to the U magnitude of YY Her, designated U'. Obviously, $U' \propto U$. In
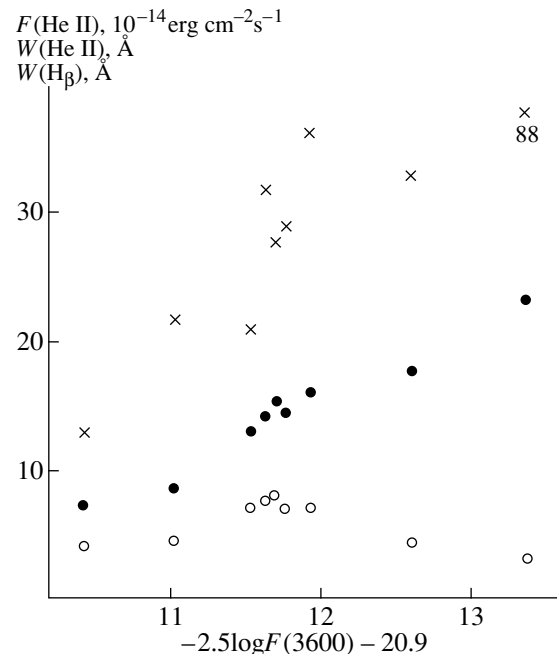

Fig. 4. Dependence of the equivalent widths of the He II $\lambda4686$ (filled circles) and H$_\beta$ (crosses) lines and the flux in the He II line (open circles) on the spectral radiation flux of YY Her at 3600 Å. For increased clarity, the values of W(He II) + 6 are plotted instead of W(He II). The cross labelled "88" in the upper right corner indicates that W(H$_\beta$) ≈ 88 Å on May 9, 1990. See text for further information.

addition, we plotted only those values from Table 2 corresponding to phases $\varphi = 0.5 \pm 0.15$ to avoid any appreciable effect due to eclipse of the hot radiation source. The first point on the right side corresponds to the quiescent state of YY Her (May 9, 1990), and the first point on the left side to the outburst maximum (July 26, 1993). The cross labeled "88" in Fig. 4 indicates that $W(H_\beta) \approx 88$ Å on May 9, 1990 (Table 2); we denoted this point in this way in order not to change the plot scale because of a single data point.

The equivalent width of the He II $\lambda4686$ line (W(He II)) is a very sensitive indicator of the hot component's temperature (T_h) and depends only weakly on the electron temperature of the ionized envelope (T_e). For example, when $T_h \approx 8 \times 10^4$ K, we have W(He II) $\propto T_h^{5.4}$. This value would decrease by a factor of ~1.3 when T_e changes from 1.5×10^4 to 2×10^4 K. Thus, if we exchange one of the suggested values for the electron temperature with the other, the resulting change in the estimated temperature of the hot component will be ~5%.

When L_c photons are completely absorbed in the circumstellar envelope and the temperature of the hot component is high enough (e.g., $>5 \times 10^4$ K) that this component can be considered a black body to good accuracy, the spectral radiation flux $F(3600) = F_h(3600) + F_{gas}(3600)$, or U', is a trustworthy indicator of the bolometric flux from the hot component $F_{h, bol}$. The ratio $F_{h, bol}/F(3600)$ depends only slightly on T_e or T_h. This ratio decreases by only ~6% when T_e changes from 1.5×10^4 to 2×10^4 K (for $T_h \approx 8 \times 10^4$ K). At the same time, it increases by only ~10% when T_h changes from 8×10^4 to 6×10^4 K (for $T_e = 2 \times 10^4$ K). Thus, $F_{h, bol} \propto U'$ with sufficient accuracy.

It is apparent from Fig. 4 that, when the star's U' brightness increases, the equivalent width of the He II $\lambda4686$ line decreases, providing evidence for a decrease in the temperature of the radiation source ionizing the circumstellar envelope. At the same time, the flux in this line first increases and then begins to decrease. Its growth as the temperature of the ionizing radiation source decreases implies a substantial increase in the latter's bolometric luminosity. However, at the final stage, due to the very strong dependence of the He II line intensity on temperature for $T_h \leq 7 \times 10^4$ K, the growth turns into a decrease.

As a rule, the circumstellar envelopes of symbiotic stars are optically thick to the hydrogen Balmer lines [1]. YY Her is no exception. In this case, $W(H_\beta)$ (here $W(H_\beta) = F(H_\beta)/F(3600)$) can be used as an indicator of $\tau(H_\beta)$. Note that, in the optically thin case, $W(H_\beta) > 200$ Å. Figure 4 shows that $\tau(H_\beta)$ grows ($W(H_\beta)$ decreases) as the U brightness increases. The sharpest increase of $\tau(H_\beta)$ occurred during the transition from the quiescent to the active state, and it reached its minimum at the outburst maximum. This suggests that, during the

increasing activity of the hot component of YY Her, its envelope, which we associate with that part of the circumstellar envelope that is eclipsed during the orbital motion of the binary, becomes considerably denser. This is probably due to an increased rate of mass loss by the hot component during its increased activity. This is also indicated by the appearance of the N III $\lambda4645$ line in the star's spectrum, a feature typical of the extended envelopes of hot stars.

The best radiation parameters of a symbiotic star for estimation of the temperature and bolometric flux of its hot component are the energy distribution in the continuum and the equivalent widths of He II lines. When fitting the observed spectrum with the combined contributions of various structural components of YY Her, we required that their continuum coincide for a given observed flux in the He II $\lambda4686$ line. Our model calculations used the following assumptions, based on the results of [4]:

(1) In the basic model, YY Her is taken to be a spherical black-body source of radiation (a hot subdwarf) ionizing the circumstellar envelope.

(2) The circumstellar envelope absorbs all L_c photons from this source and has an electron temperature $(1.5–2) \times 10^4$ K. Note that this range of temperature covers all possible values, at least for regions where the bulk of the envelope's volume emission measure is located [1].

(3) Radiation from the red giant must be added to the radiation from the hot subdwarf and ionized envelope.

The pluses in Table 4 mark observation dates when the spectral energy distribution of YY Her could not be reproduced to good accuracy using the basic symbiotic-star model. A visual impression of the magnitude and character of deviations of the calculated from the observed energy distributions can be obtained from Fig. 5, which shows these energy distributions for the spectrum taken on August 1993. Note that we derived the "deviation" curve by subtracting the calculated from the observed energy distribution, smoothing with the polynomial $(a\lambda^{-2} + b\lambda^{-1} + c)$. In other words, if the spectral energy distribution of YY Her cannot be accurately reproduced by the basic model, we can achieve a good approximation by adding to the three basic sources one more source with a polynomial spectral energy distribution. This is how we obtained the final calculated spectral energy distributions for the dates marked with plus signs in Table 4. The good quality of the resulting approximation of the observed continuum is evident from Fig. 5.

Munari *et al.* [4] analyzed UV spectra of YY Her, supplemented by some optical spectra. In their case, the deviation of the observed energy distribution from the distribution calculated with the basic model, when present, was most obvious near ~2200 Å. In addition, they found that curves derived by subtracting the calculated from the observed energy distributions could be

well described by a black-body curve corresponding to a temperature of ~1.3×10^4 K. In essence, the polynomial we used to smooth the "deviation" between the calculated and observed energy distributions reproduces the corresponding part of a black-body curve with a temperature of about $(1–1.5) \times 10^4$ K. In the analysis of the UV spectra of YY Her, the total flux under the smoothed "deviation" curve did not exceed 15% of the hot component's bolometric luminosity. However, it can appreciably change the "standard" shape of the energy distribution described in the basic model. This is illustrated in Fig. 5 using spectra taken in August and November of 1993. We are not sure of the origin of the deviation, and speculation on this subject is beyond the scope of this paper.

Figure 5 shows the spectra of YY Her with their best approximations within the limits of the above assumptions. Note again that the model reproduces both the continuum and the radiation flux in the He II λ4686 line. In Table 4, we present estimates of the hot subdwarf's bolometric flux and temperature ($F_{h, bol}$, T_h) for dates corresponding to phases $\varphi = 0.5 \pm 0.15$ and $\varphi \approx 0.8$. The first two lines of Table 4 contain data from [4, 9]. Figure 6 shows a $\log F_{h, bol}$–$\log T_h$ diagram for phases near 0.5.

A linear interpolation of this relation yields $F_{h, bol} \propto T_h^{\alpha}$ (where $\alpha \approx -5$), though the scatter is rather large, suggesting that there is not a unique relation between the hot component's temperature and luminosity.

The upper left panel of Fig. 5 shows spectra of YY Her in the quiescent state and at outburst maximum taken at the same orbital phase. The upper right panel of Fig. 5 shows the decomposition of the total radiation into separate components for the spectrum taken in August 1993, one month after the outburst maximum. The observed energy distribution for the November 1993 spectrum can be reproduced using the basic model. However, there is a considerable disagreement between the calculated and observed energy distributions in August 1993. These spectra are shown in the lower left panel of Fig. 5. The lower right panel shows the spectra at the outburst maximum (July 26, 1993) and at the same phase one orbital period later (March 11, 1995). The latter spectrum resembles that of November 1993. As a whole, Fig. 5 illustrates the evolution of the spectrum of YY Her during the strong outburst.

It is evident from Table 4 that, one month after the maximum brightness of the bright component, its luminosity decreased by a factor of ~2 with only insignificant changes of the hot subdwarf's temperature. During the following 1.5 months, the luminosity dropped again by a factor of ~2, while the temperature of the hot dwarf appreciably increased. After a local minimum, the luminosity again increased, and, in November 1993, four months after the maximum, the hot subdwarf's temperature and luminosity were approximately the same as one month before maximum.

Table 4. Bolometric flux and effective temperature of the hot component of YY Her*

Date	Phase	T_h	$F_{h,bol}$
Aug. 12, 1980	−5.6	10.7	1.2
Sep. 13, 1982	−4.3	10.2	1.3
May 9, 1990	0.43	8.8	1.1
June 10, 1993+	2.34	8.2	4.7
July 26, 1993+	2.42	6.0	12.2
Aug. 25, 1993+	2.47	6.5	6.5
Oct. 7, 1993+	2.55	8.0	2.8
Nov. 22, 1993	2.61	7.9	5.5
Dec. 16, 1993	2.67	7.5	6.0
Feb. 25, 1994	2.79	8.6	1.9
Mar. 11, 1995	3.43	7.7	4.6
July 22, 1995	3.65	8.2	2.3
Oct. 14, 1995	3.80	8.5	1.3
May 12, 1997	4.77	10.5	1.0

* The flux and temperature are in 10^{-9} erg cm^{-2} s^{-1} and 10^4 K, respectively. The data in the first two lines are from [4, 9]. Pluses indicate dates for which it is impossible to reproduce the spectral energy distribution of YY Her using the basic model (see text for details).

In February 1994 ($\varphi = 2.79$), the bolometric flux dropped considerably. However, this decrease could be due to an eclipse of the hot radiation source. Comparing our estimates of the bolometric flux for $\varphi \approx 0.8$ (Table 4), we note that they decrease with time; i.e., the hot component gradually returns to its quiet state. It reached quiescence in 1998 (Fig. 1), five orbital periods later.

Figure 5 shows that the spectra of YY Her taken at phases $\varphi = 2.61$ and 3.43 are similar, as are our estimates of the parameters of the hot component (Table 4). This suggests that the photometric minimum was due, not only to eclipse of the hot radiation source, but also to an actual decrease in the luminosity of the hot component, which experienced a second outburst one orbital period later, though it was not as bright as the first. Indirectly, the fact that the ratios of bolometric fluxes are equal at phases $\varphi = 2.42$, 2.61 and $\varphi = 3.43$, 3.65 (Table 4) provides evidence for such a wavelike development of the outburst of YY Her. In other words, the rate of luminosity decrease was approximately the same during these intervals. Two outbursts in a row were observed in Z And at $\Delta \varphi \approx 0.8$ in 1984–1985; the second outburst was stronger and coincided exactly with the phase of photometric minimum. This suggested that the two local brightness maxima corresponded to separate outbursts and that the hot component of the binary system was not eclipsed by the red giant, though that system is observed at a large angle [6, 10].
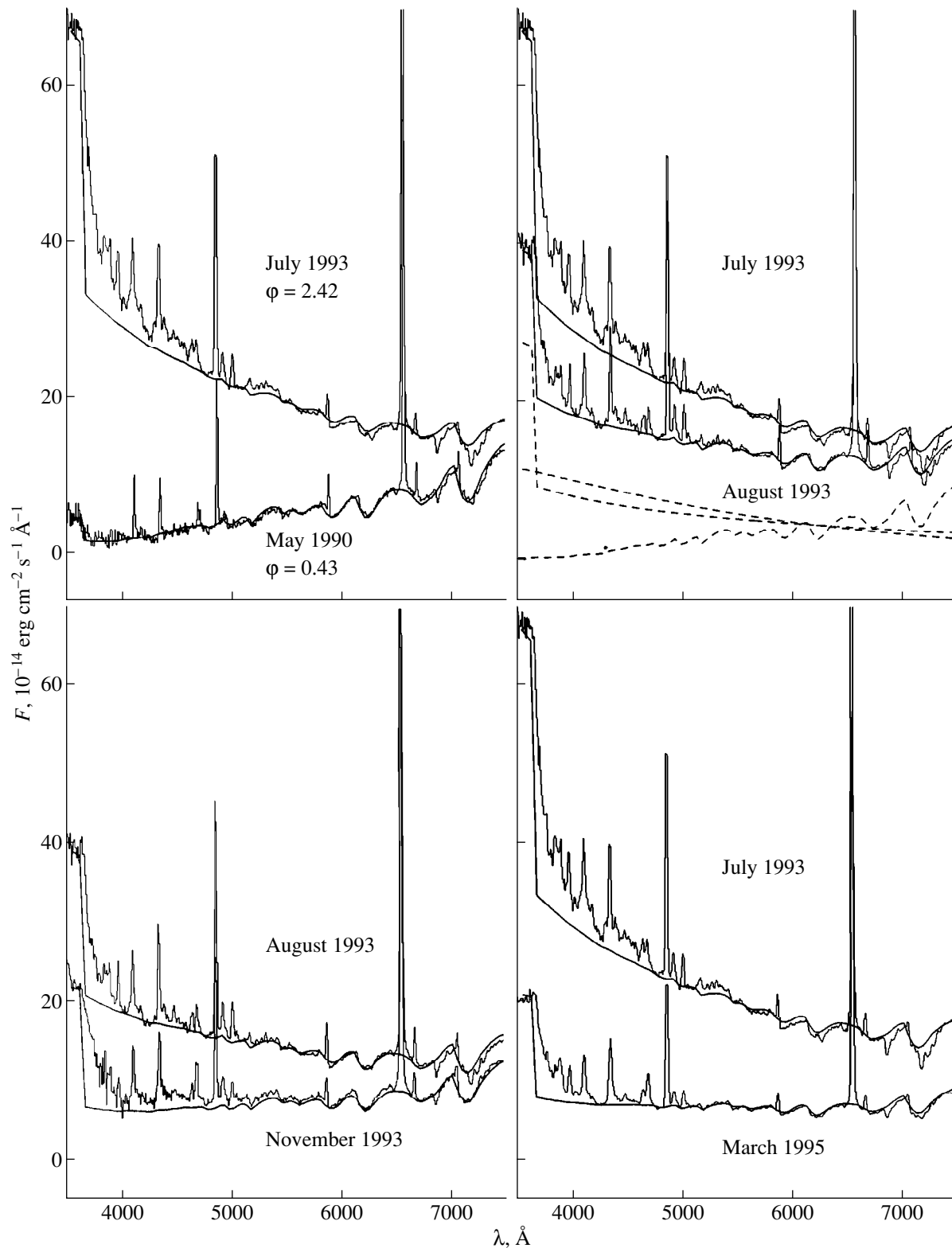
Fig. 5. Spectra of YY Her in its quiescent state and during the evolution of the strong outburst of 1993. The solid lines are computed energy distributions in the star's continuum. In the upper right panel, the dashed lines show spectral energy distributions of the radiation sources forming the continuum in August 1993. The source with a prominent Balmer jump is the combined radiation of the hot subdwarf and the ionized nebula. The source with absorption bands is the red giant. The remaining (third) component is a radiation source to be added to the three "principal" sources in order to reproduce the observed energy distribution (see text for more detail).

4. DISCUSSION

The most complete light curves of symbiotic stars have been obtained at visual wavelengths, and it is these that are usually cited when describing the state of a star. If its visual brightness fluctuates within several tenths of a magnitude of its minimum brightness, a classical symbiotic star is said to be quiescent. It stays in this state for most of its life, entering the active state, which usually resembles a nova-like outburst, once every several decades.

The mean visual brightness of YY Her in the quiescent state is $V \sim 13$. From the $(B - V)$–V diagram (Fig. 2), the $B - V$ value at this brightness level can have values from ≈ 1.4 to ≈ 0.9, and, from the $(B - V)$–U diagram, the U brightness can vary between $\sim 14^m$ and $\sim 13^m$. Here, we neglect the left-most group of data points in Fig. 2, corresponding to the most recent brightness minimum of YY Her, which is due to an eclipse of the hot source and not to intrinsic variability.

Thus, in the quiescent state, the U brightness of the hot radiation source of YY Her can change by more than a factor of two. This means that the bolometric luminosity of the hot component ($U \propto U' \propto F_{h, bol}$) changes by more than a factor of two. It is difficult to call such a state quiescent. Comparing the three uppermost lines of Table 4, we see that the temperature can have different values for the same bolometric luminosity of the hot component.

At the minimum brightness of the hot component of YY Her, its bolometric flux fluctuates near the value $F_{h, bol} \approx 1.2 \times 10^{-9}$ erg cm^{-2} s^{-1}, and its temperature is in the range $(9–11) \times 10^4$ K. In this state, $F_{h, bol}/F_{c, bol} \approx 0.9$; i.e., the hot component's luminosity is slightly below that of the cool component. A similar luminosity ratio is observed for other classical symbiotic stars, such as Z And, CI Cyg, BF Cyg, AX Per, and AG Dra [9, 11, 12]. Since the light curves of all these stars have a periodic component, which is especially appreciable in the U filter, we emphasize that this conclusion refers to the phases of their photometric maxima.

The fact that $L_{h, bol}/L_{c, bol} \leq 1$ in the quiescent state of a classical symbiotic star must be taken into account in evolutionary models. Thus, if its hot component is a dwarf with a degenerate helium or carbon–oxygen core whose mass exceeds that of the core of the red giant, we can assume that the burning of its surface hydrogen envelope is completed and that it has entered its early cooling phase. In this case, novalike outbursts can only be associated with accretion.

In principle, the rate of accretion of matter from the red giant onto the degenerate core of the dwarf can be high enough to continually resupply its hydrogen envelope, making surface burning possible. Such a stationary burning regime has been considered in outburst models for classical symbiotic stars (see [2, 6] and references therein). In this case, the dwarf's mass must be lower than that of the red giant core (see [13] and references therein). In turn, this influences the evolution of
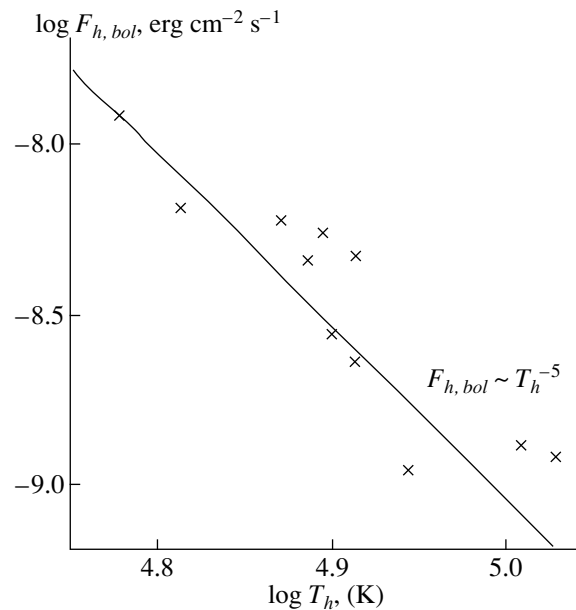

Fig. 6. Relation between the logarithm of the hot subdwarf's bolometric flux and the logarithm of its temperature. A linear approximation yields the power law $F_{h, bol} \propto (T_h)^{-5}$.

the binary system prior to the emergence of the classical symbiotic star. For example, the binary system's period must have increased during the first mass exchange, when the dwarf was still the core of a red giant. This could allow the companion of the symbiotic star's red component to ascend further along the red giant branch. Note also that, if the cool component of a classical symbiotic star is a red giant of luminosity class III, the hot component must be a low-mass helium dwarf.

In the case of the hot component of YY Her, its activity implies increased luminosity and decreased temperature ($F_{h, bol} \propto T_h^{-5}$), though observations do not show a unique relation between these parameters (Fig. 5). At the outburst maximum of the hot component, its bolometric flux increases by a factor of ~ 10, whereas its temperature decreases to $\sim 6 \times 10^4$ K (Table 4).

Among other classical symbiotic stars studied in detail, only the hot component of AG Dra has a comparable luminosity increase during strong outbursts [11, 14]; in this case, as for YY Her, $F_{h, bol} \propto T_h^{-5}$ [11]. However for other symbiotic stars, such as CI Cyg, BF Cyg, AX Per, and Z And, $L_{h, max}/L_{h, min} \leq 3$ [1, 6, 9, 11, 12, 14]. This provides the main argument for the thermonuclear model for the outbursts of the hot components in classical symbiotic stars. However, their time characteristics virtually rule out this model, at least in its original form, which also includes the postulated capture of some fraction of the red giant's stellar wind by the hot component (see [4, 6] and references therein).

In models explaining the outbursts of classical symbiotic stars as the result of the nonstationary disk accretion of matter from a red giant onto its companion, it is usually assumed that the companion is a main sequence star [2, 6, 15]. In this case, it should be a yellow or red dwarf, and the red giant, which fills its Roche lobe, should have luminosity class II ($L_g \approx 3600L_\odot$ for YY Her). In addition, the binary system must be observed nearly edge-on if it is to show a well-defined symbiotic spectrum [16].

In principle, a pure accretion model can reproduce any particular state of a symbiotic star; i.e., it can provide typical values of the hot component's temperature and bolometric luminosity [15]. However, in such models, even with the most modern calculations of the structure of the boundary layer, its temperature increases with increasing accretion rate [15], whereas in reality it decreases. This difficulty can probably be overcome: The model calculations still neglect a number of factors that tend to decrease the temperature of the boundary layer. Essentially, it has only been demonstrated that increasing the size at high accretion rates cannot explain the temperature decrease. A stellar wind regulating the effective radius of the hot star's photosphere could do it, and there are many reasons to believe that the intensity of such winds increase significantly during outburst. In particular, if we assume, as is usually done, that the temperature of the hot star and the mass loss rate are related as $\dot{M}v = L/c$, then, if the velocity of the matter in the stellar wind remains constant as its intensity changes, the luminosity and temperature will be related as $L \propto T^\alpha$, where $\alpha \approx 4.5$ [17], similar to the observed relation. Note also that, at its maximum, the hot component's luminosity reaches the Eddington limit, so that the accretion acquires a quasi-spherical geometry.

As already noted, in order for this model of a symbiotic binary to produce a well-defined total spectrum, the system must be observed nearly edge-on. In other words, not only a substantial fraction of the ionized circumstellar envelope, with the bulk of its emission measure concentrated around the hot component, must be eclipsed, but also the hot component itself. This is true of the stars CI Cyg [18], AX Per [19], and BF Cyg [20], but not of Z And [6]. To prove that an eclipse occurs, it is necessary to observe the symbiotic star at the short-wavelength end of the UV range, close to the photometric minimum. Such observations exist for Z And; however, it underwent a strong outburst during the observations, and the drop in the energy distribution in the corresponding part of the spectral range was attributed to a drastic decrease of the hot component's temperature [6, 10] and not to its eclipse.

If a symbiotic binary has a small inclination to the line of sight, it will appear as a red giant in a pair with a hot giant, with strong He II $\lambda\lambda$1640, 4686 lines in the spectrum. The system should also show burst activity. Such binaries have not been detected, though there do exist "red giant + hot giant" pairs, such as AX Mon or 17 Lep. However, these lack high-excitation spectra and burst activity.

The apparent absence of such pairs casts doubt on models of classical symbiotic stars with main-sequence hot components. In addition, accretion phenomena can occur in such symbiotic binary systems, so that it would be impossible to distinguish the hot radiation source (star + accretion disk + gas) from that of a symbiotic nova with a simpler structure (hot subdwarf + gas) [21].

This difficulty is not so severe if we assume that the hot component is a dwarf with a degenerate core instead of a main sequence star and that the mean accretion rate can produce a regime of stationary hydrogen-envelope burning at its surface. In this case, the minimal (quiescent) brightness level of the hot component will be determined by its intrinsic luminosity. For $T_h \approx 10^5$ K and $L_h \approx 0.9L_g \approx 3200L_\odot$, the photospheric radius will be $R_h \approx 0.2R_\odot$. In other words, the hot component will have an extended atmosphere. No calculations of disk accretion onto such a star have been performed, but it is obvious that observable effects will differ from those for models with disk accretion onto a main sequence star.

Finally, we would like to note that the presence of a periodic component in the light curve has now become a required property of symbiotic stars. This is true not only for classical symbiotic stars, but also for stars that do not show novalike outbursts but have orbital periods similar to those of classical symbiotic stars (one to two years). The *U* brightness amplitude indicates that a substantial fraction of the ionized envelope's volume emission measure can be obscured from the observer. A similar phenomenon was observed for the symbiotic nova PU Vul, for which the photometric period and the duration of its "total eclipse" are ~13.5 yrs and ~0.06*P*, respectively [22]. In addition, it turns out that PU Vul and YY Her have approximately the same linear dimensions for the eclipsed part of the ionized envelope containing more than 50% of the volume emission measure. In PU Vul, the hot subdwarf moves in the stellar wind of the cool component, which is undoubtedly far from filling its Roche lobe. Nevertheless, it appears that, as for closer symbiotic binaries, a considerable fraction of this symbiotic nova's envelope emission measure is located near the hot component. Thus, the problem of detecting eclipsing variables among symbiotic stars, which persisted for a long time after their discovery and was solved only after the advent of systematic photometric observations in the violet, is now replaced by the task of finding symbiotic systems without a periodic component in their light curves.

REFERENCES

1. A. A. Boyarchuk, *Eruptive Stars* [in Russian], Ed. by A. A. Boyarchuk and R. E. Gershberg (Nauka, Moscow, 1976), p. 113.

2. S. J. Kenyon, *The Symbiotic Stars* (Cambridge University Press, Cambridge, 1986).

3. U. Munari, M. Rejkuba, M. Hazen, *et al.*, Astron. Astrophys. **323**, 113 (1997).

4. U. Munari, E. A. Kolotilov, A. A. Popova, *et al.*, Astron. Zh. **74**, 898 (1997).

5. L. D. Beshenova and A. V. Kharitonov, Tr. Astrofiz. Inst., Akad. Nauk Kaz. SSR **27**, 1 (1975).

6. J. Mikolajewska and S. J. Kenyon, Astron. J. **112**, 1659 (1996).

7. S. J. Kenyon and T. Fernández-Castro, Astron. J. **93**, 938 (1987).

8. A. Skopal, Astron. Astrophys. **318**, 53 (1998).

9. A. P. Ipatov and B. F. Yudin, Astron. Tsirk. **1471**, 4 (1986).

10. T. Fernández-Castro, R. Gonzá-Riestra, A. Cassatella, *et al.*, Astrophys. J. **442**, 366 (1995).

11. B. F. Yudin, Astron. Zh. **63**, 137 (1986).

12. A. P. Ipatov and B. F. Yudin, Astrofizika **25**, 435 (1986).

13. I. Iben and A. V. Tutukov, Astrophys. J., Suppl. Ser. **105**, 145 (1996).

14. J. Mikolajewska, S. Kenyon, M. Mikolajewski, *et al.*, Astron. J. **109**, 1289 (1995).

15. P. Godon, Astrophys. J. **462**, 456 (1996).

16. B. F. Yudin, Astrophys. Space Sci. **135**, 143 (1987).

17. G. T. Bath, Mon. Not. R. Astron. Soc. **182**, 35 (1978).

18. T. S. Belyakina, Izv. Krymsk. Astrofiz. Obs. **59**, 133 (1979).

19. J. Mikolajewska and S. J. Kenyon, Astron. J. **103**, 579 (1992).

20. A. Scopal, A. Vittone, L. Erico, *et al.*, Mon. Not. R. Astron. Soc. **292**, 703 (1997).

21. U. Murset, H. Nussbaumer, H. M. Schmid, *et al.*, Astron. Astrophys. **248**, 458 (1991).

22. E. A. Kolotilov, U. Munari, and B. F. Yudin, Mon. Not. R. Astron. Soc. **275**, 185 (1995).

Translated by N. Samus'

Properties of Oscillations in Sunspot Penumbras

N. I. Kobanov

Institute for Solar-Terrestrial Physics, Russian Academy of Sciences, Siberian Division
P. O. Box 4026, Irkutsk, 664033 Russia
Received March 3, 1999

Abstract—Observations of oscillations in the penumbras of seven sunspots are analyzed. High-sensitivity differential measurements of the line-of-sight velocity (11 time series) and variations of the Ni I 4857 Å and H_β line profiles (four series) have provided new data making it possible to improve estimates of the amplitude and spectral characteristics of the oscillations. In the middle penumbras, oscillations of the line-of-sight velocity with fundamental periods of 5 and 8–10 min predominate at the photospheric level; their amplitude does not exceed 40–50 m/s, and the spatial coherence scale in the radial direction is no greater than $5''$–$10''$. At frequencies of 0.5–2.0 mHz, the phase difference between the photosphere and chromosphere (NiI 4857 Å–H_β) is close to 180°. The line-of-sight velocity component due to Evershed motions is responsible for oscillations with periods of 15–35 min, which occur synchronously at both heights. © *2000 MAIK "Nauka/Interperiodica".*

1. INTRODUCTION

In spite of the abundance of investigations of sunspot oscillatory processes that have been carried out, this problem will continue to be of interest for a considerable time. A sunspot with sharp boundaries and physical conditions that are very different from those in the surrounding photosphere is a convenient object for local helioseismology studies. For example, oscillations in sunspot penumbras are characterized by an increase of spatial dimensions. It is reasonable to assume that a sunspot penumbra oscillates as a single unit at the photospheric level [1, 2]. In this case, we have a natural, rather large piston, whose location and oscillation frequency can be determined. All this provides hope that, in some problems of local helioseismology, large, well-developed, regular-shaped sunspots can be treated as a "source" of oscillations. In this approach, sunspots can be used as seismic probes for studying the propagation of oscillations in the surrounding atmosphere, zone of temperature minimum, and lower chromosphere. The geometry of a sunspot is quite suitable for two modern methods in local helioseismology: the ring-diagram method [3] and the time–distance method [4]. To successfully solve problems of this sort, the parameters of the "source" must be well understood. The most important of these is the spectral distribution of the oscillations.

However, observations of oscillations of the line-of-sight velocities in sunspots are hindered by their small amplitude and the presence of strong quasi-stationary motions, as well as by the small signal-to-noise ratios due to the low light intensity involved; this leads to wide scatter in the resulting observational data. The data for sunspot penumbras are especially varied [2, 5–11]. At the same time, penumbras, with their strong horizontal fields, are unique objects for studies of the

interaction of the transverse magnetic field with oscillatory and stationary motions. What then is the origin of this situation? It is obvious that, due to the presence of strong magnetic fields, the amplitudes of line-of-sight velocity oscillations in the penumbra photosphere are significantly smaller than in the umbra. Furthermore, penumbra oscillations are masked by powerful Evershed currents. At each point of the penumbra, a multitude of motions with different temporal and spatial frequencies arriving from different directions are superimposed. The usual methods for measuring the line-of-sight velocity have no selectivity in either spatial wavelength or direction; therefore, the observed mixture of a large number of components is often noiselike.

On the whole, according to the recent review of Lites [2], the following pattern is characteristic of sunspot penumbras:

(a) There are no confidently identifiable oscillations at the photospheric level.

(b) At the chromospheric level, oscillations with periods from 4–5 min near the umbra to 10 min at the outer boundary of the penumbra (so-called traveling waves) are observed.

Note that the 3-min oscillations that are characteristic of the chromosphere above sunspot umbras are suppressed.

In addition to the papers cited above, some results are presented in [12–22]. The few studies published later [23–25] do not fundamentally change the situation. For example, Marco *et al.* [24] found from observations of two sunspots that 5-min (in some spectra, 7-min) oscillations are present in umbras at the photospheric level. Most of the power of these oscillations is concentrated in the outer penumbra. Measurements at the two heights were carried out at different times. A systematic instrumental drift of the spectrum was

removed by subtracting a combination of three cubic splines, and the 0–1.5-mHz band was excluded from the calculations. Note that this procedure does not remove quasi-periodic components of the spectrograph instrumental noise. Photographic echelle spectra (one sunspot, a 55-min time series) obtained in several spectral lines are analyzed in [25]. Spectra were taken every 30 s with an exposure of 4 s; this does not exclude spurious signal components due to aliasing (transfer of high-frequency fluctuations to low frequencies). It is noted that the bulk of the power of the line-of-sight velocity oscillations falls at 4 mHz. At the photospheric level, a period of about 15 min is also detected and is ascribed to fluctuations of the Evershed velocity [26]. The oscillation amplitude at the photospheric level is 200–250 m/s. Even a brief analysis of these works shows that inconsistencies and uncertainties in the photospheric oscillation parameters persist. Moreover, the statistics are poor: Only three sunspots are considered in two studies, contributing to the wide scatter of the results. There is a need for a study of oscillations using other, nontraditional methods.

The aim of the present work is to improve estimates of the spectral distributions of line-of-sight velocity oscillations at two heights in sunspot penumbras. The main task was to confirm or disprove the presence of oscillations in the penumbra photosphere. In addition, it is of interest to determine whether periodic variations of the steepness of the H_β 4861Å and NiI 4857Å line profiles occur in penumbras. These measurements can provide information about the dynamics of unresolved spatial structures. Achieving this objective depended to a considerable extent on our choice of measurement methods.

2. THE METHOD

We used two observational methods. To observe the line-of-sight velocity oscillations, we used a differential method [27, 28], which has been proven to work well when studying local oscillations in sunspots, filaments, and prominences. Differential methods measure only relative motions of areas on the solar surface; therefore, they are naturally suited for investigations of wave processes. The differential method completely suppresses the instrumental noise of the spectrograph. Furthermore, it enables us to isolate in the composite mixture of oscillatory and other motions in which an object participates, only those oscillations with specified spatial parameters (size, direction). This can be correlated with the dimensions and configuration of the object under study. The influence of large-scale irregularities of the Earth's atmosphere on the measurements is also considerably decreased. This combination of properties of the method provides high sensitivity measurements, as well as purity and quality of the time series, making it possible to detect well-pronounced oscillations of the line-of-sight velocities in penumbra photospheres.

We also investigated variations of the steepness of the H_β 4861 Å and NiI 4857 Å line profiles. It is by no means easy to detect these line-profile variations, which are only 10^{-3} of the intensity, especially if the measurements are carried out in direct-current mode. To understand how our method (used in [29]) works, consider the formula for the signal describing measurements of the longitudinal component of the magnetic field intensity. It is known that $S \sim f(\partial I/\partial\lambda, \Delta\lambda_H)$, where $\Delta\lambda_H$ is the Zeeman splitting of the spectral line and $\partial I/\partial\lambda$ describes the steepness of the line profile. If we set $\Delta\lambda_H = $ const, then $S \sim f(\partial I/\partial\lambda)$. After we have created an artificial splitting of a spectral line $\Delta\lambda_H = \Delta\lambda_0$, changes in the signal S will be due only to $\partial I/\partial\lambda$. The artificial splitting is formed using a thin calcite plate and a quarter-wave plate, which were mounted immediately behind the entrance slit of the spectrograph, in front of the electro-optical modulator. Thus, it is possible to realize modulation measurements of variations of $\partial I/\partial\lambda$.

In both types of observation, we used an 80-cm telescope equipped with a photoelectric guide, image rotator, and magnetograph operating in a mode for measurement of the longitudinal field component. During the observations, the electro-optical modulator was controlled by a square-wave signal with a frequency of 1.2 kHz; the time constant of the synchronous integrator was 10 s.

3. OBSERVATIONS

From July to September 1998, we obtained 11 series of observations for seven sunspot groups with measurements of the differential line-of-sight velocity and four series recording time variations of the H_β and NiI 4857 Å profiles with a mean duration of about 1 h. The H_β 4861 Å line forms in the chromosphere and is widely used in observations of filaments and prominences. The photospheric line NiI 4857 Å is insensitive to temperature fluctuations and has a lower excitation potential of 4.71 eV.

The table lists the general characteristics of the observational data and the fundamental periods derived from the calculated power spectra. When possible, the observations were carried out for large sunspots with a well-developed umbra and penumbra. We selected out time intervals with minimal image jitter and scattered light. For this reason, the durations of the time series varied between 40 and 80 min.

We will now present additional arguments that such durations are close to optimal for the problem at hand. On the one hand, it is clear that, to obtain power spectra with high frequency resolution, we should use observational series that are as long as possible. However, observations have shown that the physical conditions in sunspots are rather dynamic, so that the spectrum of a long series will become blurred. For example, the mean lifetime of penumbra dark filaments is close to 1.5 h [30]. Furthermore, in differential measurements of the

Observational data and oscillation periods

Active region (NOAA number)*	Date and UT of observations	Type of observation (V, S)**	Main periods, min	
			photosphere	chromosphere
8260 (W)	04.07 00:40–01:35	V	5.2, 9.5	3, 5.5, 7.5
8263 (W)	05.07 02:37–0.3:40	V	4.35, 8, 13	2.8, 5.2, 8.7, 15
	05.07 05:07–0.5:52	V	5.2, 8.7, 11.6	2.6, 5.5, 9.5
	05.07 06:01–07:01	V	5.5, 10.4	3, 4.7, 10.5
8264 (E)	05.07 00:18–01:05	V	5, 10.4, 23	2.9, 4.3, 21
(W)	05.07 01:12–02:30	V	5.4, 9.5	3.5, 5.2, 8.7
8297 (E)	12.08 01:20–02:34	V	5, 8	2.8, 4.3, 7.5
	12.08 03:15–04:02	V	5.2, 9	3, 5.2, 8
8299 (W)	13.08 02:31–03:40	V	5, 9, 35	3.2, 3.7, 5, 8, 35
	13.08 04:09–04:55	S	8.7	8.0
8301 (N)	13.08 05:02–05:58	S	5.2, 8.7	7.5
	13.08 06:03–06:48	S	5.5, 10	3.2, 6.9
	13.08 08:14–09:20	S	9.5	8
8326 (W)	07.09 01:50–03:23	V	4.4, 8	3.6, 5.5, 8.7
(E)	07.09 06:28–07:14	V	5, 7.5	2.3, 6, 9.5

 * W, E, N, western, eastern, and northern parts of the penumbra.
** V, differential measurements of the line-of-sight velocity; S, steepness variations of the part of the contour studied.

line-of-sight velocity in sunspots, the maximum contribution to the signal comes from short-wavelength spatial harmonics, which in our case are formally equivalent to acoustic p modes with $l = 250–500$. The lifetime of these modes is estimated to be from 30 min to 2–3 h [31]. In our conditions, appreciable changes of the scattered light and of image jitter are also noted over similar time intervals. Therefore, if high uniformity of the observational data within a time series is required, it is preferable to restrict the duration to 50–90 min.

The parameters of the polarization optics of the modulator and photometer were set so that the measurements were carried out in the wings of the spectral lines, at wavelengths shifted from the core by ± 40 mÅ. For H$_\beta$, this corresponds to heights of no less than 1500–2000 km [32], and for NiI, to heights of about 100–200 km. When studying oscillations of the line-of-sight velocity in sunspot penumbras, we set the separation between area elements to 5.5″. As a rule, the areas observed were arranged radially along the direction of
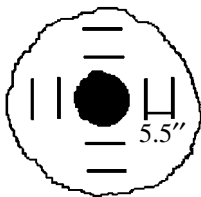
filaments in the penumbra, in its middle part, as shown schematically in Fig. 1. This was motivated by our interest in oscillations in the zone where the Evershed currents are strongest. As shown by Title *et al.* [33], this is characteristic of sites where the direction of the magnetic field is nearly horizontal. On the other hand, it was necessary to remove possible contributions to the signal from the sunspot umbra and the quiescent photosphere. This latter contribution can appear when the areas observed are close to the boundaries of the penumbra, as well as under conditions of increased scattered light and image jitter.

We chose a 4″ entrance aperture, though the atmospheric conditions provided a mean resolution of about 1.5″. This aperture matched the distance between the areas observed and enabled us to record the oscillation properties that were the most common for the entire penumbra, while decreasing the influence of fine-structure elements on the measurement results. The entrance slit for the H$_\beta$ line could be widened to increase the signal-to-noise ratio, but, in this case, the instrumental profile would considerably affect the shape of the NiI line. Image drift due to the solar rotation was removed via slow, automated motion of the photoguide at a rate determined from the sunspot coordinates.

4. RESULTS

One characteristic of the five observational series is that the signals for the line-of-sight velocities in H$_\beta$ and NiI have opposite signs; i.e., they are shifted in opposite directions from the zero level. This is due to the

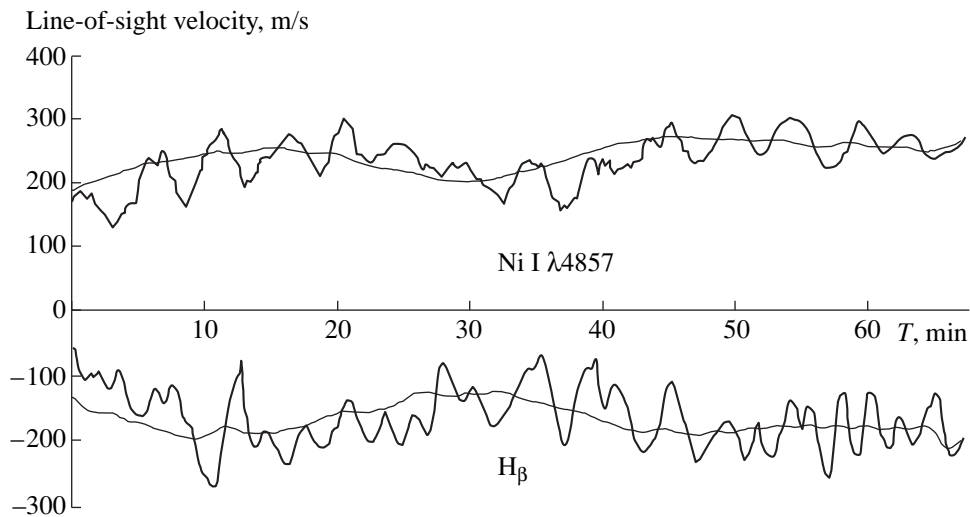**Fig. 1.** Location of areas observed in the sunspot penumbras.

Fig. 2. Periodic variations of the differential line-of-sight velocity signal at two heights in the middle penumbras.

action of Evershed currents, which are oppositely directed in the photosphere and chromosphere of sunspot penumbras. Because of their deviation from the direction perpendicular to the line of sight, a line-of-sight velocity signal appears. It turned out that the differences of the line-of-sight velocities for two penumbra areas also have opposite signs for H_β and NiI. The relative time stability of this signal can be considered indirect confirmation that there were no radical changes in the penumbra structure during the observation. However, this is not true of all the time series. In two cases, time variations of the signal due to Evershed currents are clearly visible. The 70-min series for the penumbra of sunspot NOAA 8299 (Fig. 2) is especially interesting. In Fig. 2, for convenience of presentation, the values of the photospheric velocity (NiI) are increased by a factor of four.

The thin line shows smoothed signals representing the component of the line-of-sight velocities due to Evershed currents. Periodic variations of this component are readily visible. These variations are surprisingly synchronous in the photosphere and chromosphere, testifying that they are related. We have not been able to find any indications of an instrumental origin for this signal. Even if we assume that the Evershed-velocity signal variations are not due to natural oscillation of this parameter in the sunspot penumbra, but result from, for example, quasi-periodic shifts of the image in the entrance aperture, in this case, too, such a rigid connection between the penumbra spatial structures at the two heights should cause surprise. In several cases, the Evershed-velocity variations in the chromosphere lead similar changes in the photosphere by one to several minutes. However, this is a preliminary result and must be tested using a larger data set. Periodic variations of the line-of-sight velocity at both sunspot penumbra heights are clearly visible in all the observational series. Oscillations with a period of

35 min resulting from Evershed currents could formally reflect one of two phenomena:

(a) change of the speed of Evershed currents flowing in a constant direction;

(b) change of the direction (inclination angle of the magnetic field vector) of Evershed currents flowing with a constant speed.

The latter case corresponds to the model considered by Vandakurov [34]. A more specific answer to this question can be obtained through simultaneous measurements of the differential line-of-sight velocity and magnetic-field intensity.

The periods of 5 and 8–10 min dominate in the power spectra of the photospheric oscillations (Figs. 3, 4). The measured amplitude of the differential line-of-sight velocity varies somewhat from one penumbra to another, and even within a single penumbra, depending on the position of the entrance aperture and the time; however, on average, it is 30–40 m/s. It follows from Fig. 4 that the peaks in the 2.5–4.5 mHz frequency band merge into a single broad maximum when averaging several time series for the same penumbra. Since 5-min oscillations are common for the photosphere, both outside active regions and in sunspot umbras, their presence in the penumbra spectra seems natural. The nature of the (8–10)-min oscillations is less clear, since they are not observed at the photospheric level, either in the sunspot umbras or the surrounding photosphere. As early as 1972, Beckers and Schultz [6], and later Lites [2, 7, 15], observed oscillations with these periods in the penumbra chromosphere. Beckers and Schultz [6], who observed the core of the FeI 5434 Å line, at first believed these oscillations to be photospheric; however, Lites [8] convincingly showed that they correspond to the lower chromosphere. Evidently, they were not observed in the photosphere due to their small amplitude (no greater than 40–50 m/s) and masking by Evershed currents.
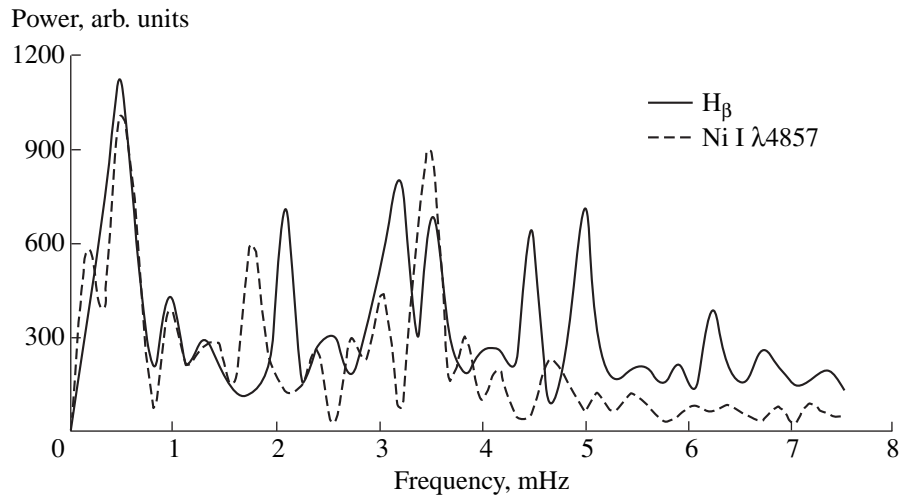
Power, arb. units

Fig. 3. Power spectra of the line-of-sight velocity oscillations recorded in the middle of the western part of the penumbra of sunspot NOAA 8299.
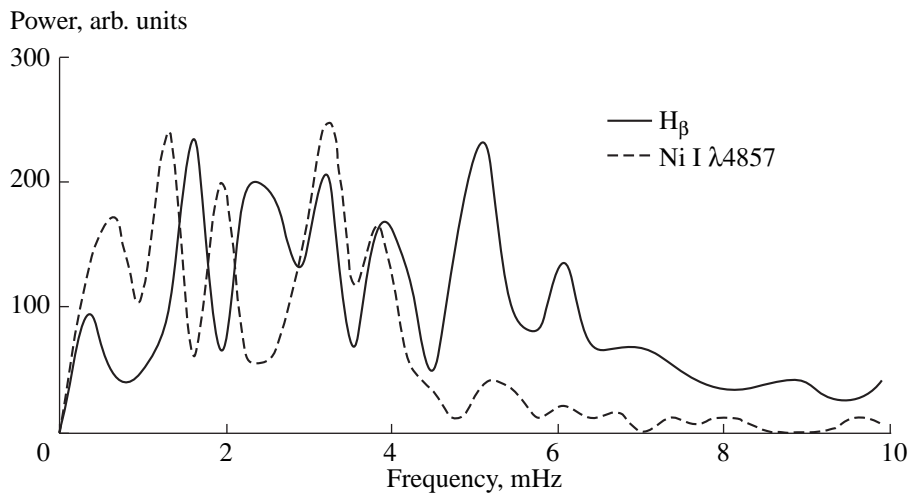
Power, arb. units

Fig. 4. Power spectrum of the line-of-sight velocity variations averaged over three series of observations of the middle part of the penumbra of NOAA 8263.

Remarkably, the 8-min period dominates in the power spectra calculated for the variations of the H_β and NiI profiles. It is quite probable that the (8–10)-min oscillations are characteristic only of the penumbra and represent a distinguishing property of this region. This may be related to the filamentary structure of the penumbra and the horizontal magnetic field. The phase difference $\Delta\phi(V_{ph} - V_{chr})$ is 180° at 0.5–1.9 mHz (Fig. 5). This interval includes both the (15–35)-min oscillations (which, as can be seen from the input data, result from Evershed currents) and the (8–10)-min oscillations. The connection of these latter oscillations with Evershed motions is still speculative. If these oscillations reflect temporal changes of the Evershed velocity, a phase difference close to 180° indicates that they are in phase, not in antiphase. In this case, the opposite directions of the velocities must be taken into account. A

decrease (increase) of the velocity in the photosphere corresponds to a velocity decrease (increase) in the chromosphere. In the primary diagram, this creates the impression that the signals of Fig. 2 are in antiphase. Our observations do not confirm the considerable (more than 20″) spatial coherence of penumbra oscillations noted in [25], at least in the radial direction. In the presence of such coherence, the differential signal from two areas of a penumbra would be close to zero. In addition, our observations indicate horizontal oscillations with a most probable wavelength in the radial direction of about 8″–12″; this is a factor of several smaller that the value given in [25].

Three-minute oscillations are also pronounced in the middle-penumbra chromosphere (Figs. 2, 3); this somewhat contradicts the picture described by Lites [2] for a penumbra chromosphere. In this connection, we note
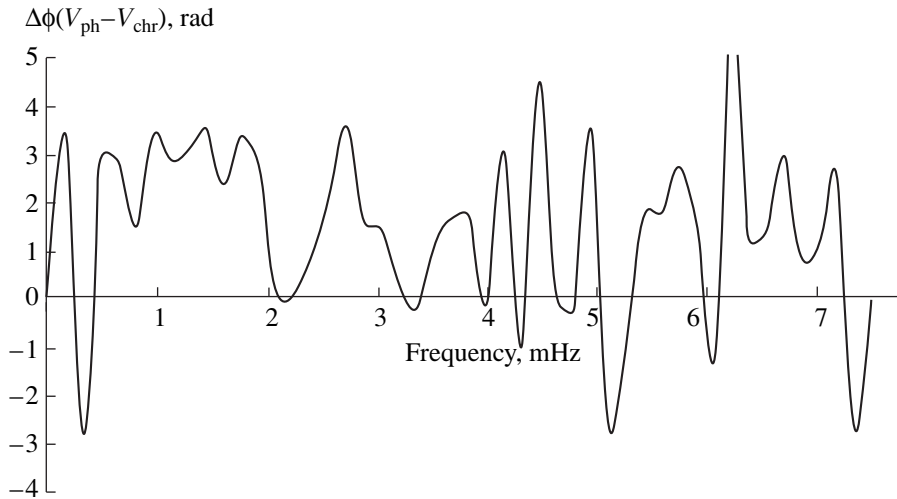
$\Delta\phi(V_{ph} - V_{chr})$, rad

Fig. 5. Phase difference $\Delta\phi(V_{ph} - V_{chr})$, i.e., $\Delta\phi(\text{Ni I} - \text{H}_\beta)$ as a function of frequency for the line-of-sight velocity oscillations in the photosphere and chromosphere of the middle penumbra of NOAA 8299.
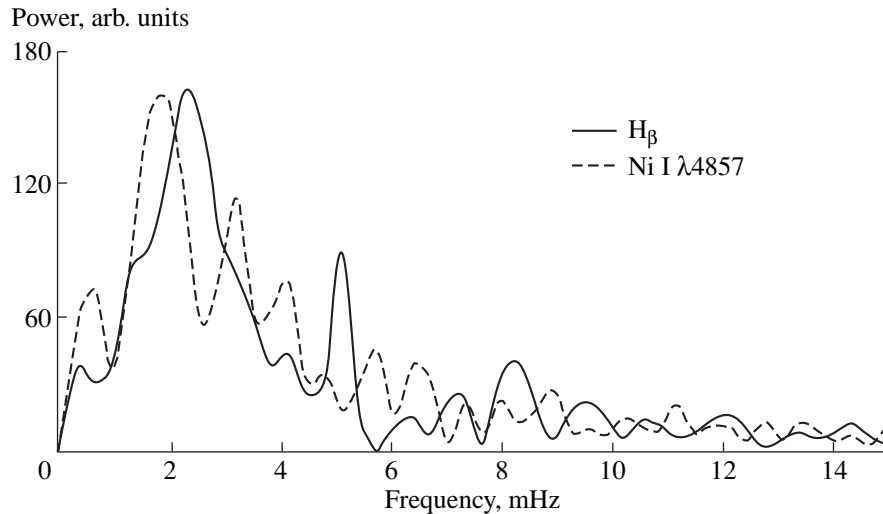

Fig. 6. Variations of the spectral-line profiles in the middle penumbra of NOAA 8301.

that Musman *et al.* [9] reported evidence for 3-min penumbra oscillations even in FeI 5576 Å line observations. Their observations appeared to reveal quasi-periodic perturbations with similar periods propagating with a high phase velocity. However, these results were later placed in doubt [10].

We observed variations of the H_β and NiI 4857 Å profiles in the penumbras of NOAA 8301 and NOAA 8299. Figure 6 presents the power spectra, averaged over three time series for NOAA 8301. At the photospheric level (the NiI 4857 Å line), the power maximum is near 8 min. The spectrum of the H_β variations contains a similar peak, shifted slightly toward higher frequencies. In addition, the 3-min period is appreciable in H_β. As noted above, the H_β observations were carried out near the line core, whereas the NiI line

observations corresponded to a part of the wing located closer to the continuum. This provided the maximum difference in the heights for these lines. However, this same factor hinders our interpretation. The most probable origin for changes in the H_β line is spatially unresolved motions, but NiI variations are most likely due to changes in the pressure and temperature. The measured amplitude of the variations was about 3.8×10^{-4} for H_β and about 4×10^{-3} for NiI. The H_β signal had to be multiplied by a factor of 10 to present the corresponding spectra on the same scale.

5. CONCLUSION

(1) We have confidently detected oscillations of the line-of-sight velocity with periods of 5 and 8–10 min in the middle-penumbra photospheres of sunspots. The

spatial coherence of these oscillations in the radial direction (away from the sunspot penumbra) is no more than 5″–10″. Their amplitudes do not exceed 40–50 m/s, hindering detection of the oscillations in the presence of more powerful quasi-stationary motions.

(2) The profiles of the NiI 4857 Å (photosphere) and H$_\beta$ (chromosphere) spectral lines in the penumbras of sunspots display variations with a dominant period of about 8 min.

(3) Oscillations with periods of 8–10 min are a specific property of the penumbras. It is not clear whether there is a connection between these oscillations and Evershed currents.

(4) For line-of-sight velocity variations at 0.5–2 mHz, the photosphere–chromosphere phase difference in the penumbras is close to 180°.

(5) We have observed time variations connected with Evershed motions in individual sunspots. The fundamental periods of the variations are 15–35 min, and the variations in the photosphere and chromosphere are synchronous.

REFERENCES

1. N. I. Kobanov, Solar Phys. **125**, 25 (1990).
2. B. W. Lites, *Sunspots: Theory and Observations*, Ed. by J. H. Thomas and N. O. Weiss (1992), p. 261.
3. F. Hill, Astrophys. J. **333**, 996 (1988).
4. T. L. Duvall, S. M. Jefferies, J. W. Harvey, *et al.*, Nature **362**, 430 (1993).
5. H. Balthasar, W. Schmidt, and E. Wiehr, Solar Phys. **171**, 331 (1997).
6. J. M. Beckers and R. B. Schultz, Solar Phys. **27**, 61 (1972).
7. R. G. Giovanelli, Solar Phys. **27**, 71 (1972).
8. B. W. Lites, Astrophys. J. **334**, 1054 (1988).
9. S. Musman, A. H. Nye, and J. H. Thomas, Astrophys. J. Lett. **206**, L175 (1976).
10. A. H. Nye and J. H. Thomas, Solar Phys. **38**, 399 (1974).
11. H. Zirin and A. Stein, Astrophys. J. Lett. **178**, L85 (1972).
12. T. J. Bogdan, D. C. Braun, B. W. Lites, *et al.*, Astrophys. J. **492**, 379 (1998).
13. S. I. Gopasyuk and G. V. Lyamova, Izv. Krymsk. Astrofiz. Observ. **77**, 17 (1987).
14. Yu. D. Zhugzhda, Pis'ma Astron. Zh. **10**, 51 (1984).
15. B. W. Lites, Astrophys. J. **277**, 874 (1984).
16. É. I. Mogilevskiǐ, V. N. Obridko, and V. D. Shel'ting, Izv. Vyssh. Uchebn. Zaved., Radiofiz. **16**, 1357 (1973).
17. R. L. Moore, *The Physics of Sunspots*, Ed. by L. E. Cram and J. H. Thomas (1981), p. 259.
18. R. L. Moore and D. Rabin, Ann. Rev. Astron. Astrophys. **23**, 239 (1985).
19. J. H. Thomas, Aust. J. Phys. **38**, 811 (1985).
20. I. P. Turova, R. B. Teplitskaja, and G. V. Kuklin, Solar Phys. **87**, 7 (1983).
21. I. P. Turova, Kinematika Fiz. Nebesnykh Tel. **5**, 69 (1989).
22. M. Uexkull, F. Kneer, and W. Mattig, Astron. Astrophys. **123**, 263 (1983).
23. H. Balthasar, G. Cuveler, and E. Wiehr, Solar Phys. **112**, 37 (1987).
24. E. Marco, M. Aballe Villero, M. Vázquez, *et al.*, Astron. Astrophys. **309**, 284 (1996).
25. M. Sigwarth and W. Mattig, Astron. Astrophys. **324**, 743 (1997).
26. T. R. Rimmele, Astrophys. J. **445**, 511 (1995).
27. N. I. Kobanov, Solar Phys. **82**, 237 (1983).
28. N. I. Kobanov, Astron. Astrophys. **143**, 99 (1985).
29. N. I. Kobanov, Solar Phys. **145**, 11 (1993).
30. R. Muller, *Sunspots: Theory and Observations*, Ed. by J. H. Thomas and N. O. Weiss (1992), p. 174.
31. K. R. Chen, D. Y. Chou, and the TON Team, Astrophys. J. **465**, 985 (1996).
32. C. W. Allen, *Astrophysical Quantities*, 3rd Ed. (Univ. London, The Athlone, London, 1973).
33. A. M. Title, Z. A. Frank, R. A. Shine, *et al.*, Astrophys. J. **403**, 780 (1993).
34. Yu. V. Vandakurov, Pis'ma Astron. Zh. **21**, 300 (1995).

Translated by G. Rudnitskiǐ